Design of a superconducting atom chip for interfacing Rydberg atoms with microwave resonators

Leon Sadowski

Masterarbeit in Physik

angefertigt im Institut für Angewandte Physik

vorgelegt der
Mathematisch-Naturwissenschaftlichen Fakultät
der
Rheinischen Friedrich-Wilhelms-Universität
Bonn

Juli 2024

I hereby declare that this thesis was formulated by myself and that no sources or tools other than those cited were used.

Bonn, 23.07.2024
Date

Signature

1. Supervisor: Prof. Dr. Sebastian Hofferberth
2. Supervisor: Prof. Dr. Stefan Linden

Contents

Chapter 1

Introduction

During the past decades, quantum theory has developed from being a field of a purely fundamental study of physics to the point of being relevant in many cutting edge technologies, which has opened the field of quantum technologies [1, 2]. Applications of quantum technologies can among others be found in the fields of quantum cryptography [1, 3], quantum sensing [4], quantum simulation [5] and quantum computing [6]. The quantum systems used in the various fields all come with their distinctive advantages and disadvantages [7]. This has lead to the approach of creating hybrid quantum systems by combining different quantum systems to exploit and leverage their respective advantages over a wide range of quantum technological application [2, 7–9]. It aims at the creation of a device which is capable of multiple required tasks simultaneously, like e.g. processing and storage of quantum information [2].

Among the various fields of quantum technology, quantum computing has gained increasing interest from both industry [10–12] and academia [6]. This is due to its potential to solve specific computational problems that are considered to be intractable with classical computers [6], for example Shor's algorithm for factorization [13]. However, the development of the necessary quantum computing hardware poses major technological challenges that have to be tackled along the way [6, 14].

In the quest for quantum computing platforms, a series of quantum systems are currently under investigation, including among others ions [15], Rydberg atoms [16] and superconducting circuits [17]. At the time of writing, it is not yet clear which, if any, platform will ultimately provide the hardware for a quantum computer that fulfils the DiVincenzo criteria for quantum computing [18].

Recently, the field of superconducting qubits has been the subject of considerable public attention. Despite the subsequent contradiction [19], this was due to the claim of quantum supremacy using a programmable superconducting processor [10]. Superconducting qubits enable fast gate operations [8, 20], tunability [8], strong coupling to external fields [8] and promise good scalability [8, 20].

Besides the advantages of superconducting qubits, they do not have long coherence times when compared to isolated quantum systems like atoms [8, 21]. Furthermore, superconducting qubits operate with frequencies in the microwave regime around 6 GHz [10], while sophisticated information transfer over large distances relies on optical frequencies due to its superior transfer abilities [7, 22, 23]. This fact hinders the integration

of superconducting circuits into proposed quantum networks [24]. That is one reason why devices for quantum transduction as microwave-to-optical interfaces have been investigated with growing interest [22–25]. Consequently, hybrid quantum systems that include superconducting qubits have been proposed in an attempt to overcome their limitations [8]. This includes coupling superconducting qubits to systems with large coherence times like atoms [8] and high quality factor electromechanical resonators [8, 26–28], which could potentially enable quantum memories [27] or serve as quantum transducers [29].

Among these interfaces, electromechanical oscillators are particularly appealing not only for the area of quantum technologies, but also as an interesting system to observe classical-to-quantum behaviour of mesoscopic mechanical quantum systems, when cooled to their quantum mechanical ground state [28, 30, 31].

The latter could also enable an indirect coupling scheme that facilitates quantum state transfer between superconducting qubits and long-lived atomic states bridged by the electromechanical oscillator [8, 20]. Electromechanical systems are a promising candidate for such a scheme due to their large quality factors [26, 28] of up to 10^7 [26] and strong coupling to superconducting qubits [27] while potentially providing a scalable approach [8, 20] due to their small physical size, that leverages the on-chip fabrication capabilities of superconducting circuits [8].

A promising candidate for exploiting the long coherence times of atomic states in hybrid quantum systems are Rydberg atoms that cover transition frequencies over a large range from optical to microwave [32] and simultaneously overcome the limited coupling strength of ground-state atoms to external fields [20, 32]. This is due to Rydberg atoms being highly excited atoms [32] with corresponding large electric dipole moments, which renders them very sensitive to external electric fields [32], in particular to microwaves [33].

While the large sensitivity also poses experimental challenges due to stray electric fields [34], experiments have shown the feasibility of achieving long coherence times of Rydberg atoms close to chip surfaces [35], paving the way towards proposed hybrid quantum systems interfacing Rydberg atoms and electromechanical resonators on a chip [20, 30].

Such an interface in a cryogenic environment of 4.2 K and the aim to cool a resonator mode to its quantum mechanical ground state is the stated objective of the Hybrid Quantum Optics (HQO) experiment in the Nonlinear Quantum Optics group of Sebastian Hofferberth. This thesis was prepared as a part of the HQO experiment.

Integrating a Rydberg atom - resonator interface on an atom chip [36] enables the precise positioning of ultracold atoms above the electromechanical resonator, which allows for the control of the Rydberg atom - resonator interaction [36, 37]. The electromechanical resonator is intended to be a high-overtone bulk acoustic resonator (HBAR) with a high-quality acoustic substrate, which enables large quality factors [26]. Given its hybrid nature, the experiment requires to be tackled from two directions, the atomic side being one of them and the interacting resonator the other one.

The atomic ensemble needs to be prepared and brought into close vicinity of the

resonator to carry out the experiments. On the other hand the resonator has to be designed to match the atomic transition frequencies and enable sufficient coupling strengths. Currently, the experiment consists of a room temperature setup. It is capable of ultracold atom preparation in a separate chamber by using a magneto-optical trap and to transport the trapped atoms into a second chamber, the science chamber, through a magnetic transport setup. For a detailed description of the room temperature experimental setup see the master thesis of Johanna Popp [38].

This setup will be extended by a closed-cycle cryostat, which provides the cryogenic temperature of 4.2 K inside the science chamber. The goal of this thesis is to design an atom chip that will be integrated into the cryogenic science chamber setup. The atom chip is supposed to be loaded from the last transportation coil of the magnetic transport setup, and it will integrate a microwave resonator on its surface. To avoid excessive heating of the cryogenic region, current-carrying parts of the atom chip will be made of superconducting material.

Since the room temperature setup is just about to be extended by the cryostat, still a number of steps between the successful magnetic transport process and the interaction of on-chip trapped atoms with any kind of microwave resonator have yet to be tested. Therefore, the first-generation atom chip of the experiment that is designed in this thesis has its focus on the possibility to allow for testing of the essential experimental steps, ranging from chip-loading to Rydberg atom detection, that are needed before on-chip interaction between atoms and an electromechanical oscillator can be observed. That is why the designed chip relies on the implementation of a coplanar waveguide resonator due to its ease of fabrication [39] and since its ability to couple to Rydberg atoms has already been experimentally demonstrated [40], rather than an electromechanical resonator. However, the implemented on-chip trapping is designed with a later-generation chip in mind, aiming at the best possible transferability of the experimental procedure from the first- to later-generation atom chips.

The structure of the thesis will be outlined in the following. First, chapter 2 discusses how the on-chip magnetic trap can be loaded from the last transport coil pair. Second, chapter 3 describes the design of the on-chip superconducting microwave resonator. Afterwards, chapter 4 demonstrates how both on-chip structures have to be positioned in order to enable Rydberg atom - resonator interaction, how the on-chip trap facilitates the active positioning of trapped atoms relative to the resonator and outlines which coupling strengths can be expected. For that, the physical basics of Rydberg atoms will be introduced and finally, it gives an overview of the fabrication process of the atom chip. In chapter 5, a short introduction to the prospective electromechanical resonator will be given before chapter 6 discusses the aspects of integrating the first-generation atom chip into the experimental setup and what has to be considered to verify Rydberg excitations and Rydberg-microwave interactions.

Chapter 2

Magnetic trapping of neutral atoms

The following chapter is dedicated to the trapping mechanism for neutral atoms on the atom chip. While it is also possible to trap neutral atoms in optical dipole traps [41], this chapter discusses the principle of a magnetic trap. Magnetic trapping is the technique of choice when it comes to the design of atom chips [36, 42] which allows for a precise control of the trap position close above the chip surface. In addition, since this trap does not require any laser beams to support the trap, a possible source of heating in the cryogenic region of the experimental setup can be avoided.

The following sections will first give an introduction into the physical principle of magnetic trapping. Afterwards, the specific configuration that is used for the atom chip will be discussed together with the demonstration of a possible loading scheme of the atom chip.

2.1 Theory of magnetic trapping

An atom in an external magnetic field exhibits energy shifts of its states, which is known as the Zeeman effect. This is due to the interaction energy between a magnetic moment $\vec{\mu}$ and the magnetic field $\vec{B}$, which is given by [43, 44]

$$V = -\vec{\mu} \cdot \vec{B}. \tag{2.1}$$

Under the assumption that the change of the magnetic field angle θ with time is slow compared to the Lamor precession ω_L, which can be expressed as [44]

$$\frac{\mathrm{d}\theta}{\mathrm{d}t} \ll \omega_L = \frac{g_F m_F \mu_B B}{\hbar}, \tag{2.2}$$

it can be assumed that the spin follows the direction of the magnetic field adiabatically. This assumption allows to write equation (2.1) as [45]

$$V = m_F g_F \mu_B B \tag{2.3}$$

for an atom in the hyperfine state $|F, m_F\rangle$ in a magnetic field with field strength B. Here, g_F is the Landé factor and μ_B denotes the Bohr magneton. The vector nature of equation (2.1) can be neglected with the adiabatic assumption, since the magnetic field

direction sets the quantization axis for the under this condition conserved m_F quantum number.

For a configuration with magnetic field minimum, the potential of equation (2.3) becomes attractive for states with $g_F m_F > 0$, which are therefore called low-field seekers [44], meaning that these atoms can minimize their energy by moving towards a position with low magnetic field strength and getting trapped at this position. In contrast, states with $g_F m_F < 0$ feel an attractive potential for a magnetic field maximum and are called high-field seekers [44]. However, only magnetic field minima can be created in free space [44] and are therefore used for magnetic trapping.

Trapping atoms means that their thermal energy does not suffice to escape the potential barriers of the trap [46], the latter is defined by the trap depth. Thus, the magnetic trap depth T_{td} is commonly given in units of temperature, using the ansatz of comparing thermal energy with the magnetic potential, which yields $T_{\mathrm{td}} = \mu B_{\mathrm{td}}/k_B$ with the Boltzmann constant k_B, and the magnetic field strength B_{td}.

Here, it should be noted that the velocities of atoms inside a magnetic trap will follow the Maxwell Boltzmann distribution for a given temperature and therefore the faster atoms of the distribution would escape a trap with depth equal to the cloud temperature. As a rule of thumb one can assume the potential barrier being high enough to keep all atoms trapped if it is about ten times the cloud temperature.

2.1.1 Magnetic trap configurations

The magnetic field minimum needed to form a magnetic trap can be realized by different experimental setups. A simple method is to create a quadrupole potential by two coils in an anti-Helmholtz configuration [44]. Such a configuration and the resulting magnetic field is schematically shown in figure 2.1.

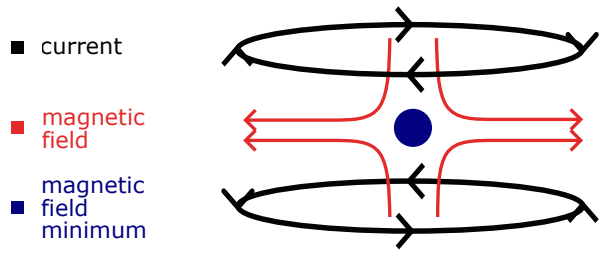

Figure 2.1: Anti-Helmholtz configuration coil pair. Two coils that carry a current in different directions create a magnetic field configuration as indicated with the red field lines. This results in a magnetic field minimum in the centre between both coils, where a magnetic trap can form (indicated by the blue circle).

The quadrupole potential increases linearly along all axes away from the minimum,

with two axes having an equal potential gradient and one with twice that gradient. However, this trap comes with the disadvantage of having a zero field minimum which can lead to atoms undergoing non-adiabatic spin flips into a high-field seeking state and consequently not being trapped anymore (see section 2.1). This process is also known as "Majorana spin flips" and therefore the lifetime of these traps can be severely limited [44]. To avoid this loss mechanism, a non-zero field minimum is required and can, among other options, be achieved by a configuration that leads to the so-called Ioffe-Pritchard traps. An Ioffe-Pritchard like trap describes a trap configuration that has a finite field strength at its minimum, is harmonic in proximity of the minimum and show quadrupole potential characteristics further away from the minimum [37]. In fact, the potential behaves harmonic for a thermal energy of the atom cloud less than the magnetic potential at the trap minimum [44, 47]. The Ioffe-Pritchard trap is harmonic around its minimum and can thus be characterized by the trap frequencies ω of the trap axes. The trap frequencies correspond to the motion of a particle around the minimum, exemplarily given for the x axis by [47]

$$\omega_x = \sqrt{\frac{\mu}{m}\frac{\mathrm{d}^2 B}{\mathrm{d}x^2}} \tag{2.4}$$

with the second partial derivative of the absolute field strength along that axis and the mass m of the particle in question. In this thesis ^{87}Rb is considered.

2.2 Magnetic wire traps

While large coil setups allow magnetic trapping of cold atoms, efforts have been put into miniaturizing magnetic traps to the state of implementing nano fabricated chips with integrated wires. That allows for magnetic trapping with strongly confined traps with low currents, e.g. used for the creation of Bose-Einstein condensates [36, 37].

These miniaturized trap configurations can be realized by the combined use of current carrying wires and external homogeneous magnetic bias fields [37, 48]. Magnetic wire traps can be integrated onto chip surfaces, the so-called atom chips, which allows precise control of the trap position, hence magnetic wire traps have been thoroughly discussed in the literature [36, 37]. Their working principle will be discussed in the following.

A wire that carries a current I_w creates a rotational symmetric magnetic field B_w around it, that decreases with the radial distance r from the wire like $B_w \propto I_w r^{-1}$ [43], see figure 2.2.

If an external homogeneous magnetic field B_b is applied perpendicular to the long and straight wire, it will cancel with the magnetic field of the wire, creating a magnetic field minimum with zero field strength at a radial distance r_0 away from the wire [37]. This creates a two-dimensional quadrupole trap, enabling an atom guide [36, 37]. In order to create a three-dimensional trap, confinement along the axial direction is necessary, as well. This can be done by bending the wire ends in either the same or opposite directions,

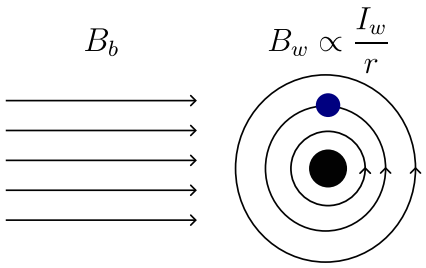

Figure 2.2: Working principle of a magnetic wire trap. The magnetic field B_w created by a wire (shown as black circle in cross-sectional view) that carries a current I_w is superimposed with a homogeneous bias field B_b. B_w is inversely proportional to the distance from the wire like r^{-1}, such that B_w and B_b cancel at a certain distance from the wire. At that position (indicated with the blue circle), a magnetic field minimum is created, which can serve as a magnetic trap.

hence creating a U or Z shaped wire [37], see figure 2.3. The U shaped wire trap shows the characteristics of a three-dimensional quadrupole trap, while the Z shaped wire is an Ioffe-Pritchard-type trap with the characteristics mentioned above [37]. To avoid the described Majorana losses, the Z wire trap is the trap of choice for the experimental setup.

Interesting properties of the Z wire trap are the distance between trap and wire and the curvatures along the radial and axial direction, which are commonly characterized by the trap frequencies [37, 47]. For thin and infinitely long wires and under the assumption that the distance between trap and wire r_0 is smaller than the length L of the central Z wire bar, the scaling behaviours can be given analytically by [37]

$$r_0 \propto \frac{I_w}{B_b} \qquad \frac{\mathrm{d}^2 B}{\mathrm{d}r^2} \propto \frac{B_b^5 L^2}{I_w^4} \qquad \frac{\mathrm{d}^2 B}{\mathrm{d}x^2} \propto \frac{B_b}{L^2}, \tag{2.5}$$

with the wire current I_w and the magnetic bias field B_b for the curvatures along the radial r and axial x directions[1]. Very close to the minimum the trap can be approximated as harmonic [37], thus allowing to calculate trap frequencies ω along the different axes of the trap. While L is fixed by the chosen geometry, the bias field and wire current can be changed during the experiment, which allows manipulating the trap characteristics like position and compression while having atoms trapped inside.

As a consequence of the point symmetry of the Z wire shape, the cylindrical trap is slightly rotated with respect to the central bar of the Z wire [47].

[1] This corresponds to a trap in the coordinate system used later on, where the central Z wire bar is in parallel with the x axis.

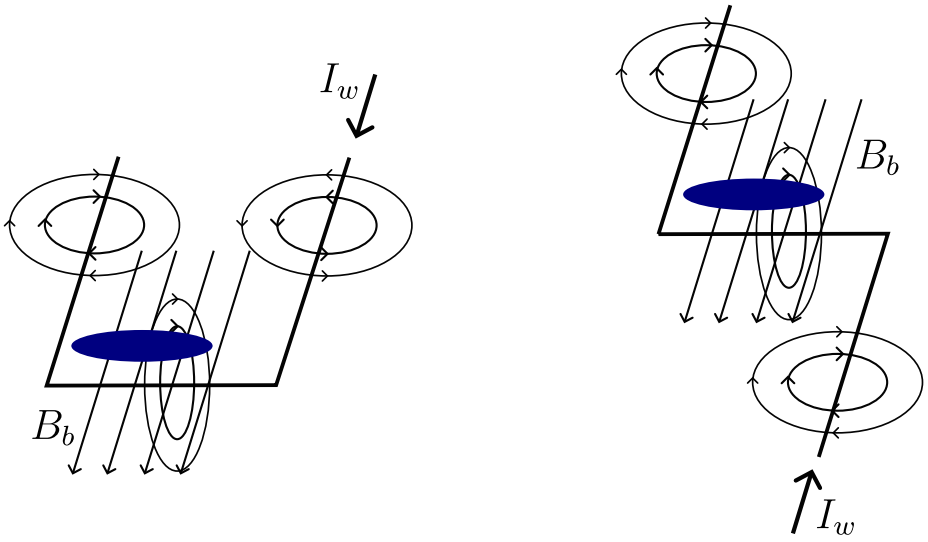

(a) U wire trap.

(b) Z wire trap.

Figure 2.3: Schematic of magnetic wire traps, adapted from [37]. In both images, the shaped wires carry a current I_w which creates a radial magnetic field indicated by the circular field lines. In both cases, a homogeneous magnetic bias field B_b is used to superimpose the magnetic field created by the wire, which creates a magnetic field minimum. In (a), a U shaped wire is shown, which creates a trap with quadrupole-like potential. (b) depicts a Z shaped wire which creates an Ioffe-Pritchard like trap potential.

2.2.1 Gravitational influence

The potential landscape seen by the atoms is a linear combination of the magnetic potential and the gravitational potential. The effect of the gravitational potential on the trapping potential has been discussed in e.g. [47, 49]. A magnetic field potential that produces the same force as the gravitational potential would be $U_{\text{grav}} = 15.29\,\text{G/cm}$ for ^{87}Rb atoms and the atomic state $|F = 2, m_F = 2\rangle$. This potential does not shift the position of a quadrupole trap but can make it more shallow [50]. In contrast, it can shift the minimum position of an Ioffe-Pritchard trap along the z direction, by [47]

$$\Delta z = \frac{g}{\omega_z^2} \tag{2.6}$$

with the gravitational acceleration g and the trap frequency along the z direction ω_z. Thus, the strong curvature axis of a used magnetic trap should be oriented along the vertical axis in order to minimize the gravitational influence. For trap frequencies of around

$\omega_z = 2\pi \times 150\,\mathrm{Hz}$, which will be relevant for the Z wire trap in question, equation (2.6) yields a gravity-induced potential minimum shift of $\Delta z = 10\,\mu\mathrm{m}$.

2.3 Simulation overview

The planned experimental procedure requires the loading of atoms from a magnetic quadrupole trap created by the last anti-Helmholtz coil pair of the magnetic transport setup, into the on-chip Z wire trap in order to perform on-chip experiments.

To simulate this transfer process, python code was written to calculate the static magnetic trap geometry and visualize the expected atomcloud. It will also be used to simulate the dynamic behaviour of atoms loaded from one magnetic trap into another. The goal of the simulation is to find a feasible transfer sequence.

Some parts of the simulation code base originate from the research project conducted by Florian Pausewang, supervised by Cedric Wind. It was used to write a more readily maintainable program and was also augmented to facilitate three-dimensional visualizations of trap geometries. The simulation code makes use of the python package magpylib [51] which provides analytic solutions for the magnetic field of current carrying structures for the efficient calculation of the magnetic fields created by the quadrupole and Z wire trap. The Z wire trap scaling laws of equation (2.5) are approximated under the assumption of a large trap to wire distance compared to the width of the central Z wire bar and infinitely thin wires [37]. A common method to take the finite wire width into account is to approximate the wire width using several infinitely thin wires equally distributed over the width of the actual wire, also called the 'stick model' [47]. This model is implemented in the simulation in order to take the wire width into account. However, the model is still an approximation because it assumes a homogeneously distributed current density over the complete wire width, which deviates from a real wire where the current density varies especially at the wire edges [47].

The simulation allows to calculate the static trap geometries and potential landscapes directly. For example, the results of these potential landscapes can be used to calculate trap frequencies for the Z wire trap, which will be shown in section 2.4.2.

In order to simulate the dynamics of atoms in a static or time-dependent potential, the simulation allows to initialize a cloud of atoms of temperature T via a Monte Carlo initialization of atoms in the potential (depending on temperature via $\exp(-V(\vec{r})/k_B T)$), with its velocities following the Maxwell-Boltzmann-Distribution.

Subsequently, the potential can be used to calculate the movement of the atoms inside that potential by solving Newtons equations of motion numerically. However, the simulation does not implement collisions between atoms. Consequently, the initialized velocity distribution follows the Maxwell-Boltzmann distribution, but no re-thermalization takes place if the trap potential is changed. Furthermore, the simulation neglects quantum mechanical effects such as Majorana spin flips, and is a purely classical simulation.

Hence, and as there is no experimental feedback yet, the simulation does not claim to be completely accurate, but rather is used to serve as a guide for the experimental implementation of a transfer sequence.

The simulation allows animating most of the dynamic behaviours, like atom trajectories and the change of the potentials with changing currents in the magnetic field coils and Z wire, however the following discussion will be restricted to static plots.

The simulation includes the influence of gravity on the potential landscape for all presented calculations.

2.4 Atom cloud transfer

The following section is dedicated to the characterization of the intended atom transfer from the quadrupole trap to the on-chip trap. In order to get a better understanding of the initial trap positions and characteristics, the corresponding trap geometries will be shown in the next sections.

The process of transferring atoms should ensure an efficient transfer in the sense of achieving a reasonable number of atoms in the on-chip trap to allow for a successful experiment. Additionally, the transfer should avoid coating of the chip surface with rubidium atoms. This is because such a coating could lead to surface charges with corresponding stray electric field, which have to be avoided in the vicinity of the Rydberg atoms. Furthermore, coating the oscillator might lead to dampening of the oscillations, as well.

In order to implement a transfer sequence that meets these requirements, the currents of the quadrupole coils as well as the Z wire current and the applied bias fields can be controlled dynamically. Using the scaling of the trap parameters introduced in section 2.2 as guidance, a transfer sequence is supposed to be found. An evident approach for this simulation is a linear ramp of both trap types, consequently this approach will be discussed in the final section.

2.4.1 The initial quadrupole trap

After the magnetic transport of the atoms into the science chamber, which will host the atom chip, the atoms are trapped in a quadrupole potential created by the last magnetic transport coil pair. This is the start position for the transfer sequence to the atom chip in the simulation.

The initial quadrupole trap created by the last transport coil pair has a magnetic field gradient of 130 G/cm along the strong trap axis. Figure 2.4 shows the linear potential of the quadrupole trap along the coordinate axes with its minimum at the origin. It shows that the magnetic field gradient is the same for two axes and twice that for the third axis. Accounting for the gravitational effects discussed in section 2.2.1, the trap is configured to have the strong gradient along the z axis. The effect of the additional

linear gravitational potential is reflected in the asymmetric potential along the z-axis in figure 2.4.

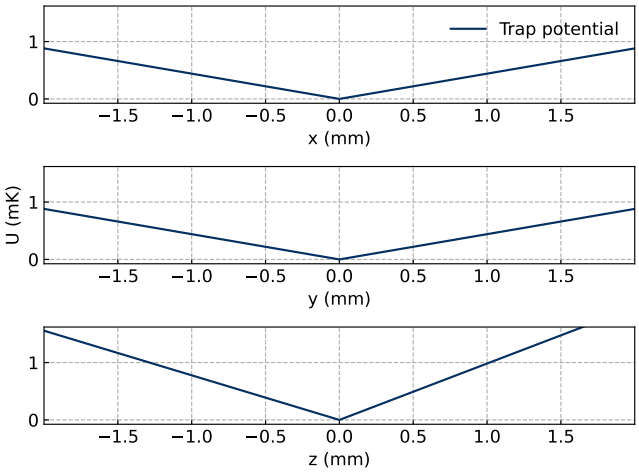

Figure 2.4: One dimensional potential curves of quadrupole potential along each spatial coordinate axis. The potential is altered along the z-axis due to the gravitational potential. To account for the gravitational effects, the strong axis of the trap, with twice the potential gradient than along the other axes, is taken along the z axis.

2.4.2 The initial Z wire trap

The on-chip magnetic trap will be formed by a Z wire structure and an applied magnetic bias field, which form an Ioffe-Pritchard type trap, as explained in section 2.2. The Z wire trap geometry that will take over the atoms previously trapped in the quadrupole trap is subject of this section. Its configuration will be referred to as the initial Z wire trap position in the following, which anticipates subsequent manipulations of the trap position that will be shown in section 4.2.

The initial trap position is supposed to be in the largest possible distance from the chip surface to avoid coating the chip with Rubidium atoms previous to or during the transfer process. According to equation (2.5), reducing bias fields and increasing the wire current leads to an increasing distance between trap position and the wire, i.e. the chip surface. The lower limit of the bias field strength is given by its ability to form a deep enough trap [50]. On the other hand, the upper limit of the wire current is determined by the fact that the Z wire will be made of a superconducting structure on the chip, the concept of superconductivity will be discussed later on in section 3.2.3. However, for the purpose needed here it is sufficient to recognize that there exists a current which, if exceeded in a superconducting structure, leads to the breakdown of superconductivity. It

is referred to as the critical current. The critical current for this case can be estimated by assuming a layer thickness of 500 nm and a wire width of 100 µm for niobium as the used superconducting material, which corresponds to the chip fabrication parameters discussed in section 4.3. Based on measurements of the critical current density of niobium films at a temperature of 4.2 K in reference [52], the critical current for the final chip is estimated to be about $I_c \approx 2.9\,\mathrm{A}$. Note, that in principle the critical current density decreases linearly with the applied magnetic field for small magnetic fields [52]. However, when referring to the data of reference [52], the magnetic field influence is negligible for the magnetic field strengths used here (order of magnitude 10 G), as the critical current decreases with the proportionality factor $-0.51\,\mathrm{A/kG}$ for a niobium film with the same cross-sectional area like the one used here[2]. Due to the sharp turns of the Z wire structure, the local current density at these turns can be expected to exceed current densities of a regular Niobium strip, which was used for the measurements in reference [52]. Consequently, to be on the safe side, a wire current maximum of 2 A is assumed for the following calculations.

The magnetic potential of the trap in one dimension along the x, y and z coordinate axes is shown in figure 2.5(a) for a Z wire current of $I_w = 2\,\mathrm{A}$ and a bias field $B_z = 6\,\mathrm{G}$. This visual representation verifies the harmonic potential around the minimum with quadratic fits as a reference for the eye. The actual trap shape can be recognized more conveniently in figure 2.5(b), where the 100 µK potential isoline is highlighted directly above the 3 mm long central bar of the Z wire. The plot shows the potential contours in the xz-plane at the potential minimum's y coordinate and the Z wire has to be imagined as being placed in the xz-plane at $y = 0$. The plot indicates that the ellipsoid trap geometry is slightly rotated with respect to the central bar of the Z wire, which is characteristic for this trap configuration [47]. For the given parameters, the rotation of the ellipsoid main vectors with respect to the lab axes amounts to 6° for the x and z axis.

In order to calculate the trap frequencies this rotation has to be considered by fitting a harmonic potential along the rotated main axes of the ellipsoid and not along the coordinate axes. The rotation is accounted for in the trap frequency calculation algorithm of the simulation and leads to the trap frequencies of $\omega_{\tilde{z}} = 2\pi \times 149\,\mathrm{Hz}, \omega_{\tilde{y}} = 2\pi \times 153\,\mathrm{Hz}$ and $\omega_{\tilde{x}} = 2\pi \times 15\,\mathrm{Hz}$, where the tilde denotes the frequency along the ellipsoid main axes that are closest to the respective lab system axes. Here, the axial direction of the trap clearly follows the x-coordinate axis closest, see figure 2.5(a).

[2] Measured for a perpendicular applied field. Some parts of the Z wire will be exposed to parallel magnetic fields, however its influence is less critical than the perpendicular field strength, or at least comparable for the film thickness at hand [53, 54]. Thus, the parallel field influence can be neglected, as well.

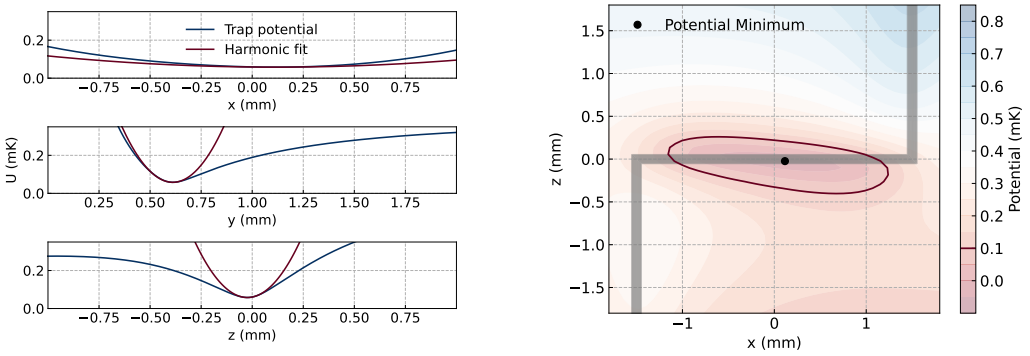

(a) **(b)**

Figure 2.5: Magnetic potential of the Z wire trap for a wire current of $I_w = 2\,\mathrm{A}$ and a bias field $B_z = 6\,\mathrm{G}$. (a) shows the potential in one dimension along the coordinate axes including quadratic fits around the minimum position to illustrate the harmonic characteristic of the potential. (b) shows a contour plot of the potential in the xz plane of the minimum position with a highlighted isopotential line for 100 µK. The Z wire, shown in gray, is illustrated as a projection into the shown xz plane from its actual position in the $y = 0$ plane.

2.4.3 Transfer sequence

Having discussed the relevant static properties of the involved traps, the next step is to discuss a possible transfer sequence to load the Z wire trap from the quadrupole trap. A successful transfer sequence would result in a large fraction of atoms that are transferred from one trap to the other and a heating of the cold atom cloud would be prevented as good as possible. To find such a sequence, the trap characteristics are important to keep in mind and certain requirements need to be fulfilled. A first requirement would be a reasonable "mode-matching", following the wording of optical cavities, of the initial and final trap [44]. This means the best possible overlap between the trap geometries in the region occupied by the atom cloud. Figure 2.6 shows the overlap of the isosurfaces of the initial quadrupole trap and the final Z wire trap for the same trap depth, with both trap minima matching reasonably well. This plot clearly shows the difference of both geometries. For the Z wire trap the axial trap frequency is way smaller than the radial one, resulting in the long ellipsoid shape of the trap. In contrast, the quadrupole trap is way more confined. Additionally, the Z wire trap is larger than the quadrupole trap for the same trap depth. This will result in some sloshing of the atom cloud after the transfer.

In order to make the Z wire trap become smaller, a stronger bias field would have to be applied. However, due to equation (2.5), this would bring the trap closer to the chip

surface and lead to a different minimum position compared to the quadrupole trap. To compensate for that, a larger wire current would be needed, but the current is limited by the critical current of the superconducting wire, as mentioned above. However, even for a smaller trap along the radial directions of the ellipsoid the axial confinement would remain and a perfect mode matching is not possible between both trap types [47]. It should also be noted that the magnetic field strength at the minimum is different for the two types of trap, which may also affect the transfer behaviour.

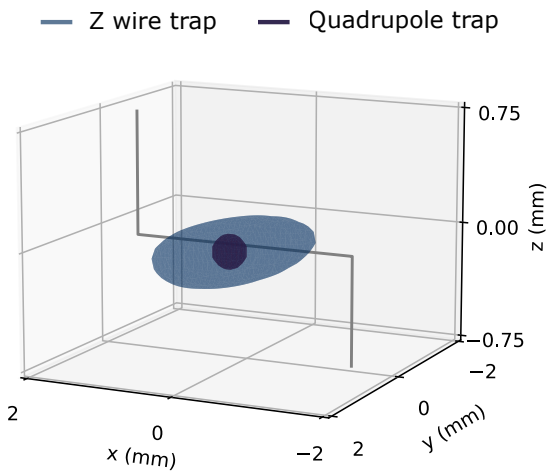

Figure 2.6: Overlap of the 100 µK isosurfaces of the initial quadrupole and initial Z wire trap. The ellipsoid Z wire trap geometry is shown in blue with the smaller quadrupole trap in red (appearing dark blue) inside.

The quadrupole trap itself also exhibits problematic behaviour with regard to the transfer. If a quadrupole trap is superimposed with a homogeneous bias field, the external magnetic field shifts the quadrupole minimum away from its bias free position. For the trap case, this means that the trap position will be shifted in dependence of an applied homogeneous external magnetic field. Figure 2.7 shows how the shift becomes worse during the actual transition when the coil current is decreased while the applied magnetic bias field is increased. Lower coil current leads to a less steep quadrupole potential gradient and thus makes the minimum position more sensitive to the applied magnetic bias field.

This illustrates that a smooth transition between the two traps does not appear to

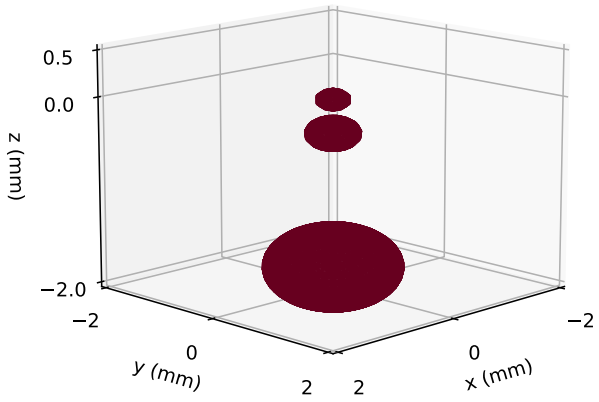

Figure 2.7: The figure shows three isosurfaces of the quadrupole trap, each corresponding to 100 µK, while the bias field B_z is being ramped up and the transport coil current down. The smallest trap geometry depicts the isosurface for zero applied bias field and a quadrupole trap gradient of 130 G/cm along the z axis. For decreasing quadrupole gradients the same isosurface increases in size and the trap minimum position becomes more sensitive to applied bias fields. This leads to a strong shift of the quadrupole trap position during a ramping sequence.

be possible. Thus, from this static potential point of view a successful transfer appears challenging.

However, while the static picture can give an understanding of the problem to tackle, in the end the timescales of the atom movement and the build-up of the trap play a very important role. If the movement of the atoms is slow compared to the changing potential around them, the transition sequence can become less critical. Indeed, in the literature the common way to transfer atoms between different kinds of traps is to switch fast between both types [37, 44]. The following paragraphs will show that a simple transfer sequence allows a reasonably efficient transfer contrary to the concerns from the static view.

Therefore, a dynamic simulation of the atom transfer was run, as explained in section 2.3. Note, however, that the dynamic simulation does not take into account rapid changes in the magnetic field, which could violate the adiabatic condition equation (2.2).

To enable the transfer, three different parameters are crucial. These are the transport

coil current, which is ramped down and the Z wire current and bias field which have to be ramped up in order to form a Z wire trap. A linear ramping sequence for these parameters to switch between both trap types is shown in figure 2.8, where the duration of the ramp is 10 ms. In the following paragraphs, the ramping duration will be referred to as the transition time.

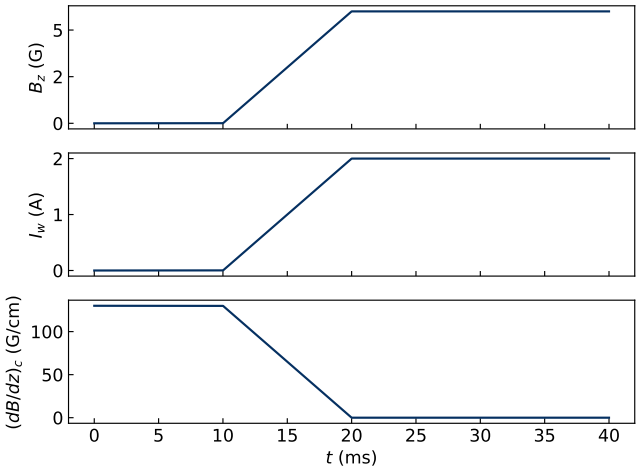

Figure 2.8: Transfer sequence with linear ramps of all involved parameters, i.e. bias field B_z, the Z wire current I_w and the magnetic field gradient of the quadrupole trap $(dB/dz)_c$, influenced by the coil current. The parameter ramping starts at 10 ms for a duration of 10 ms.

The dynamic simulation is run for three different initial cloud temperatures 10 µK, 40 µK and 70 µK for two sequences with different transition times. These temperatures and transition times are selected on the basis of what is expected to be experimentally achievable. The limiting factor for the transition time is the feasible switch-off time of transportation coil currents. Since these are water cooled in a solid copper mount, Eddy currents limit the switching time. For the current setup 20 ms were measured to fully eliminate the created magnetic field. However, replacing the heat sinks could potentially reduce this time to 10 ms. These considerations motivate the simulated transition times of 10 ms and 30 ms. The resulting transfer efficiencies are shown in figure 2.9 by plotting the relative number of trapped atoms as a function of time. This demonstrates the transfer efficiency at all times during the transfer sequence.

The first thing to notice is the crucial influence of the initial cloud temperature which shows that lower initial temperatures lead to an improved transfer efficiency. This is reasonable, because a colder cloud will expand slower while the new potential is formed around it during the transition and thus fewer atoms escape the trapping region.

Following the argumentation of the temperature influence and the relevance of the

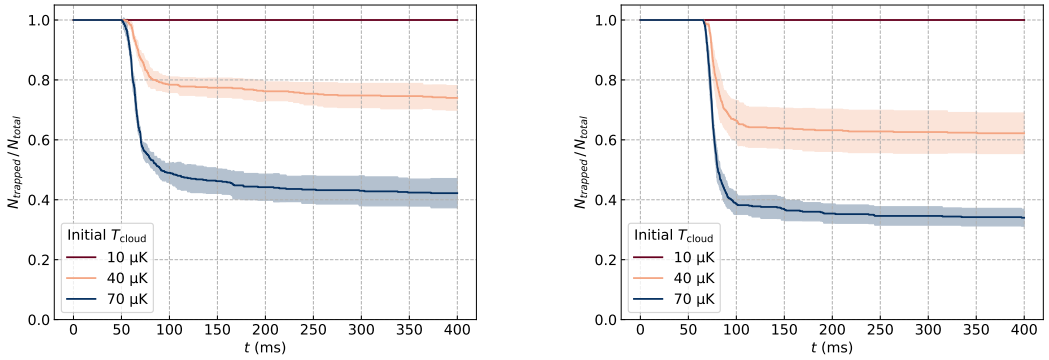

(a) Transition time of 10 ms.

(b) Transition time of 30 ms.

Figure 2.9: Relative number of trapped atoms $N_{\text{trapped}}/N_{\text{total}}$ during (a) 10 ms and (b) 30 ms transition time transfer processes for three different initial cloud temperatures. The plot shows the mean trapped numbers with one standard deviation of five simulations with 100 atoms each.

expansion velocity during the transfer, the slower transition should lead to worse efficiency results. This expectation is met when comparing the 10 ms transition time sequence to the 30 ms transition time. However, the difference is not really large and even with the longer transition time it is possible to transfer about 40 % of the atoms in the simulation.

Note, that the transition sequence for both transition times starts at $t = 10$ ms (see figure 2.8) and that the atom losses in figure 2.9 occur after the sequence has already reached the final trap steady state. In fact, the loss of the atom is determined during the sequence and the delay of the tracked atom loss is a consequence of the applied metric. In figure 2.9, an atom is considered lost from the trap as soon as its distance from the trap minimum is larger than three millimetres, i.e. as soon as it leaves a sphere of 3 mm around the minimum, which is why it will be called distance metric in the following. This radius is chosen to be twice the range of the larger axial trap size. The distance metric is readily applied and allows a computationally advantageous tracking of the time step when an atom is lost.

In order to demonstrate the validity of the distance metric, another unambiguous metric is introduced. It makes use of the velocity in z direction v_z. The trajectory of a trapped atom describes an oscillating movement and as soon as an atom is no longer trapped, its velocity component v_z will increase monotonically under the implemented influence of gravity. This fact is used to implement a metric that considers an atom lost when its v_z increases monotonically after some point in time until the end of the simulation. In figure 2.10 the spatial coordinates of a number of atoms trapped in a potential that undergoes an arbitrary transfer sequence is shown. It shows the oscillating

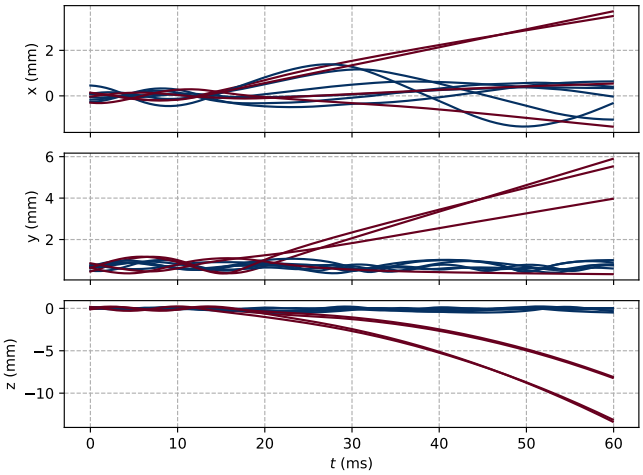

Figure 2.10: Coordinates of trapped atoms moving inside a trap with changing potential as a function of time t. The lines drawn in red are atom trajectories that were recognized as escaping out of the trap by means of the velocity metric (see text), the blue trajectories correspond to atoms that remain trapped.

movement of the trapped atoms and the quadratic spatial increase of the z component under the influence of gravity if an atom is lost from the trap, drawn in red. This plot intuitively explains the delay between the actual moment at which the atom is determined to be lost from the trap and the moment when this circumstance is captured by the distance metric. The resulting atom loss calculated by the respective metrics is compared for the same simulation runs, shown in figure 2.11. It indicates that both metrics are sufficiently accurate for the evaluation of a transfer sequence.

Summarizing, the main result of this chapter is that sequences can be found to achieve an efficient atom transfer between the final quadrupole trap of the magnetic transport setup and the on-chip Z wire trap. The simulations further support the intuitive assumption that aiming for properly pre-cooled initial atom cloud temperatures is advantageous. The found transfer sequence forms the first step of an extended sequence discussed in chapter 4. The extended sequence will facilitate the desired coupling between the trapped atoms, discussed here, and the resonator that will be subject of the next chapter.

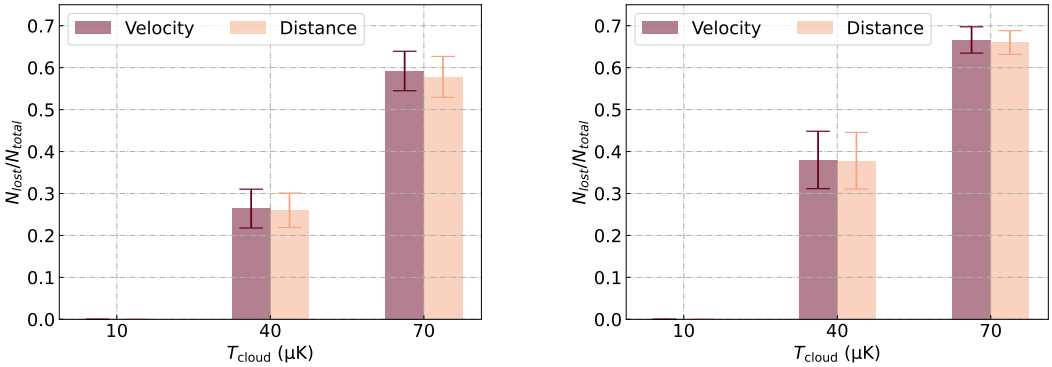

(a) Transition time of 10 ms.

(b) Transition time of 30 ms.

Figure 2.11: Comparison of mean calculated atom loss $N_{\text{lost}}/N_{\text{total}}$ by distance and velocity metric for different temperatures and transition times after a transfer sequence for five simulation runs. Both metrics show good agreement of the atoms that are considered to be lost from the trap. For an initial cloud temperature of 10 µK no atoms have been lost during any of the transfer processes, which leads to a non-visible loss-indicating bar for that temperature.

Chapter 3

Coplanar waveguide resonators

For the chip designed in this thesis, a coplanar waveguide resonator will serve as an on-chip microwave resonator. It is a transmission line resonator, that is derived from coplanar waveguide transmission line structures [55]. The following chapter will initially introduce coplanar waveguides to provide a design guide. This design guide will be used in the subsequent section to design a coplanar waveguide resonator that can be put onto the atom chip surface. Furthermore, the discussion will include an analysis of the potential sources that could result in a shift of the designed resonance frequency, accompanied by estimates of the extent of such a shift. Finally, a brief overview over potential device simulations is given in an attempt to include the aforementioned sources of frequency deviations for the specific device into the design process.

3.1 Theoretical introduction

This section gives an overview over the theoretical aspects when dealing with coplanar waveguide resonators. The first part introduces the structure of coplanar waveguides in general, then it will be discussed how this can be used to create a microwave resonator.

3.1.1 Coplanar waveguides

High-frequency signals require transmission line structures, that can carry them without larger losses. A well known transmission line is the coaxial cable, which is commonly used in laboratories and for all types of applications where high-frequency signals are applied. With the advent of integrated circuits, the need arose for transmission structures that could be applied to printed circuit boards [55]. One consequence of this development is the emergence of coplanar waveguides which are essentially two-dimensional variants of the aforementioned coaxial cables.

The cross-section of a ground-backed coplanar waveguide is shown in figure 3.1. The coplanar waveguide transmission line typically consists of three conducting parts, namely one central trace of width w and two ground planes next to the trace, separated by a gap of width s. The conducting parts of thickness t are deposited onto a dielectric substrate of height h with dielectric constant ϵ_r. If this coplanar waveguide gets an additional grounded conducting layer below the dielectric substrate, which is typically connected to

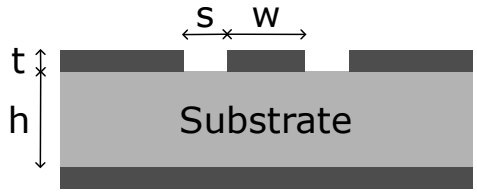

Figure 3.1: Cross-section and dimensions of a ground-backed coplanar waveguide. The dark gray areas are conducting parts of height t, consisting of a central trace of width w, lying in between two ground planes with a separation distance s on top of a dielectric substrate of height h. For the classical coplanar waveguide, the conducting plane below the substrate would be missing.

the top ground planes, it is called ground-backed coplanar waveguide [56]. Throughout this thesis, the term coplanar waveguide will refer to the combination of the trace and the coplanar ground planes.

In high-frequency circuit applications, the included transmission lines and components have to be impedance matched in order to avoid signal reflections at impedance mismatch positions. Typically, the impedance of these components is set to a value of $Z = 50\,\Omega$. The impedance of the waveguide is given by $Z = \sqrt{L_l/C_l}$, with the inductance L_l and capacity C_l per unit length [56, 57]. Both of them can be found via the method of conformal mapping and depend on the geometry of the structure. The expressions are given by [57]

$$L_l = \frac{\mu_0}{4}\frac{K(k_0')}{K(k_0)} \tag{3.1}$$

$$C_l = 4\epsilon_0\epsilon_{\text{eff}}\frac{K(k_0)}{K(k_0')} \tag{3.2}$$

with K being the complete elliptic integral of the first kind with the arguments $k_0 = \frac{w}{w+2s}$ and $k_0' = \sqrt{1-k_0}$. These expressions neglect the thickness t of the conducting parts and the substrate height h. For accurate results, however, both need to be included and would modify k_0 and k_0' [56]. However, the expressions equation (3.1) and equation (3.2) will nevertheless become useful later on.

The ratio of the trace width w and the gap spacing s determines the impedance of a coplanar waveguide transmission line for a given dielectric substrate and has to be designed accordingly [56, 57]. As a matter of fact, this leads to in principle infinite possibilities to design a waveguide of one specific impedance. That is an advantage,

because it allows to enlarge the dimension of the trace continuously while keeping a constant impedance, if the gap spacing is enlarged accordingly, which is used to create larger traces for connections to e.g. external electric contacting [56]. The equations for impedance calculation with and without ground conductor at the bottom differ, which has to be taken into account [56].

3.1.2 From waveguide to resonator

The signal reflections that are created at impedance mismatches can also be used on purpose. If two impedance mismatches are inserted at a distance l along a transmission line, the reflections between both positions can lead to the formation of a standing wave [58]. As a consequence, transmission line resonators can be designed by inserting discontinuities in the transmission line that lead to impedance mismatches.

Such resonators are commonly used in the field of circuit quantum electrodynamics and superconducting quantum computing and are therefore well described in the literature, see e.g. [57–59].

The impedance mismatch can be in the form of shorted and open ends. The simplest way of introducing such discontinuities is shown in figure 3.2 with one series capacitance and one series inductance [56, 59]. While the shorted end (inductive coupling) leads to a zero voltage boundary condition, the open end (capacitive coupling) ensures a zero current boundary condition [59]. Therefore, the discontinuity that leads to the formation of the resonator influences the behaviour of the electric and magnetic field of the standing wave at the resonator boundaries. The inductive zero voltage boundary condition leads to an electric field node at the discontinuity, while the capacitive zero current boundary conditions results in a magnetic field node (and thus electric field anti-node) [59].

(a) **(b)**

Figure 3.2: Coplanar waveguides in top view, with inserted impedance discontinuities. In (a) an open end in the waveguide is shown, which forms a capacitive discontinuity. In (b) a short end is illustrated, which introduces an inductive impedance mismatch.

Two open, respective shorted, ends at a distance l form a half wavelength resonator

with the standing wave condition

$$l = n\frac{\lambda'}{2}, n \in \mathbb{N}_{>0}. \tag{3.3}$$

Here, λ' denotes the wavelength of the standing wave inside the propagation medium with a positive integer n. Thus, for $n = 1$, the fundamental mode is formed by half a wavelength. In contrast, one shorted and one open end result in a quarter wavelength resonator [59].

The electric field of the fundamental and second harmonic standing wave in a capacitively coupled resonator is shown in figure 3.3.

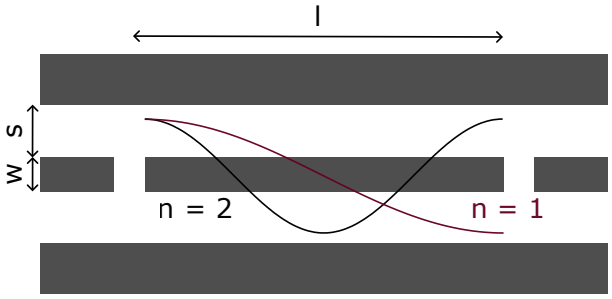

Figure 3.3: Schematic of a coplanar waveguide resonator in top view, adapted from [59]. The cosines indicates the electric field of the $n = 1$ and $n = 2$ harmonic modes of the standing wave in the shown open end (capacitively coupled) half wavelength resonator.

The resonance frequency of such a resonator can be derived and understood in an intuitive way. First, the phase velocity of an electromagnetic wave propagating through the waveguide $v_{\text{ph}} = c/\sqrt{\epsilon_{\text{eff}}}$ [57] with the speed of light in vacuum c and the effective dielectric constant ϵ_{eff} is needed. Additionally, the phase velocity is also given by the expression $v_{\text{ph}} = \lambda' f$ with the wavelength λ' inside the medium and the frequency f. Now, both expressions for the phase velocity are compared, and the standing wave condition plugged in for λ'. Thereby, the result for the fundamental resonance frequency given in [57] is obtained with

$$f_n = n\frac{c}{\sqrt{\epsilon_{\text{eff}}}}\frac{1}{2l}, \tag{3.4}$$

where the fundamental mode is denoted by $n = 1$. The fundamental resonance frequency is determined by the length of the resonator and the effective dielectric constant. The

effective dielectric constant is approximately given by $\epsilon_{\text{eff}} = (\epsilon_r + 1)/2$ [39], for the dielectric constant of the substrate ϵ_r and vacuum above the substrate, with a dielectric constant of 1.

Next to the intuitive approach, this result can also be obtained using an equivalent circuit analysis for frequencies near the resonance frequency, which is discussed in reference [57]. It is useful to conduct this analysis, since it reveals and explains further resonance frequency dependencies that are important when discussing the coupling of the resonator in this section and the peculiarities of superconducting resonators in section 3.2.3.

The resonator can in general be described as a distributed element circuit, but near resonance considered as a parallel LCR oscillator circuit [57]. The LCR circuit is connected to the rest of the transmission line with $R_L = 50\,\Omega$ at both sides, thereby becoming the feed lines, via coupling capacitors with capacitance C_κ [57], as shown in figure 3.4(a). The resistance R accounts for resonator losses [55]. The inductance L and capacitance C can be calculated from the resonator length l and the inductance and capacitance per unit length, respectively.

Neglecting the coupling of the resonator for now and following the derivation and definitions of reference [57], the resonance frequency of the oscillator circuit in figure 3.4(a) is given by

$$\omega_n = n\omega_0 = \frac{1}{\sqrt{L_{n,\text{def}}\, C_{\text{def}}}}, \tag{3.5}$$

with the mode number n dependent characteristic inductance $L_{n,\text{def}}$ and characteristic capacitance C_{def} as parameters[1], defined by [57]

$$L_{n,\text{def}} = \frac{2L_l l}{n^2\pi^2} \tag{3.6}$$

$$C_{\text{def}} = \frac{C_l l}{2}. \tag{3.7}$$

The definitions of equation (3.6) and equation (3.7) will be used in the following to show that they lead to the equivalence of both found equations for the resonance frequency, namely equation (3.4) as the result of the intuitive approach and equation (3.5) as the result of the LCR equivalent circuit analysis. To do that, both equation (3.6) and equation (3.7) are plugged into equation (3.5). After noting that the phase velocity of a coplanar waveguide resonator transmission line is given by [57]

$$v_{\text{ph}} = \frac{1}{\sqrt{L_l C_l}} \tag{3.8}$$

[1] Note the definition of these characteristic parameters. When using $\omega = 2\pi f$ to obtain equation (3.5) from equation (3.4), the π remains and is put into the definition of L_n in equation (3.4). Finally, equation (3.8) and equation (3.9) convert the different expressions for the phase velocity. In the main text this approach is reversed.

equation (3.5) becomes equation (3.4) since [57]

$$v_{\mathrm{ph}} = \frac{c}{\sqrt{\epsilon_{\mathrm{eff}}}} \tag{3.9}$$

can be written for the phase velocity as well. Note, that the equivalence of the two phase velocity expressions, i.e. equation (3.8) and equation (3.9), can be shown by plugging the expressions for L_l and C_l of equation (3.1) and equation (3.2) into equation (3.8).

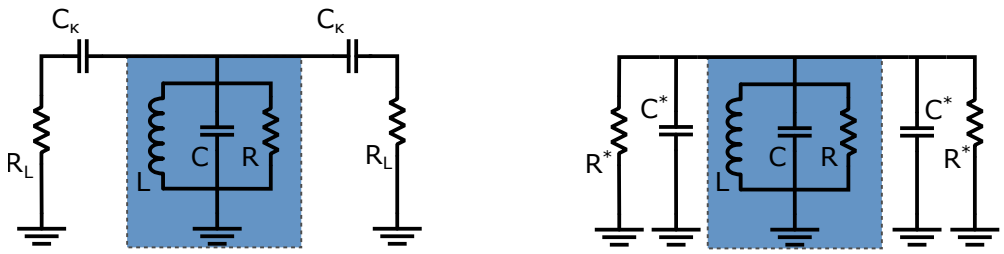

(a) **(b)**

Figure 3.4: Equivalent circuits of the coplanar waveguide resonator, adapted from [57]. Here, (a) shows the LCR circuit (in the blue box) equivalent of the coplanar waveguide resonator, which is coupled to the feed lines with the coupling capacitance C_κ. $R_L = 50\,\Omega$ denotes the load and L, C the total inductance and capacitance, respectively. The resistance R accounts for losses of the resonator. In (b) the coupling capacitances C_κ of (a) can be transformed into capacitances C^* parallel to the LCR circuit capacitance, that alter the resonance frequency. The loads R_L become the transformed impedances R^*.

Quality factor

An important parameter to compare resonators is the quality factor, which is in general defined as [39]

$$Q = \omega \frac{E_{\mathrm{res}}}{P_{\mathrm{loss}}} \tag{3.10}$$

with the frequency ω, the energy E_{res} stored in the resonator and the energy lost per cycle which is P_{loss}.

In most cases, resonators have to be coupled to an external system, like feed lines for example. This lowers the resonator's Q-factor. An isolated resonator is described by its internal quality factor Q_{int}. The coupling is taken into account with the external quality factor Q_{ext} which finally leads to the loaded quality factor Q_L of the coupled resonator, given by [55, 57]

$$\frac{1}{Q_L} = \frac{1}{Q_{\mathrm{int}}} + \frac{1}{Q_{\mathrm{ext}}}. \tag{3.11}$$

The loaded quality factor is experimentally accessible when considering the resonator's resonance frequency f_n and corresponding linewidth δf using [55, 57]

$$Q_L = \frac{f_n}{\delta f}. \tag{3.12}$$

Both f_n and δf can can be derived from the measured resonance curve of the resonator, for further information on the resonance curve see section 3.1.3.

After this general discussion of the Q-factor, the special case of coplanar waveguide resonators is discussed. Two coupling regimes have to be differentiated, namely the over- and undercoupled regime. For a capacitively coupled coplanar waveguide resonator, the external quality factor is mainly determined by the coupling capacitance C_κ, and large coupling capacitances lead to $Q_{\text{ext}} \ll Q_{\text{int}}$ [57]. This is the overcoupled regime of the resonator, where the loaded quality factor is governed by the external quality factor [57], which is reflected in equation (3.11). In particular, this results in the dependence $Q_L \propto C_\kappa^{-2}$ [57]. Consequently, equation (3.12) shows that the resonator's linewidth can be influenced by adjusting the coupling capacitance[2], which is of importance for the design process.

In addition to affecting the linewidth of the resonator, the coupling leads to a shift in the resonance frequency. This is due to the capacitive load, resulting from the capacitive coupling to the feed lines [57]. To show that, the series coupling capacitance C_κ in the equivalent circuit of figure 3.4(a) can be transformed into the parallel capacitance C^* [57], shown in figure 3.4(b). Since C^* is in parallel with the capacitance of the LCR circuit, it alters the circuit's resonance frequency. This results in the equation [57]

$$\omega_n^* = \frac{1}{\sqrt{L_n\,(C + 2C^*)}} \tag{3.13}$$

with $C^* = C_\kappa / \left(1 + \omega_n^2\, C_\kappa^2\, R_L^2\right)$.

For small coupling capacitances compared to the resonator's capacitance[3], such that $C \gg C_\kappa$ and $C^* \approx C_\kappa$, the resonance frequency of equation (3.13) can be Taylor approximated as $\omega_n^* \approx \omega_n\,(1 - C_\kappa/C)$ to estimate the coupling induced resonance frequency shift [57]. As a result, a linear relation between the relative induced frequency shift and the coupling capacitance can be concluded as [57]

$$\left(\omega_n^* - \omega_n\right)/\omega_n = -\frac{C_\kappa}{C}. \tag{3.14}$$

Until now, the mode number n of the resonator mode has only been a side note. However, higher harmonic modes lead to a decreasing quality factor, scaling with n^{-1}

[2] At least until Q_L is not governed by Q_{ext} anymore, which is in the undercoupled regime, when $Q_L \approx Q_{\text{int}}$ [57]

[3] Typical coupling capacitances considered here have fF capacitances, compared with capacitances per length in the $\mathrm{pF\,m^{-1}}$ range and resonator lengths of order 20 mm, cf. section 3.2.1

[57]. As an example, this is shown for one resonator measurement of reference [57] in figure 3.5. This will be used in the resonator design process of section 3.2.2.

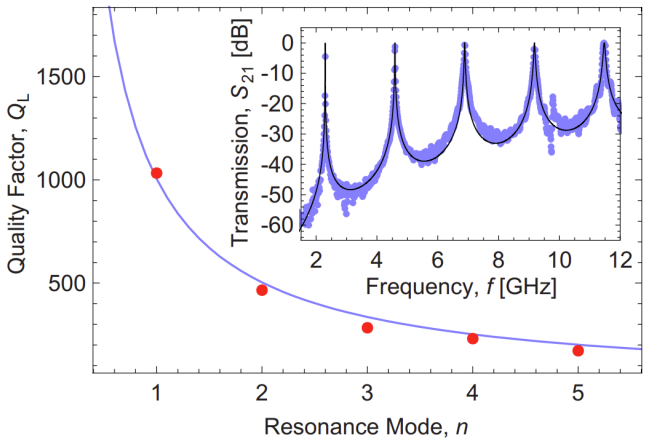

Figure 3.5: Dependence of the loaded quality factor on the resonance mode number n and transmission spectrum of an exemplary coplanar waveguide resonator, image taken from [57]. The plot indicates a decreasing quality factor with increasing mode number of the coplanar waveguide mode. The inset shows the measured resonator spectrum underlying the extracted Q_L dependency of the main plot. The decrease of the loaded quality factor with increasing mode number is clearly reflected in the increasing linewidths in the spectrum.

3.1.3 Scattering parameter

Until now, the analysis of the coplanar waveguide resonators was restricted to the transmission line theory treatment. However, the resonator behaviour can as well be analysed using the scattering matrix theory, shown in reference [57]. This approach allows a complete theoretical description and is especially relevant for practical purposes and measurements using a vector network analyzer. Measuring the scattering parameters can be used to characterize the resonator's resonance frequency and even the quality factor can be obtained that way (cf. equation (3.12)). This description is in general used for a network, or part of a circuit with different inputs and outputs, in the following referred to as ports. In the case of the coplanar waveguide resonator, it can be described as a two port network, where each end of the resonator is one port (see figure 3.3, where each gap can be understood as one port).

The scattering matrix S, given by [55]

$$\begin{pmatrix} V_1^- \\ V_2^- \end{pmatrix} = \begin{pmatrix} S_{11} & S_{12} \\ S_{21} & S_{22} \end{pmatrix} \begin{pmatrix} V_1^+ \\ V_2^+ \end{pmatrix} \tag{3.15}$$

is used to describe the incident V_i^+ and reflected V_i^- voltages of a signal at the two ports of the system with $i \in \{1, 2\}$. In general, the elements of the scattering matrix are defined as [55]

$$S_{ij} = \left.\frac{V_i^-}{V_j^+}\right|_{V_k^+ = 0 \text{ for } k \neq j} \tag{3.16}$$

which means that in order to obtain the scattering parameter S_{ij} only the port j is driven while all other ports do not have any voltages applied, but are terminated with a matched load [55]. So, the scattering parameter S_{11} gives the reflection of a signal at port 1. For the analysis of coplanar waveguide resonators the interesting property is the power that is coupled into the resonator at the input port and transmitted to the output port, i.e. in the notation of the scattering parameters the element S_{21}.

Typically, the Scattering parameters are given in units of decibel, which is obtained by using the expression $20 \log(S_{ij})$ [55].

When the parameter S_{21} of the resonator is measured for a range of frequencies around the resonance frequency, a Lorentzian line shape is obtained [57]. The resonance curve, as obtained with the scattering parameter S_{21} in dB is schematically plotted in figure 3.6 and can be used to calculate the loaded quality factor with equation (3.12). In units of decibel, a decrease of 3 dB from peak transmission is equivalent to a decrease of half the transmitted power. Thus, the difference between the two frequencies around resonance where a 3 dB decrease from peak transmission is found defines the linewidth δf. Further on, the deviation of peak transmission from unity is defined as the insertion loss L_0, which differs for differently coupled coplanar waveguide resonators [57].

This concludes the theoretical introduction to coplanar waveguide resonators. The following section will be devoted to the design of a resonator that meets the requirements for successful experimental integration.

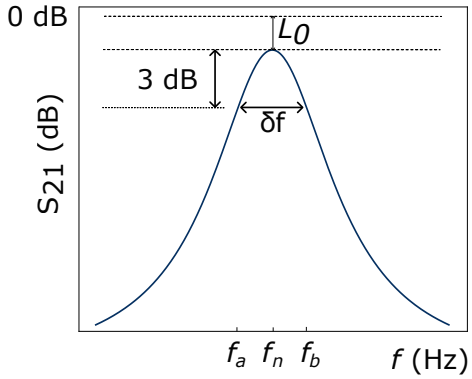

Figure 3.6: Lorentzian resonance curve of the S_{21} scattering parameter (transmission) as a function of frequency around the resonance frequency f_n. The linewidth $\delta f = f_b - f_a$ is defined as the difference between the frequencies around the resonance at which the transmission has dropped by 3 dB, i.e. where half the input power is transmitted. L_0 denotes the deviation from unit transmission, the insertion loss.

3.2 Design of the coplanar waveguide resonator

In the following, the requirements placed on the coplanar waveguide resonator by the experiment are discussed, and the theoretical background introduced in section 3.1 is used to design a resonator to meet these requirements.

The difficulty in the design process lies in the needed precision of the resonator's resonance frequency, which in turn can be influenced by many external influences spanning from the fabrication process to a temperature dependence. Essential for an interaction is the overlap of the resonance curve of the designed resonator with the atomic transition frequency. Details of Rydberg atom properties will be discussed in section 4.2.1 in the context of coupling strength estimations. In order to compensate for deviations from the target frequency, in principle the resonator as well as the atomic transition can be shifted. Tuneable resonators via temperature have been implemented [60] (this principle will be discussed in section 3.2.3) and Rydberg transition frequencies can be tuned using the DC Stark shift [61]. However, since the experiment is still in an early stage at the time of this thesis it is not yet clear to what extent and precision these techniques will be applicable in the first iteration of the experiment.

Although the planned cryostat allows for a comparably fast exchange of samples because repeated baking of the system will likely not be required due to cryopumping, a high throughput of different chips is not intended. Consequently, the design described in the following aims to minimize possible external effects on the resonance frequency

and maximize the chance of achieving the wanted interaction even when the resonator resonance frequency happens to deviate slightly from the target frequency.

As a first step, the geometry of the waveguide has to match a $Z = 50\,\Omega$ impedance, as described in section 3.1.1. Anticipating section 6.1, the chip will be attached to a grounded sample holder and the ground planes of the coplanar waveguide are planned to be connected to the sample holder at the chip sides. To take these circumstances into account, the dimensions are chosen such that the typical impedance would be matched for both cases, i.e. conventional and ground-backed coplanar waveguides. The dielectric substrate will be a $h = 330\,\mu m$ thick sapphire substrate with a dielectric constant $\epsilon_r = 11.6$ [62] and a conducting layer thickness of $t = 500\,nm$ (for the material and dimension choices see section 4.3). The resulting impedance is $Z = 49.8\,\Omega$ for the conventional and $Z = 50.2\,\Omega$ for the ground-backed coplanar waveguide for a trace width of $w = 30\,\mu m$ and a gap $s = 19\,\mu m$. The calculation is done using an online tool [63], which takes the metal thickness into account and states to have corrected typographical errors in its reference book (reference [56]).

3.2.1 Coupling resonator to the feed line

When it comes to the type of coupling the resonator to the feed line, as described in section 3.1.2, different advantages and disadvantages of the respective coupling types have to be evaluated. There are two main points that influence the decision of the coupling type, namely the target Rydberg transition and its corresponding transition frequency.

Due to its advantageous scaling, the target Rydberg transition is supposed to be an electric dipole transition and thus the electric field generated by the resonator is the relevant parameter. Due to symmetry reasons of the chip design, the resonator is therefore expected to have an electric field anti-node at its centre position (which is where the atomcloud will be positioned above the atom chip, see section 4.2). In order to be compatible with most superconducting qubits, a resonance frequency near 6 GHz is aimed for.

The wavelength of a 6 GHz wave propagating along a coplanar waveguide on a dielectric substrate with a dielectric constant near $\epsilon_r = 11.6$ (resulting effective dielectric constant $\epsilon_{\text{eff}} \approx 6.3$) becomes $\lambda' \approx 20\,mm$. As a first note, this length can be squeezed on the planned chip size of 9x9 mm^2, although not in a straight line.

As described in section 3.1.2, for an inductively coupled CPW resonator, the electric field is minimal at the resonator ends. As a consequence of the standing wave condition (equation (3.3)) the fundamental resonator mode has its electric field maximum in the middle of the resonator length. In contrast, the capacitively coupled resonator requires the electric field to be maximal at the resonator ends, which means that the first resonator mode that has an electric field maximum at the centre of the resonator is the $n = 2$ mode, see e.g. the electric field of the fundamental and second harmonic standing wave shown in figure 3.3. The fundamental mode of the capacitively coupled resonator has a

node in its centre and an anti-node at each coupling position. Therefore, the capacitively coupled resonator has to be longer than the inductively coupled one in order to fulfil the requirement of an electric field anti-node in the resonator's centre for a given frequency. However, inductive coupling comes with the effect of having closed loops between the coplanar ground planes and the signal trace, where consequently current can flow. Since the coplanar waveguide will be made of superconducting material, this can become problematic (further information on superconductivity will be given in section 3.2.3). In the case of present magnetic fields during the cooldown of the chip below the critical temperature, persistent currents inside the superconductor can be formed [58], that subsequently lead to persistent magnetic fields that may interfere with the magnetic fields needed to form the magnetic wire trap during the experiment. In other experimental setups this effect is used deliberately to form superconducting persistent current traps which allow for trapping atoms very close to the superconducting resonator surface [40, 58]. However, since the medium-term goal of this experiment is to implement an electromechanical oscillator, which does not have the possibility to form this type of trap, the Z-wire trap will have to be used for the entire duration of the experiment. The chip at hand is supposed to test an experimental procedure that is transferable to later-generation atom chips and thus the implementation of a persistent-current trap on this chip would not be expedient. Consequently, persistent currents as the result of current loops introduced by an inductive coupling would have to be prevented by slitting the ground plane, which complicates the fabrication.

As a conclusion, capacitive coupling is preferred for the given requirements, further supported by the fact that meandering superconducting coplanar waveguides is a widespread technique [39, 59], which overcomes spatial limitations and conveniently allows for the longer capacitively coupled resonator to be squeezed on the chip surface (see section 4.1).

Having decided on the type of coupling, the coupling capacitance has to be set. The coupling capacitance influences the external $Q-$factor and the resonance frequency of the resonator, as described in section 3.2.1. Since the interaction strength is not expected to be limited by the available microwave power (cf. section 4.2), pushing towards a high $Q-$factor is not necessary. Instead, a lower $Q-$factor with a corresponding larger linewidth (cf. section 3.1.2) is advantageous for maximizing the probability of overlapping resonances between Rydberg transitions and the resonator's resonance frequency. Large coupling capacitances can be achieved when interleaved capacitors, in the following called finger capacitors are used. One example of a $3+3$ finger capacitor is shown in figure 3.7, which replaces the gap coupling mentioned before. For the current design, a finger capacitor with $8+8$ fingers is used for a large coupling capacitance. Its dimensions are based on the finger capacitor dimensions used in reference [57]. The finger length is set to a length of 100 µm, each finger has a width of 3 µm and a distance to the next interdigitated finger of 3 µm. Photographs of the on-chip capacitors are shown in section 4.3 in figure 4.15.

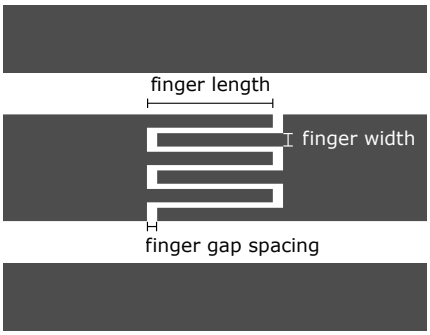

Figure 3.7: Schematic of a $3 + 3$ interleaved, or finger capacitor in top view. The characteristic dimensions of this capacitor are the finger length and width and the finger gap spacing. This type of capacitor can be used to achieve larger coupling capacitances.

For this specific capacitor[4], reference [57] states a coupling capacitance of $C_\kappa = 56.4\,\mathrm{fF}$. For the above-mentioned coplanar waveguide dimensions used for the chip, a capacitance per length of $C_l = 167.161\,\mathrm{pF/m}$ is calculated using [63]. With equation (3.14), to first order this results in a relative frequency shift of $(\omega_2^* - \omega_2)/\omega_2 \approx 1.6\,\%$ and thus for a frequency of $\omega_2 = 2\pi \times 5.818\,\mathrm{GHz}$ leads to an absolute frequency deviation of $\omega_2^* - \omega_2 \approx -95\,\mathrm{MHz}$ from the geometrically designed resonance frequency. That result gives an impression of possible capacitance dependent frequency shifts when using such a capacitor type.

3.2.2 Specifying the resonator length

The resonator length is the main parameter influencing the resonance frequency, as shown in section 3.1. In order to specify the exact length of the resonator, first the exact target frequency has to be chosen.

An operating frequency close to that of state-of-the-art superconducting qubits in the microwave regime [10] would allow a future interfacing with these devices in a quantum network. This gives a range of Rydberg states and transitions to consider. For the compensation of possible frequency deviations, it is convenient to choose a Rydberg transition in such a way, that there exists another Rydberg transition that can be driven with a higher harmonic of the coplanar waveguide resonator. Next to the simple fact of having a second possible atomic target transition, higher harmonics show an increasing linewidth, as shown in section 3.1.2. The Rydberg transitions are supposed to be $n\mathrm{S}_{1/2} \rightarrow n\mathrm{P}_{3/2}$ transitions as a starting point. The corresponding transition frequencies are shown in figure 3.8(a) as a function of the principal quantum number n, where the

[4]Note that the conducting layer height of reference [57] differs from the one of the chip designed in this thesis, which influences the capacitance. The presented values can only serve as an order of magnitude estimation.

quantum defect [64] was taken into account for the calculations.

Given these conditions, suitable transitions can be chosen. For each n_0 of a transition $n_0\mathrm{S}_{1/2} \rightarrow n_0\mathrm{P}_{3/2}$ with transition frequency f_{n_0} a matching transition $n_1\mathrm{S}_{1/2} \rightarrow n_1\mathrm{P}_{3/2}$ with transition frequency f_{n_1}, which minimizes the difference $\delta_{\mathrm{min}} = f_{n_1} - 2f_{n_0}$, is calculated in the interval $n_1 \in [40, 90]$. The resulting minimal differences δ_{min} are shown in the bar plot of figure 3.8(b), which can be understood in the following way. If the mode[5] $n_{\mathrm{res}} = 2$ of a coplanar waveguide resonator is designed to match the Rydberg transition frequency f_{n_0}, the harmonic mode $n_{\mathrm{res}} = 4$ of the same resonator is detuned from the transition frequency f_{n_1} by δ_{min}.

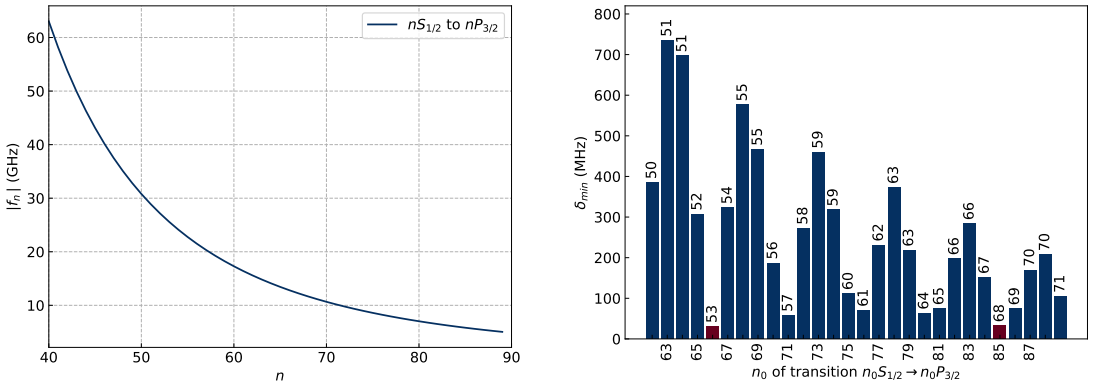

(a) **(b)**

Figure 3.8: Relevant plots for choosing the target Rydberg transitions. In (a) the transition frequencies f_n of transitions $nS_{1/2} \rightarrow nP_{3/2}$ are shown as a function of the principal quantum number n. The bar plot in (b) makes use of the transition frequencies shown in (a). It shows the lowest possible δ_{min} which is the result of minimizing the difference $\delta_{\mathrm{min}} = f_{n_1} - 2f_{n_0}$ as a function of n_0 and depicts the corresponding best match n_1 on top of each bar. Red bars indicate $\delta_{\mathrm{min}} < 50\,\mathrm{MHz}$. For further explanation see main text.

Analysing the possible transitions leads to the choice for the Rydberg transition frequency pair of $n = 85$ with $f_{85} = 5.818\,\mathrm{GHz}$ and $n = 68$ with $f_{68} = 11.668\,\mathrm{GHz}$. These two transitions lead to a $\delta_{\mathrm{min}} = 32\,\mathrm{MHz}$.

Finally, the resonator is primarily designed to match the $f_{85} = 5.818\,\mathrm{GHz}$ frequency. The required resonator length can be calculated with equation (3.4) with $n_{\mathrm{res}} = 2$. However, the resulting length has to be adjusted because of the used interdigitated coupling capacitors, which effectively extend the resonator length. In reference [57], 40 % of each side's finger length had to be added to the geometrically calculated resonator

[5] To avoid confusion of the principal quantum number and the resonator mode number, the latter will be denoted n_{res} throughout this section.

length in order to match the measured resonance frequencies. Conversely, a length of $\delta l = 2 \cdot 0.4 \cdot 100\,\mu\text{m}$, corresponding to two times 40 % of 100 µm long finger, has to be subtracted from the simply geometrical length to match the target frequency, resulting in a final resonator length of

$$l = 20.449\,\text{mm}. \tag{3.17}$$

The process of determining the optimal resonator length for a finger capacitor coupled resonator indicates that the resonator length is not a fixed, precise value for this type of resonator. In order to get an idea of what frequency shifts are possible with respect to length deviations, equation (3.4) can be Taylor approximated around the target length l. To first order, this yields a linear dependence of the frequency shift Δf on possible length deviations Δl like $\Delta f = -k\Delta l$ with the proportionality constant

$$k = n\,\frac{c}{2l^2\sqrt{\epsilon_{\text{eff}}}} = n\,143\,\frac{\text{kHz}}{\mu\text{m}}, \tag{3.18}$$

evaluated for the target length equation (3.17), for the derivation see appendix A.1.

3.2.3 Considerations for superconducting resonators

Until now, the coplanar waveguide resonator has been treated like a normal conducting resonator. However, it will be made of a superconducting material, which comes with some peculiarities. Furthermore, an essential parameter in the context of superconductivity, namely the critical current, has already been addressed in section 2.4.2 in the discussion of the similarly superconducting Z wire.

So, this section first aims at explaining the fundamental basics of superconductivity that are needed for the design considerations for the atom chip at different points in this thesis. After that, special aspects of superconductivity that are relevant for the design of coplanar waveguides will be discussed.

Superconductivity

The hallmark of superconductivity is the lack of electric resistance [54, 65] which means that there is no current-induced joule heating and that an induced current in a superconductor becomes a persistent current without being reduced over time [65]. This phenomenon can be explained by the microscopic Bardeen-Cooper-Schrieffer theory [66], which introduces paired electrons, so-called Cooper pairs, as the current carriers in superconductors. In normal conductors, the cause of resistance is scattering of electrons at the crystal lattice, but this mechanism does not occur with Cooper pairs which results in the current flow without resistance [65]. Furthermore, this has the consequence of a relaxation time $\tau \to \infty$, which is the time that it takes for an electron to come to a stop after it has been scattered [54]. This will be of importance in the next section, because the resulting kinetic energy of the charge carriers leads to a kinetic inductance [67].

The superconducting state is abruptly achieved for a superconducting material, as soon as it is cooled down below a critical temperature T_c [65]. However, next to the temperature, two other critical parameters exist, namely the critical magnetic field and the critical current I_c or critical current density j_c, and all three critical parameters in total depend on each other [65].

One illustration of the interdependence is the close relation between the critical current density and the critical magnetic field. In general, a current that runs through a wire creates a magnetic field around the wire. Let that wire be in a superconducting state, consequently the magnetic field created by that current must not exceed the critical magnetic field in order for the wire to remain superconducting [54]. As it turns out, the current only flows in a small layer λ beyond the surface of the superconductor and as a matter of fact this can be used to calculate the critical current density in that model [54].

The layer thickness λ is also called the penetration depth of the superconductor [54]. That is because it also implicates how far any external magnetic field can penetrate into the superconductor, which is given by an exponential decay with λ as a characteristic length under the prerequisite of the superconductor being in a superconducting state [65]. An external magnetic field induces a current inside the layer of thickness λ, which creates a magnetic field itself and leads to zero magnetic field inside the superconductor [65]. Given that λ is typically small in comparison to the dimensions of the superconductor, it can be concluded that a superconductor in the superconducting phase excludes external magnetic fields entirely and behaves as a perfect diamagnet, a phenomenon known as the Meissner effect [65]. The consequence of the Meissner effect is shown in figure 3.9. As soon as the wire becomes superconducting, it excludes the magnetic field lines, potentially disturbing them significantly.

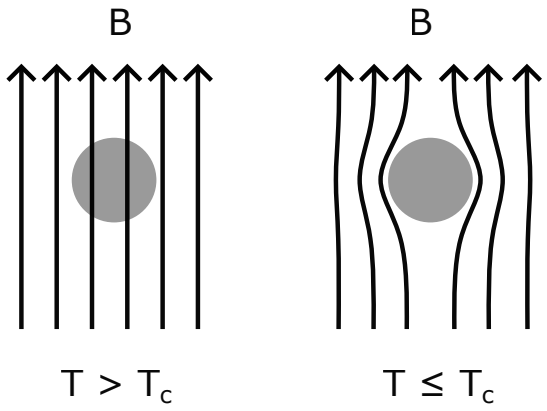

Figure 3.9: Meissner effect demonstrated with a superconducting wire. If the superconductor is in its superconducting phase (here illustrated with a temperature T below the critical temperature T_c) it excludes the external magnetic field B, thereby disturbing the magnetic field lines. Figure adapted from [65].

Superconducting resonators

The resonance frequency of the coplanar waveguide resonator has been shown to scale with $f \propto \frac{1}{\sqrt{L}}$ in equation (3.5). This scaling is important for the understanding of temperature dependent resonance frequency drifts in superconducting resonators.

The inductance per unit length L_l is in general given by [57, 67]

$$L_l = L_l^m + L_l^k \tag{3.19}$$

with L_l^m and L_l^k being the magnetic and kinetic inductance per unit length, respectively. The magnetic inductance depends on the geometry of the resonator in this case and is therefore synonymously called geometric inductance. It is calculated by means of conformal mapping, with equation (3.1) from section 3.1.1. In contrast, the kinetic inductance is a consequence of the inertia of Cooper pairs [57, 67] and has a temperature dependence, that arises from the temperature dependence of the penetration depth [54]

$$\lambda(T) = \frac{\lambda_0}{\sqrt{1 - \left(\frac{T}{T_c}\right)^4}} \tag{3.20}$$

where $\lambda_0 = \lambda\,(T = 0\,)$ and T_c denotes the critical temperature.

Up to temperatures of $T < T_c/2$ the penetration depth remains nearly constant [60, 68], but changes for larger temperatures, exemplarily shown in figure 3.10 for a critical temperature of the used superconducting niobium with $T_c = 9.2\,\mathrm{K}$ [69] (material choices will be discussed in section 4.3). Since the planned cryostat is designed for a temperature of 4.2 K, the $T < T_c/2$ regime is the relevant interval for the planned experiment.

Since λ_0 is known for niobium, the kinetic inductance can be estimated. However, the expression to be considered for the calculation differs for different ratios between superconducting layer thickness and penetration depth. For the chip at hand, the layer thickness will be large compared to the penetration depth, see section 4.3 for the design choice. With that knowledge, the estimation can be conducted, built upon reference [70]. There[6], the kinetic inductance for superconducting coplanar waveguide dimensions of $\lambda^2/t \ll w/2$ and $\lambda \ll t \ll w/2$ is given by the simplified equation [70]

$$L_l^k \approx \frac{\mu_0 \lambda}{4w} g_\epsilon \tag{3.21}$$

with the function g_ϵ being of order unity for typical waveguide dimensions [70]. The kinetic inductance is estimated as $L_l^k = 1.05 \cdot 10^{-9}\,\mathrm{H\,m^{-1}}$ with equation (3.21) for a literature penetration depth of $\lambda_0 \approx 100\,\mathrm{nm}$ [60, 71]. Indeed, the result confirms that the kinetic inductance is about two orders of magnitude smaller than the geometric inductance for the used dimensions (cf. section 3.2) with $L_l^m = 4.14 \cdot 10^{-7}\,\mathrm{H\,m^{-1}}$, calculated with the calculation tool [63]. Hence, the argumentation shows that equation (3.19) can be simplified to $L_l \approx L_l^m$ for chip temperatures $T < T_c/2$ with the design at hand. Furthermore, this also suggests that no significant kinetic induction induced deviation from the geometrically designed resonance frequency is expected in the temperature region that is aimed for in the experiment.

However, if the temperature of the on-chip niobium exceeds $T_c/2$, e.g. due to insufficient thermal conductivity, temperature dependent frequency shifts are expected to become relevant. This effect has been exploited by others, who use the temperature to tune the resonance frequency of their resonator by order of magnitude of several 10 MHz [60].

[6] Note the renaming of the variables in comparison with reference [70], $a = w/2$, $d = t$

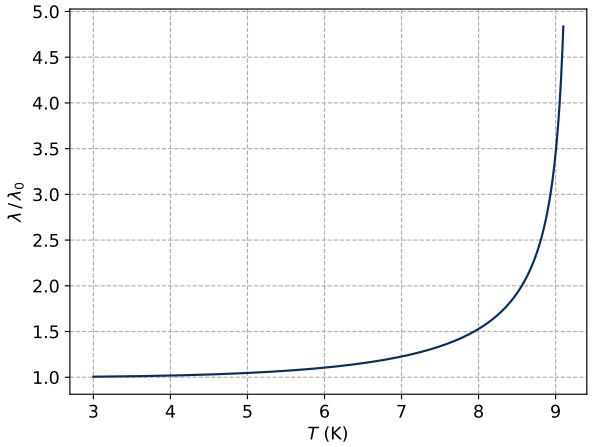

Figure 3.10: Temperature dependence of penetration depth λ of equation (3.20) normalized to the penetration depth at zero temperature λ_0. This shows a steep increase for temperatures increasing above 4.5 K, which is about half the critical temperature of niobium with $T_c = 9.2\,\mathrm{K}$.

3.3 Resonator simulations

The resonator design described in the previous sections draws on analytical expressions, but also on measured data of published resonators. The ability to directly simulate the developed resonator design could provide further insights into the expected properties. Therefore, this section is dedicated to the description of resonator simulations with the Finite Element Method software Comsol Multiphysics [72]. Finite Element Methods build upon the principle to divide a given geometry into smaller areas, in which the equations relevant to the problem are solved. The process of dividing the geometry is called meshing and some problems, in particular problems with propagating waves, are quite sensitive to the mesh and can lead to different results with different meshes [73]. To gain certainty about the obtained results, in principle sophisticated meshing refinement studies have to be conducted, which can get time-consuming and particularly demanding with regard to computational power. Therefore, the results of the simulations shown in this section are intended as a first exploration of the possibilities of resonator simulations, rather than serving as a design guide in the present state of simulation.

3.3.1 Eigenfrequency analysis

The eigenmodes and eigenfrequencies of a straight coplanar waveguide are subject of this section. The dependence of the resonance frequency on the resonator length is in principle well-covered by the theory, as confirmed by measurements in reference [57]. In

contrast, the additional length added by the finger length of finger coupling capacitors alters the resonance frequency, which is corrected by means of empirical measurements, which was mentioned in section 3.2.2. This is further supported by reference [56], which emphasizes that no design equations are available for interdigitated capacitors. This suggests, that simulations of the actual resonator geometry could have an advantageous impact on the design process.

For the first simulation, a straight and capacitively coupled resonator of the length stated in section 3.2.2 is taken as geometry. In principle, a meandering resonator like the actual resonator designed for the chip could be used, as well. However, the additional turns mainly complicate the meshing procedure while no physical differences between the straight and meandered resonator are expected, as long as a sufficient meandering distance is considered (see section 4.1). The simulated resonator is coupled via simple gap capacitors (see e.g. figure 3.3) to put the focus on the resonator length in the initial simulations. The mesh is computed with an automatic preset and the waveguide excitation is achieved with the Lumped Port element of the Electromagnetic Waves, Frequency Domain module. The length of the resonator is chosen to be the same as for the actual resonator without finger capacitor coupling, which is $l = 20.529\,\mathrm{mm}$. This results in the eigenmodes shown in figure 3.11. The modes show the electric field distribution that is theoretically expected from the boundary conditions of capacitively coupled resonators with anti-nodes at the coupling capacitors. However, even with the same substrate dielectric constant used for the resonator length calculations in section 3.2.2, the simulation yields a resonance frequency of $f_2 = 5.711\,\mathrm{GHz}$ for the $n = 2$ mode shown in figure 3.11(b). This deviates from the calculated resonance frequency of $5.818\,\mathrm{GHz}$ (see section 3.2.2) by $107\,\mathrm{MHz}$.

Ultimately, both models, i.e. the resonator design presented in section 3.2.2 and the simulation contain uncertainties like empirical data and idealized material assumptions, for example. Consequently, a reliable evaluation of these results requires comparison with prospectively measured resonance frequencies of the actual device.

3.3.2 Scattering parameter simulations

The resonator's characteristic resonance frequency and linewidth are important parameters to be considered in the resonator design process. As described in section 3.1.3, the resonance curve of a resonator can be obtained by measuring its scattering parameters. In the simulation, this is done by a frequency domain source sweep, which means that the excitation port is used to drive the resonator with different frequencies around the resonance frequency and calculate the corresponding S_{21} parameter.

The coupling capacitance of the resonator influences the resonance frequency by adding a capacitive load to the resonator, as pointed out in section 3.1.2. This dependency has been measured experimentally in reference [57]. To test the simulation capabilities, it is supposed to reproduce this dependency. Therefore, six capacitively coupled resonators

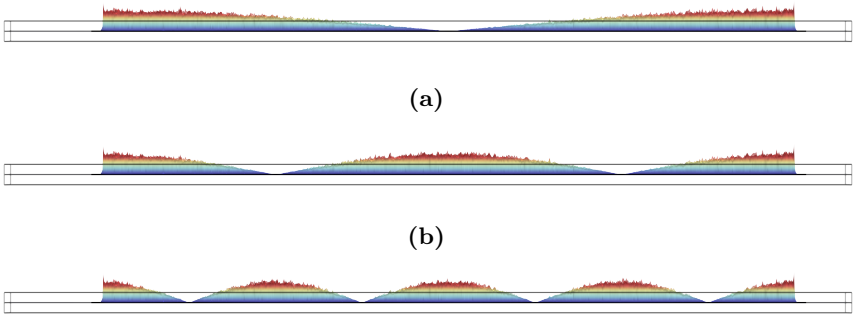

(a)

(b)

(c)

Figure 3.11: Fundamental and higher harmonic eigenmodes of the capacitively coupled coplanar waveguide resonator found in an eigenfrequency analysis simulation. The plot shows the electric field amplitude of the standing wave inside the resonator, the shown colour corresponds to the electric field norm in arbitrary units. The simulation yields a result of $f_1 = 2.854\,\mathrm{GHz}$ for the fundamental resonator mode shown in (a). In (b) the $n = 2$ and in (c) the $n = 4$ resonator mode is shown.

are simulated. The three gap capacitors have a decreasing gap distance, while the three finger capacitors have an increasing number of fingers. This allows for an increase in coupling capacitance per device [57]. Apart from the coupling capacitors, the same resonator geometry is used as in the previous section 3.3.1. All resonators are driven with an input voltage of 1 V at a characteristic impedance of 50 Ω.

The simulation result is shown in figure 3.12. As expected from the data in reference [57], the S_{21} parameter, corresponding to the transmission from port 1 to port 2, shows a clear trend of larger insertion losses for the weakly coupled gap capacitors, while the transmission of the strongly coupled resonators with finger capacitors almost reach unit transmission. This is consistent with the measurements presented in reference [57]. Furthermore, the linewidth of the finger capacitor coupled resonators is visibly larger than that of the gap capacitor coupled resonators, which in turn means a decrease of the loaded quality factor (see equation (3.12)) and is in line with the theoretical expectations, as well.

However, the shift towards lower resonance frequencies with increasing coupling capacitances, stated in equation (3.14), is not confirmed by the simulation. Instead, no clear dependency can be derived from the simulation results. A likely cause is the already mentioned meshing problem. The mesh has to get very fine around the finger coupling capacitors, but with the standard meshing presets, this cannot be achieved because of the vastly increasing memory demand, which exceeds the available computational resources. As a consequence, a more sophisticated manual meshing procedure would be required for more reliable results. Furthermore, a mesh refinement study would be needed, i.e.

running the simulation with increasing mesh fineness to confirm the convergence towards one result.

As a conclusion, direct resonator simulations seem possible in principle with this simulation configuration as some of the theoretical expectations could be fulfilled. However, the important parameter of the exact resonance frequency appears to be quite mesh-sensitive. Thus, for quantitatively reliable simulations further efforts have to be made in developing a sophisticated meshing procedure.

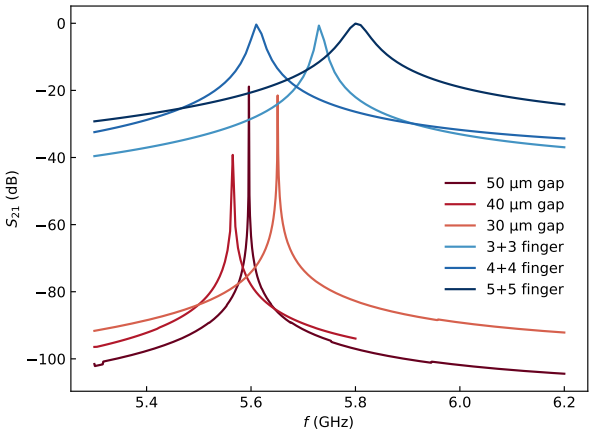

Figure 3.12: Simulation of the S_{21} parameter as a function of frequency around resonance of six coplanar waveguide resonators with increasing coupling strength. Decreasing gap distances correspond to an increase in coupling capacitance, the same applies for an increase in the number of fingers for finger capacitors. The strongly coupled finger capacitors show visibly larger linewidths and near unit transmission, as theoretically expected. However, no consistent dependence of the frequency shift on the coupling capacitance can be derived from the shown results.

Chapter 4

The atom chip

The previous chapters introduced the two structures, the Z wire for magnetic trapping and the coplanar waveguide resonator, that are supposed to be integrated onto the chip. The concept of magnetic trapping was introduced, and it was discussed how loading the on-chip trap from the magnetic transport can be done. Furthermore, the coplanar waveguide was shown and how it can serve as a microwave resonator.

Now, both of these concepts have to be brought together in order to specify how the atom chip layout can be designed to facilitate Rydberg excitation and subsequent coupling between the microwave resonator and the Rydberg atoms.

In order to choose a chip design certain considerations must be made. The size of the chip is limited by the dimensions of the cryostat, but at the same time the microwave resonator must have a certain length and be located within a certain distance to the Z wire on the chip that creates the magnetic trap.

This chapter first presents these requirements of the chip layout, and then introduces and discusses the chosen chip layout. The parameters determined by the chosen layout are then used to calculate the possible coupling strength between the on-chip microwave resonator and ultracold atoms trapped by the magnetic wire-trap.

Finally, the chip fabrication itself will be described, including the chosen materials, layer thicknesses and the general fabrication process.

4.1 Chip layout

The final chip will have a surface area of 11x11 mm^2, but with a clearance of 1 mm all around, which makes an effective area of 9x9 mm^2 that can be used for the layout. The layout that will be fit into this area has to meet two essential requirements. On the one hand, both the trapping Z wire and the coplanar waveguide resonator have to fit on the chip with the correct relative position to each other in order to facilitate interaction. On the other hand, both structures have to be contacted electrically at both beginning and end, each. Contacting such a chip electrically is typically done via wire bonds [39]. These are small diameter wires which are pressed onto the chip surface on the one side and onto another contact on the other side, typically a printed circuit board (PCB) (see section 6.2). The contact areas are called bond pads and for the coplanar waveguide they arise from the widening of the central trace, which is shown in figure 4.1. All bond

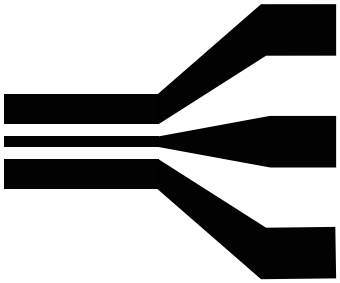

Figure 4.1: Coplanar waveguide widening into wider pads, so-called bond pads, for wire bonding to a PCB.

pads have a width of 200 µm without exception, the spacing between ground planes and trace is set to 200 µm for the coplanar waveguide bond pads for impedance matching[1]. To achieve proper grounding of the chip surface, not only the coplanar waveguide ground pads can be bonded to the PCB ground, but also the gold layer on the chip (the purpose of the gold layer will be discussed in greater detail as part of the fabrication process in section 4.3) can be bonded to the PCB ground pads and the sample holder itself. Larger bond pads of up to 400 µm (e.g. used in reference [39]) prove to be hard to achieve with respect to reasonable impedance matching when a properly grounded reference plane has to be considered.

So, for the chip layout the bond pads give one constraint on space. To avoid disturbing wire currents that could influence the magnetic trap, the Z wire will have its start and end at two opposite edges of the chip. Another constraint comes from the length of the resonator that has to be correct to support a standing wave at an appropriate frequency that fits to the Rydberg state of interest (see section 3.2.2). Furthermore, the anti-nodes of the electric field on the resonator must coincide with a position where atoms can be trapped by the Z wire trap. To achieve the overlap between the trap-position and the E-field anti-node and have the correct resonator length, the resonator is designed in meandering fashion. The distance between two neighbouring coplanar waveguide transmission lines, e.g. due to meandering, should amount to about seven times the width of the coplanar waveguide (i.e. $7 \times (w + 2s)$ [39] with the trace width w and gap spacing s, see section 3.1.1) to minimize parasitic capacities [39].

The layout shown in figure 4.2 is exactly chosen such that the centre bar of the Z wire coincides with a section of the microwave resonator where there is an anti-node, given the constraints mentioned above.

[1] This configuration results in a 50 Ω impedance for a ground-backed coplanar waveguide in the bonding regions.

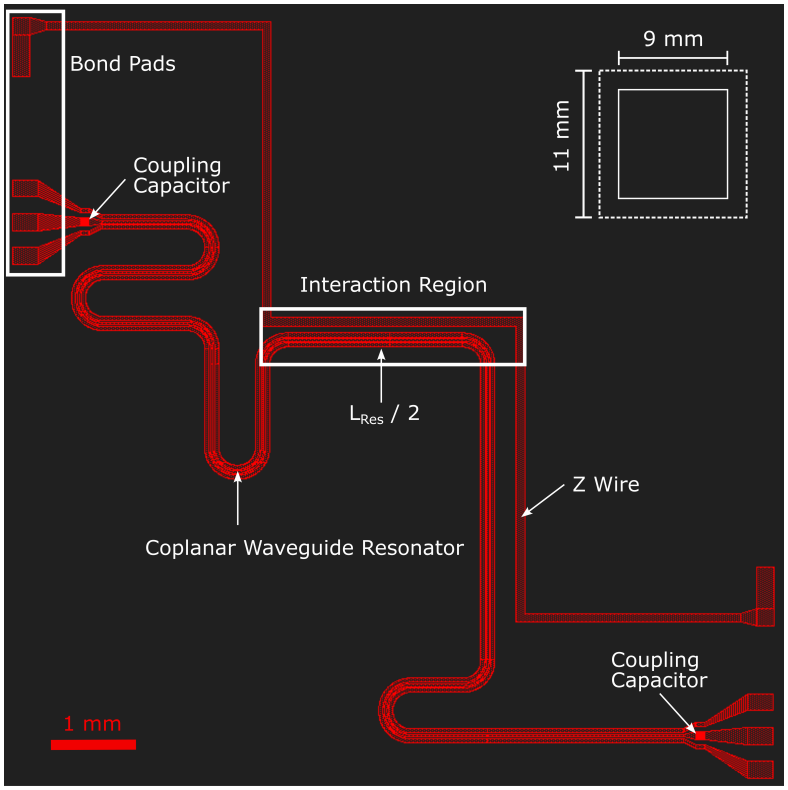

Figure 4.2: Exact atom chip layout with Z wire and coplanar waveguide resonator. The shown structures extend over an area of 9x9 mm^2, while the chip itself is larger by a clearance of 1 mm around the structures, as indicated by the dashed lines of the inset. The bond pads of both structures are found on the left and right side of the chip, on the left side they are highlighted by the white box. The length of the coplanar waveguide between both coupling capacitors determines the resonator length and is designed in such a way that the centre of the coplanar waveguide resonator coincides with the centre of the central Z wire bar, which determines the interaction region between resonator and trapped Rydberg atoms.

The shape of the electric field and the centre anti-node is shown in figure 4.3 for the $n = 2$ resonator mode as a function of the resonator length. The plot assumes a sinusoidal standing wave with its maximum at the origin due to the capacitive coupling of the resonator. If the magnetic trap centre and the centre of the anti-node coincide like that, figure 4.3 shows that the electric field varies 10 % along the trap extension. Ideally, the field would be homogeneous along the complete trap for homogeneous coupling strengths, but this variation is acceptable.

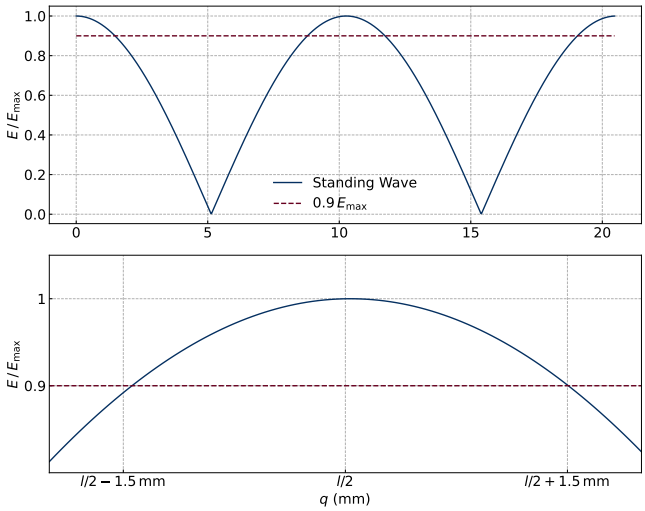

Figure 4.3: Normalized electric field $E/E_{\max}$ distribution of the standing wave inside the resonator as a function of the position along the resonator, denoted as q. The upper plot shows the electric field distribution over the total resonator length $l \approx 20.5\,\text{mm}$. The electric field is assumed to be sinusoidal with anti-nodes at the beginning $q = 0\,\text{mm}$ and end of the resonator $q = l$. The lower plot shows the normalized electric field amplitude as a zoom in of the upper plot in the 3 mm long interaction region, where the trapped atoms will sit. The peak amplitude of the anti-node is positioned at half the resonator length and the intersections of the horizontal line at $0.9E_{\max}$ with the electric field curve indicates an electric field amplitude variation of 10 % along the interaction region.

The lateral distance between the Z wire and the centre trace of the coplanar waveguide resonator of the chip layout in figure 4.2, is chosen with respect to two different considerations. Firstly, the coplanar waveguide is positioned at some lateral distance to the Z wire centre, but the magnetic trap is supposed to be rotated above the resonator centre, so the distance should be in a feasible rotating distance (this will be discussed in section 4.2 below).

Secondly, given that both the Z wire and the resonator will be made of superconducting material, it is essential that the distance between them is sufficiently large to prevent the

superconducting structures from disrupting the magnetic fields required for the magnetic trap, due to the Meissner effect (see section 3.2.3 for the Meissner effect). Indeed, the experience of other groups with superconducting atom chips has shown, that too much surface covered with superconductors leads to significant disturbances of the magnetic field, which is why they replaced large parts of the chip surface with a normal conducting material [60]. Therefore, the design at hand aims at minimizing the surface covered with superconducting material and leaves the Z wire and resonator as the only superconducting structures. Since microwave power will not be a limiting factor in this experimental setup, which will be shown in the next section, microwave losses due to smaller superconducting coplanar grounds can be tolerated. Therefore, a lateral dimension of 215 µm between the centre of the central Z wire bar and the trace centre is chosen (see e.g. figure 4.9, where this value is used for the trap positioning).

Replacing parts of the superconducting material with normal conducting material instead of keeping the bare dielectric substrate serves two purposes. On the one hand, it leads to a completely grounded chip surface by having a galvanic connection between normal and superconducting parts, which prevents parasitic resonances when exciting the resonator [60]. On the other hand, metallic coating of the dielectric surface is needed in the vicinity of Rydberg atoms. Due to the strong sensitivity of Rydberg atoms to stray electric fields (which will be discussed in section 4.2.1), surface charges of the dielectric can lead to disturbances.

It should be noted that even the current-carrying Z wire is galvanically connected to the normal conducting layer, but because of the superconducting nature of the Z wire, the path of least resistance is given along its course. Furthermore, this connection could prevent the Z wire from melting in the event of an uncontrolled breakdown of superconductivity when the normal conductor becomes the better conductor compared to the superconductor material in a non-superconducting state. In addition, this connection grounds the Z wire potential, preventing the negative pole of the DC power supply from being at floating potential.

4.2 Coupling strength

With the final chip layout in figure 4.2 being set, the expected coupling strength can be calculated. Until now, ^{87}Rb atoms have been trapped in their ground state. However, the ground state is virtually insensitive to electric fields [32] and therefore inadequate for the desired atom-resonator coupling. Hence, the on-chip trapped ^{87}Rb atoms will be excited to a Rydberg state, which in contrast is very sensitive to the electric field and facilitates the desired coupling. The properties of Rydberg atoms will be discussed in the next section and it will provide an equation to calculate the coupling strength. The coupling strength depends on the electric field strength at the position of the atoms generated by the resonator and the electric dipole moment of the transition in question.

To prepare the electric field calculation, section 4.2.2 will discuss the final relative position of atoms and resonator. After that, the electric field generated by the resonator will be obtained by means of a simulation before eventually the expected coupling strength can be estimated.

4.2.1 Rydberg atoms

Rydberg atoms are atoms with at least one electron in a state with a high principle quantum number n [32]. A useful tool for understanding Rydberg atoms is the Bohr model [32]. Electrons with large principal quantum number relate to orbits in the Bohr model that are far away from the nucleus. This large electron - nucleus distance comes with interesting atom properties, discussed in the following.

The energy between adjacent Rydberg states scales with n^{-3} [32], which results in transitions in the GHz regime, corresponding to microwave wavelengths, between neighbouring Rydberg states for large n. These states are the transitions of interest for the planned experiment.

Additionally, the electric dipole moment $d = \langle e|er|g\rangle$ for transitions between two states $|g\rangle$ and $|e\rangle$ scales with n^2 [32]. This leads to large electric dipole moments for higher Rydberg states, which is an advantageous scaling for the interaction between the atoms and the resonator, because the coupling strength [20]

$$g = -\frac{dE}{2\pi\hbar} \tag{4.1}$$

scales with the electric dipole moment d and the electric field E.

Further, the polarizability of the Rydberg atom scales with n^7 [32], which makes the atoms very sensitive to electric fields. This leads to large possible Stark shifts caused by electric fields [32].

Finally, the valence electron of a Rydberg atom is so loosely bound that it can be readily ionized by an applied electric field [32]. This property will be exploited for Rydberg atom detection in section 6.3.2.

In the experimental setup, Rydberg atoms are produced in a photo excitation scheme, using two lasers. These are the probe and control laser with wavelengths of 780 nm and 480 nm, respectively, see figure 4.4.

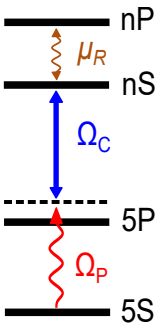

Figure 4.4: Two photon excitation for production of a ^{87}Rb Rydberg atom. The 780 nm probe laser with Rabi frequency Ω_P and the 480 nm control laser with Rabi frequency Ω_C excite the ^{87}Rb $5S$ ground state to a nS Rydberg state. μ_R denotes the electric dipole moment between the neighbouring nS and nP Rydberg states.

4.2.2 Positioning the atoms above the resonator

To achieve the best possible coupling, the atoms have to be positioned above the coplanar waveguide resonator. The layout designed in section 4.1 already ensures sufficient electric field amplitudes along the waveguide in the interaction region, demonstrated in figure 4.3. Now, the position along the two remaining coordinate axes has to be specified. Ultimately, the following process will have to be verified experimentally and revised if necessary, but for now one appropriate procedure is simulated.

In chapter 2, the Z wire trap was positioned directly above the coplanar waveguide, with a magnetic bias field B_z parallel to the chip surface. However, it is possible to rotate the trap away from above the Z wire towards the side of it, which is where the resonator is positioned in the chip layout.

The trap can be rotated to that position by applying an additional magnetic bias field component perpendicular to the chip surface, which is exemplarily shown in figure 4.5.

For this demonstration of the rotation, the B_z component is kept at a constant value of 6 G and the wire current is set to constant $I_w = 2$ A, while the perpendicular component is increased as $B_y \in \{0, 2, 5, 8\}$G. As a consequence, the trap is rotated and gets smaller as well, which means larger trap frequencies. Larger trap frequencies in turn result in a compression of the trap, which can lead to heating of the atom cloud [44]. Consequently, maintaining comparable trap frequencies during the rotation process is preferable in order to avoid heating. That can be achieved by slightly decreasing the parallel component of the magnetic bias field while increasing the perpendicular one.

Using the fact that rotation is possible with an additional bias field, the final trap position is specified. The position of the Z wire is placed at the origin and thus the centre

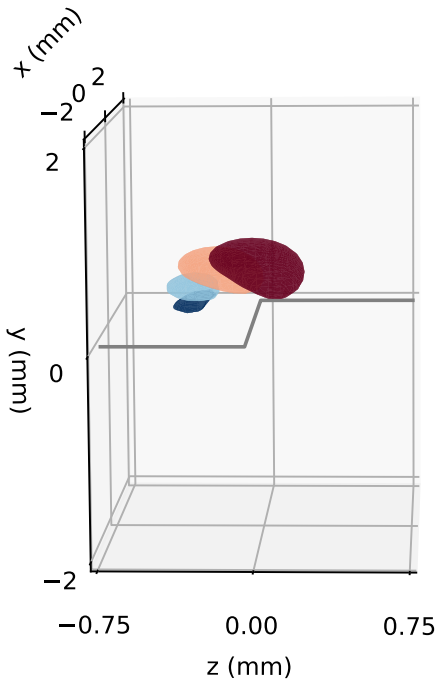

Figure 4.5: Rotation of the 100 µK isosurface around the Z wire by increasing the magnetic field component perpendicular to the chip surface with $B_y \in \{0, 2, 5, 8\}$G and keeping the chip-parallel magnetic field component $B_z = 6$ G and the wire current $I_w = 2$ A constant.

of the coplanar waveguide trace is located at the position $\vec{r} = (0, 0, -215)$ µm. In that frame, the trap will be placed at the position $\vec{r} = (0, 400, -240)$ µm, which is slightly off-centre from the trace centre. The lateral position of the trap is rather insensitive, if the trap is not located directly above the waveguide, since at a certain height the electric field is reasonably homogeneous. This will also be visualized in section 4.2.3.

The final rotated trap geometry that is chosen here, is shown in figure 4.6 in both two and three dimensions. These plots also show the probe beam of the Rydberg excitation setup (see section 4.2.1), which is tightly focussed and smaller in diameter than the trap geometry. The Rydberg excitation lasers have to be aligned with the trap position in order to enable Rydberg excitation. In the experimental setup, the relative position of the final trap position and excitation laser axis will be adjusted with a coarse degree of precision by moving the sample holder with the attached chip over a translation stage.

Fine-tuning of the position will be achieved via the trap parameters.

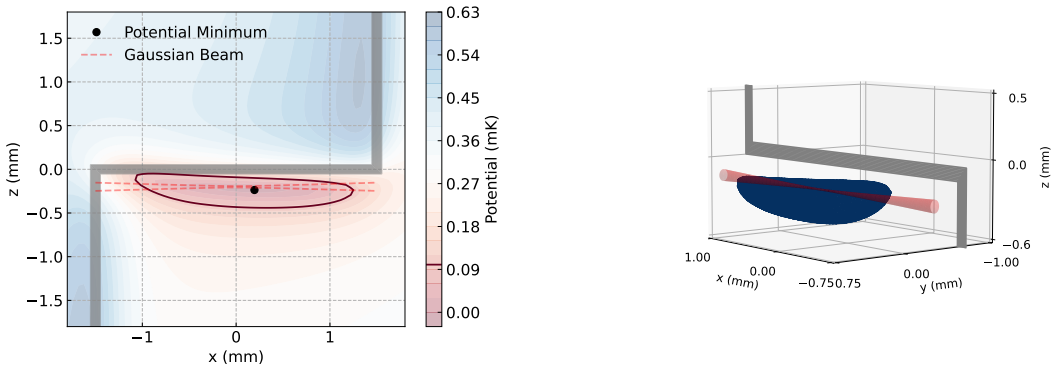

(a) **(b)**

Figure 4.6: Final trap position after rotation around the gray Z wire. Both images additionally show the probe beam of the Rydberg excitation setup. In (a) the two-dimensional potential landscape in the xz plane at the y position of the minimum is shown. Furthermore, the 100 µK isopotential line is depicted, and the dashed red line shows the probe laser beam shape. (b) shows the three-dimensional trap geometry of the 100 µK isosurface along with the probe beam. With both images together, the rotation around the central Z wire bar becomes clearly evident.

The rotation of the magnetic trap from above the Z wire to its final position can be achieved with a linear ramping sequence, which is shown in figure 4.7. The ramped bias field B_y is perpendicular to the chip surface and rotates the trap position away from directly above the wire. In addition to the ramping of the perpendicular bias field, the wire current is reduced during this sequence, which brings the trap closer to the chip surface. Since both the additional bias field and the lower current lead to increased trap frequencies, the initial parallel bias field is lowered as a compensation mechanism at the same time.

As a result, the final Z wire trap has slightly increased trap frequencies of $\omega_r = 2\pi \times 260\,\mathrm{Hz}$ in the radial (y and z) and $\omega_{\tilde{x}} = 2\pi \times 12\,\mathrm{Hz}$ in the axial direction, when compared to the initial trap frequencies. Note, that this is one possibility among others to place the trap, which was chosen here with the aim to achieve large coupling strengths. If it turns out experimentally, that this sequence heats up the atom cloud significantly or that another trap position would be more advantageous, the sequence can be readily refined using the scaling laws of equation (2.5). For example by increasing the wire current or decreasing the bias field strength as long as the trap depth remains deep enough.

To investigate the behaviour of atoms in that trap during the sequence, a dynamic simulation is run for the complete sequence of figure 4.7. Complete sequence means

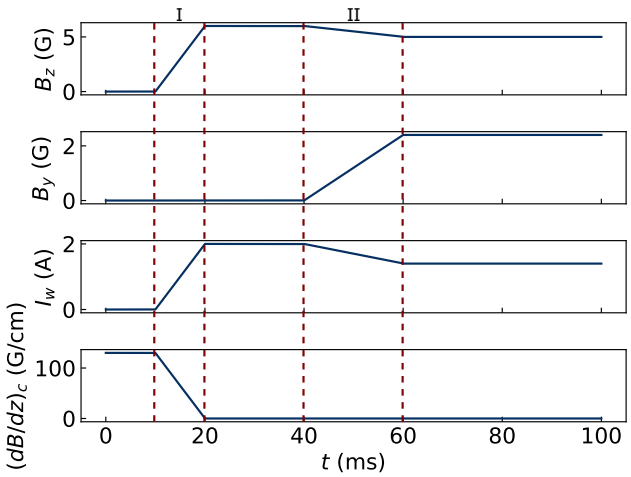

Figure 4.7: Complete atom chip loading sequence. In interval (I), the atoms are transferred from the quadrupole trap to the Z wire trap by ramping of the involved parameters. For the quadrupole trap it is the magnetic field gradient $(dB/dz)_c$ of the transport coil which is influenced by the coil current and for the Z wire these are the wire current I_w and the bias fields B_z and B_y. The B_y bias field is needed in step (II) for rotating the trap over the resonator. For further information see main text.

starting from atoms in a quadrupole trap that are loaded into the on-chip trap and finally rotated over the resonator. The results of the simulation are shown in figure 4.8, the y and z coordinates determine the position above the coplanar waveguide structure. This shows the initial distance between atoms and chip surface of about 700 µm, where the transfer is performed. The blue lines in figure 4.8(a) and figure 4.8(b) indicate the calculated trap minimum for the final trap configuration, which is where the atoms oscillate around.

The z component describes the position relative to the Z wire (located at $z = 0$) and is needed to estimate the position above the coplanar waveguide, shown in figure 4.8(b). The y component serves the same purpose, shown in figure 4.8(a), since it is equal to the distance from the chip surface and directly defines the coupling strength since the electric field strength decreases with increasing distance to the resonator. The electric field calculation will be discussed in the following.

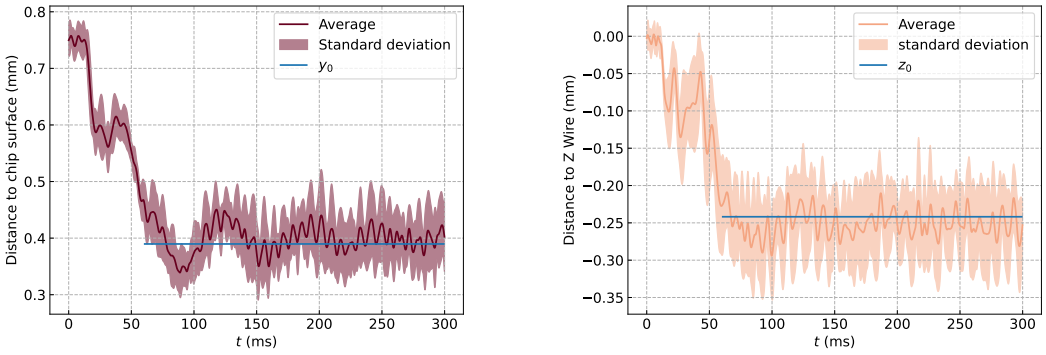

(a) **(b)**

Figure 4.8: Resulting mean atom coordinates of a dynamic simulation with trapped atoms during the sequence shown in figure 4.7. In (a) the y coordinate (atom to chip surface distance) and in (b) the z coordinate (relative position of resonator and atoms in chip-plane) coordinates are shown along with one standard deviation. The blue lines indicate the position of the calculated trap minima at the final trap position. So, here the simulation shows how the atoms reach this position after the complete process of chip-loading and trap rotation until they oscillate around the final trap minimum.

4.2.3 Calculation of the electric field above the resonator

Now, the final trap position is specified and the coordinates for the horizontal and vertical position relative to the waveguide can be used to calculate the electric field that is created by the resonator at this final trap position.

Since the distance between resonator and atoms is way smaller than the wavelength of the microwave, the coupling takes place in the near field and a static electric field simulation is applicable. For the simulation, a certain voltage is applied to the trace of the coplanar waveguide. The resonator leads to a resonant enhancement of the applied voltage, that depends on its Q-factor, and thereby resonantly enhances the created electric field in the resonator. That is why the resonant enhancement factor has to be estimated in order to obtain reasonable results for the coupling strength. On resonance, the average electric and magnetic energy in the resonator are equal [55], oscillating back and forth between maximal magnetic and maximal electric energy. As a consequence, for a given moment in time, when the oscillating voltage of the standing wave inside the cavity reaches its maximum, the total energy in the resonator E_{res} is stored in the electric field only. Thus, the effective voltage on the resonator trace $U_{\mathrm{res,eff}}$ can be calculated using [40]

$$\frac{1}{2} C U_{\mathrm{res,eff}}^2 = E_{\mathrm{res}} \tag{4.2}$$

with the total capacitance $C = C_l l$ of the resonator. Furthermore, the peak voltage of a running wave on the same transmission line is given by $U_\mathrm{p} = \sqrt{2PZ}$ with the microwave power P and the transmission line impedance Z. In general, the peak voltage U_p of a sinusoidal signal depends on the effective voltage U_eff like $U_\mathrm{p} = \sqrt{2}\,U_\mathrm{eff}$, which will be taken into account in the following steps.

The total energy in the resonator links to the Q-factor via the relation given in equation (3.10), here reordered to

$$E_\mathrm{res} = \frac{QP_\mathrm{in}}{\omega} \tag{4.3}$$

and evaluated on resonance, which means with the resonance frequency ω, the total energy stored in the resonator E_res and the power loss P_loss of equation (3.10), but where $P_\mathrm{loss} = P_\mathrm{in}$ on resonance [55].

Now, the peak voltage in the resonator $U_\mathrm{res,p}$ that is obtained after solving equation (4.2) for $U_\mathrm{res,eff}$ and scaling the result with the factor $\sqrt{2}$, can be compared to the peak voltage on the free transmission line, i.e.

$$\frac{U_\mathrm{res,p}}{U_\mathrm{p}} = 2\sqrt{\frac{Q}{\omega C Z}}, \tag{4.4}$$

which is the resonant enhancement factor. Alternatively, the resonantly enhanced peak voltage on the resonator trace can be calculated directly from equation (4.2) with equation (4.3) as

$$U_\mathrm{res,p} = \sqrt{\frac{2QP}{\omega C}}. \tag{4.5}$$

Since the chip is still being manufactured at the time of this thesis, the expected resonant enhancement and resulting coupling strength can only be estimated with literature values. The resonator closest to the one designed for the designated chip is characterized in reference [57], which is a superconducting aluminium resonator with symmetric capacitive $8 + 8$ finger coupling, operated well below the critical temperature of aluminium. The measured loaded quality factor for this resonator is stated to be $Q_L = 370$, which is used for the following calculation. Accordingly, this estimation has to be treated as an order of magnitude estimation only.

Finally, the electric field above the resonator is simulated with the AC/DC module of the Finite Element Method program Comsol Multiphysics [72].

In figure 4.9, the final trap position is schematically drawn into the simulated electric field above the resonator in a two-dimensional cross-section. The cross-section contains the trace of the waveguide at $z = -215\,\mu\mathrm{W}$ and the Z wire centre at $z = 0\,\mu\mathrm{m}$, which corresponds to the coordinates introduced in the previous section. It further stresses the aforementioned point that the electric field along the lateral, i.e. z position above the resonator is rather homogeneous starting from a certain height (around $200\,\mu\mathrm{m}$ for the

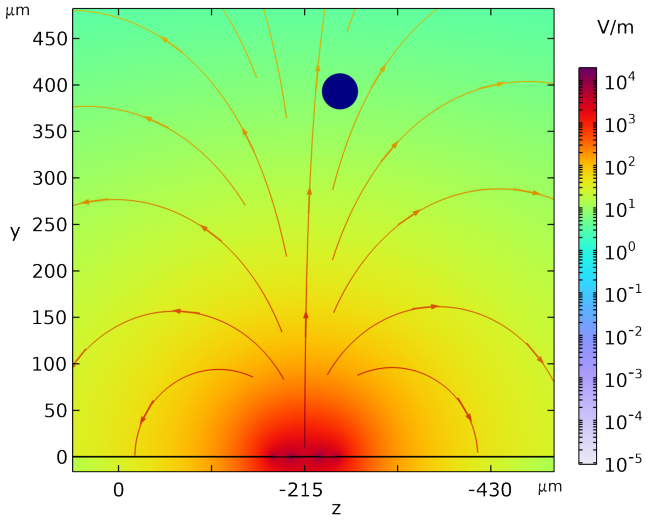

Figure 4.9: Simulated electric field above the coplanar waveguide in a cross-sectional cut for an assumed input power of $P_{\text{in}} = 1 \cdot 10^{-3}\,\text{mW}$, which corresponds to an applied voltage of $U_{\text{res, p}} = 0.107\,\text{V}$ to the central trace (see text). The blue circle indicates the final trap position schematically, the position of the Z wire is at $z = 0$ and the centre of the coplanar waveguide trace is located at $z = -215\,\mu\text{m}$. The black line in the bottom indicates the boundary of the used coplanar waveguide geometry, not identifiable on the shown scale.

simulation shown here). As a consequence, the exact lateral trap position has a rather reduced influence on the coupling strength.

The depicted electric field strength was obtained by applying a voltage of $U_{\text{res, p}} = 0.107\,\text{V}$ to the waveguide trace, which calculated using equation (4.5) for an input power of $P_{\text{in}} = 1 \cdot 10^{-3}\,\text{mW}$. For that, the needed capacitance C was obtained by calculating the capacitance per unit length with, using reference [63], which yields $C_l = 1.7094 \cdot 10^{-10}\,\text{F/m}$ and multiplying it with the resonator length. Taking the $n = 85$ target Rydberg state transition frequency of $\omega = 2\pi \times 5.818\,\text{GHz}$ yields the initially stated peak voltage used in the simulation. The two-dimensional cut is made at the exact position of the standing wave's electric field anti-node maximum (i.e. at the position of $l/2$ in figure 4.3), which justifies the simulation with the calculated peak voltage. The corresponding resonant enhancement factor of the resonator can be obtained by repeating the aforementioned calculation with equation (4.4) and $Z = 50\,\Omega$. It yields a resonant enhancement factor of 10.7 for the $n = 85$ Rydberg state transition and 7.6 for the $n = 68$ Rydberg state transition. The difference corresponds to a factor $\sqrt{2}$ difference, which results from driving the resonator with the two different frequencies.

For a given position above the resonator, the electric field generated by the resonator at that distinctive position is proportional to the applied voltage. This allows to extract

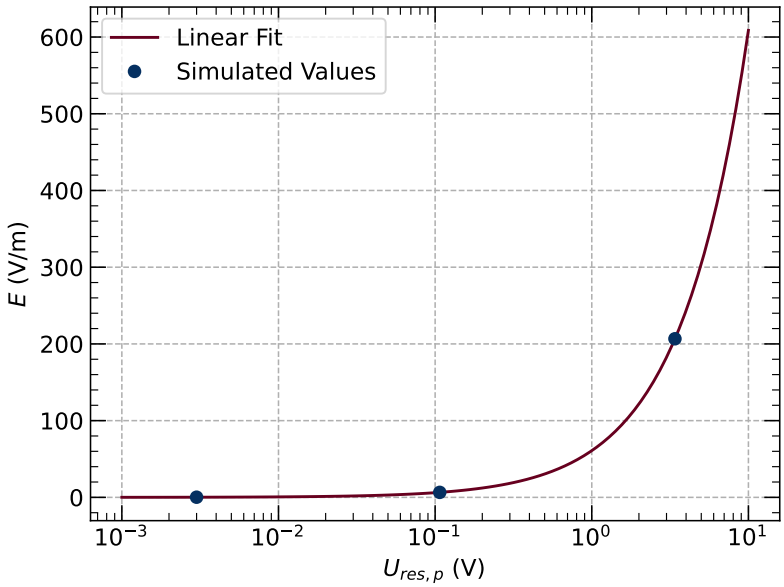

Figure 4.10: Linear dependence of the electric field norm E at the trap position on the resonantly enhanced peak voltage $U_{\mathrm{res,p}}$. It is given in a semi logarithmic representation to cover several orders of magnitude of resonantly enhanced peak voltages. The curve is the result of a least square fit to a linear function in the semi logarithmic representation.

the electric field dependence at the trap position on the trace voltage by simulating the electric field norm at the trap position for three different applied voltages of $U_{\mathrm{res,\,p}} \in \{0.003, 0.107, 3.396\}\mathrm{V}$, which correspond to input powers of $P_{\mathrm{in}} \in \{10^{-6}, 10^{-3}, 1\}\mathrm{mW}$, respectively. The resulting electric field norms are plotted in figure 4.10 in a semi logarithmic representation to visualize the data points over several orders of magnitude. The data points are fitted to a linear function without offset by means of a least square fit, which yields a proportionality factor of $E = 60.9 \cdot U_{\mathrm{res,\,p}}$ for the electric field at the trap position mentioned above.

The proportionality relation will be used in the next section to calculate the coupling strength at the trap position over several orders of magnitude input power.

4.2.4 Calculation of the expected coupling strength

Having calculated the electric field strength at the trap position, the coupling strength can finally be estimated.

The last missing step for the calculation of the coupling strength is the electric dipole moment d, required by equation (4.1). It is calculated using the Alkali Rydberg Calculator

(arc) python package [74] for both $nS_{1/2} \rightarrow nP_{3/2}$ transitions with $n = 68$ and $n = 85$.

Eventually, the calculated coupling strengths are shown in figure 4.11 for input powers ranging over six orders of magnitude.

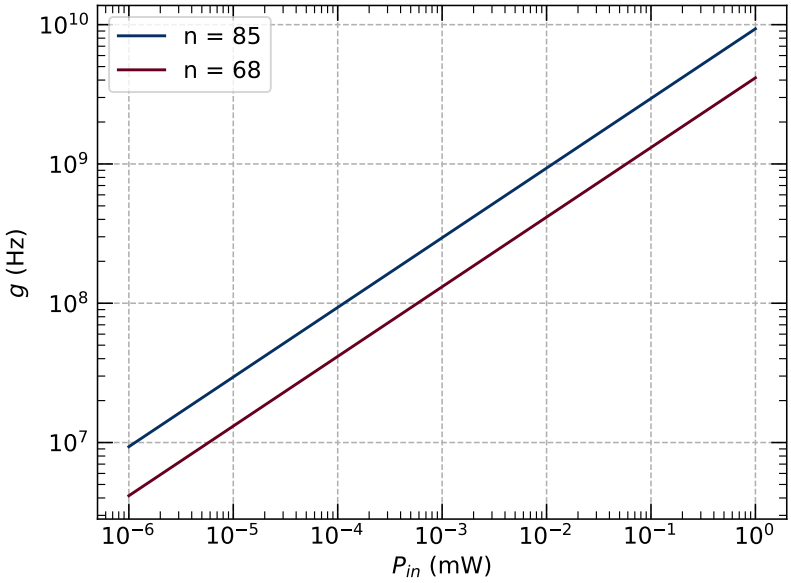

Figure 4.11: Simulated coupling strength g for the two target Rydberg state transitions with $n = 85$ and $n = 68$ for input powers P_{in} over a range of six orders of magnitude in logarithmic representation.

Even for very small input powers like $P_{\text{in}} = 1 \cdot 10^{-6}$ mW, which corresponds to -60 dBm, coupling strengths in the order of magnitude 10 MHz can be expected. To achieve weaker coupling for experimental measurements, the trap position can be moved to further away from the waveguide and the microwave power can be weakened.

As a final note, the presented coupling strengths have been calculated by using the scalar electric field norms obtained from the Comsol simulation described above. This neglects the influence of the microwave polarization on the coupling strength. Depending on the needed polarization for the driven transition, the polarization can change the resulting coupling strength by a factor which ranges between 0 and 1. For example, consider the case of a trap that is centred directly above the waveguide and a quantization axis parallel to the chip surface, which is given by the magnetic field direction inside the Z wire trap. For this configuration, the electric field is perpendicular to the quantization axis. Thus, the microwave polarization can be described by a superposition of σ^+ and σ^- microwaves, which results in a factor of 1/2 of the presented coupling strength for either transition.

4.3 Fabrication of the coplanar waveguide resonator atom chip

The previous section has shown that the designed chip layout facilitates the wanted coupling, so subsequently the chip has to be fabricated. This is done by means of a lithography process. The fabrication is based on the description given in the supplementary material of reference [60] and follows to the steps given there exactly, if not stated otherwise. As part of a collaboration, the fabrication is performed by the staff of the cleanroom located at the Forschungszentrum Jülich, based on the lithography masks that are developed in this thesis. That is why the following section aims at explaining only the most relevant aspects of the fabrication, that are needed to plan the fabrication process.

First, the chip materials have to be chosen. An overview of all needed materials is shown schematically in figure 4.12, which shows the chip in cross-sectional view. The dielectric substrate serves as the carrier material of the chip and is required to have good thermal conductivity. For the Z wire and coplanar waveguide a superconducting material is needed. Finally, normal conducting material in between the Z wire and the coplanar waveguide is also needed to shield the Rydberg atoms from the bare dielectric substrate, as described in section 4.1.

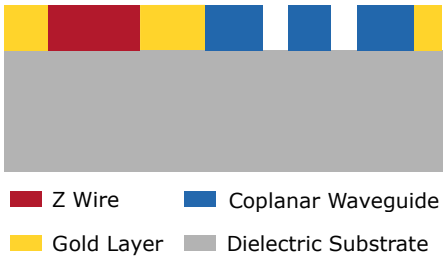

Figure 4.12: Overview over the involved chip materials, that shows the atom chip in a schematic side view with all relevant structures labelled by colour.

Sapphire is chosen for the dielectric substrate. Sapphire possesses very good thermal conductivity [75], which is important to enable proper cooling of the superconducting layers on top of the substrate. On the one hand, this layer has to get cold enough to become superconducting, on the other hand the temperature dependence of the resonance frequency is only negligible for temperatures well below the critical temperature, as explained in section 3.2.3. Furthermore, sapphire has shown to be a good choice for high quality factor high overtone bulk acoustic resonators [76] and has already been used in hybrid quantum mechanical experiments with electromechanical systems [28] and

coplanar waveguide resonators [60]. Although the chip generation at hand does not need a high quality factor resonator as shown in section 4.2, future generation atom chips that incorporate an electromechanical oscillator aim at high quality factors. Given that the chip at hand serves as an intermediate testing chip it makes sense to use a substrate which is of relevance for future generation chips, e.g. when considering the process of chip attachment (see section 6.1.1).

Niobium will serve as the material for the superconducting structures on the chip surface. As a superconductor with a critical temperature of $T_c = 9.2\,\mathrm{K}$ [69], superconductivity of niobium can be achieved in the planned cryogenic environment of at least 4.2 K and is further often used for superconducting chips of different kinds [39, 59, 60].

Finally, the normal conducting part of the chip surface will be made of gold. Depositing gold on top of sapphire requires a thin adhesion layer in between, which will be made of Titanium.

Based on the experiences with the chip fabricated for reference [60], comparable layer thicknesses as described there will be used. That is a layer thickness of 500 nm for niobium. Additionally, a 300 nm gold layer with a 4 nm titanium layer beneath, that serves as adhesion layer. Under all material layer thicknesses, the niobium layer thickness is of particular interest as it influences the treatment of kinetic inductance and consequently possible resonance frequency shifts of the coplanar waveguide resonator. See section 3.2.3 for the discussion of kinetic inductance. Since no temperature-tunable resonator is currently intended and the resonator is supposed below temperatures of $T_c/2$, a larger layer thickness is reasonable since also the kinetic inductance scales inversely with the cross-sectional area of the film [77].

Furthermore, a larger cross-sectional area is advantageous for the current that can be carried by the magnetic trapping wire before reaching its critical current density.

Finally, with the materials being set, the complete fabrication process is shown in figure 4.13. Here, the chip is shown in a cross-sectional view and the shape of the structures are the same as illustrated in figure 4.12. The initial fabrication step comprises the deposition of the 500 nm niobium layer on a four-inch c-plane sapphire wafer. After that, the wafer is diced into the final sample sizes of 11x11 mm^2. Subsequently, resist has to be deployed on the sample in order to form the structures on the chip surface in the first lithography step. For that, an even layer of resist is applied on the complete sample surface by means of spin coating. Afterwards, the areas defined by the lithography mask are exposed to a light source, in the case of optical lithography (synonymously photolithography). The effect of exposing a resist to a light source depends on the specific type of resist in question, as it is necessary differentiate between positive and negative resits. In the case of negative resists, areas that are exposed to the light source undergo crosslinking, which is followed by a subsequent baking process. The result is that the resist in these areas remains on the sample after development.

The photolithography masks for the designated structures require a high level of reproducibility and precision, in particular for the small structures of the finger coupling

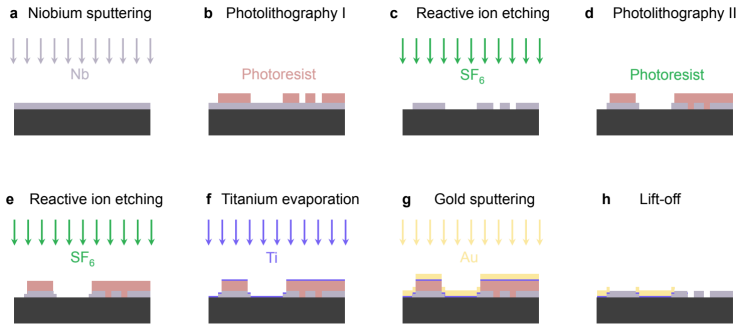

Figure 4.13: Complete process of the chip fabrication in a cross-sectional view, including material deposition, lithography steps and etching. Image taken from the supplementary material of reference [60]. **a-c** After the deposition of niobium onto the surface, which is the superconducting material for both the magnetic wire trap and the coplanar waveguide resonator, these two latter structures are formed during the first lithography and subsequent etching step. **d-f** The following steps lead to the formation of steps in the outer edges of all on-chip structures, which serve the purpose of reducing the step size between substrate and niobium and subsequently lead to a better contacting between niobium and gold. **g-h** Finally, the remaining resist is removed together with the gold on top in a lift-off process.

capacitors. Therefore, the masks were scripted, based on the python package gdspy[2]. This package provides the ability to create files in a gds format, which is used for the creation of lithography masks and can also be opened in 2D CAD programs. For the general case of drawing coplanar waveguides, the code base of the transmission-line gitHub repository[3] was used. The transmission-line code provides a straightforward implementation to draw meandering coplanar waveguide structures and calculates the length of the resulting coplanar waveguide structure automatically, which is important for designing the resonator length on the chip surface. The core functionalities of the transmission-line package were augmented by the possibility to automate the drawing of finger coupling capacitors in the scope of this thesis.

The masks for the first and second lithography steps are both shown in figure 4.14, referring to the steps Photolithography I and II in figure 4.13. Both steps are written with a negative resist. The first step serves the purpose of keeping niobium on the sample surface at the positions defined by the first mask, while the rest of the niobium is removed in a reactive ion etching step. The second lithography mask, corresponding to step Photolithography II in figure 4.13, covers most parts of the first mask except for a small distance of 10 µm that is maintained towards the edges. This leads to a

[2]See the website https://gdspy.readthedocs.io/en/stable/ (visited on 07/23/24)
[3]See the repository under https://github.com/danielflanigan/transmission-line (visited on 07/08/24)

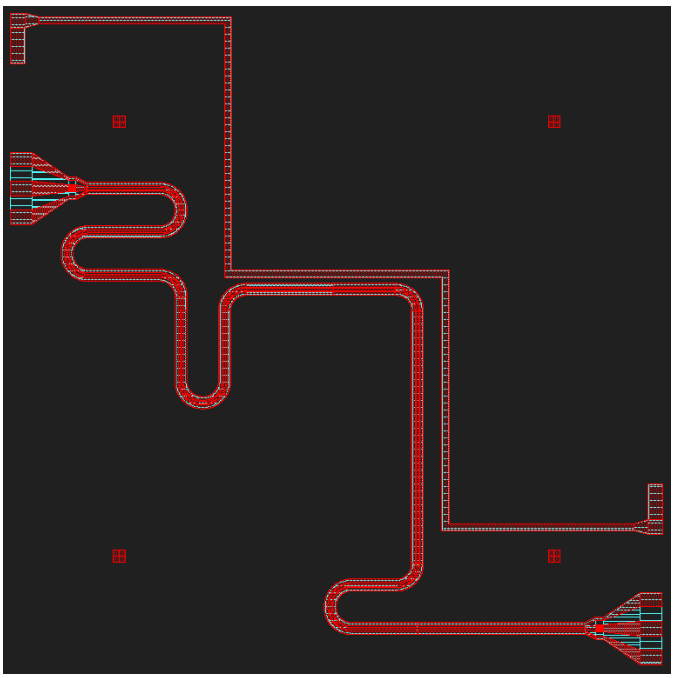

Figure 4.14: Lithography masks for the first and second lithography step drawn in different colours. The mask for the first lithography step is shown in red, the second step mask is drawn in blue. The mask for the first step contains four alignment markers, represented by the four times four squares. The structures of the second lithography mask cover the complete coplanar waveguide and Z wire except for a 10 µm edge at the sides, see text for further information.

reduced niobium step size after the subsequent reactive ion etching process and therefore to better contacting between gold and niobium after the final gold deposition. To align both lithography steps, alignment markers have to be placed in the first lithography step, which can be seen as the four times four square structures depicted in figure 4.14. The final fabrication step is the lift-off process. Here, the remaining resist is removed together with the gold that has been deposited on top of it, thus completing the final chip.

In the beginning of the fabrication process, the complete chip was fabricated by using photolithography only. However, the precision of this optical process was not good enough for the structures of the finger coupling capacitors, this is shown in the microscope image of figure 4.15(a). Compared to the drawn lithography mask, the ends of the fingers are rounded and the finger width varies over the length of the fingers and between different fingers. This would lead to a shift in the coupling capacitance with the possible effects discussed in section 3.1.2, which are a drift in the resonance frequency and bandwidth of the resonator. Next to that, the resonator would most likely become coupled in an asymmetric way. Therefore, the fabrication part of the finger capacitors was changed to

be done in an electron-beam lithography step which allows for larger precision, thereby preventing an avoidable source of frequency shift. A coupling capacitor which was fabricated in an electron-beam lithography step is shown in figure 4.15(b). In contrast to the one in figure 4.15(a), the structures show the drawn shape precisely.

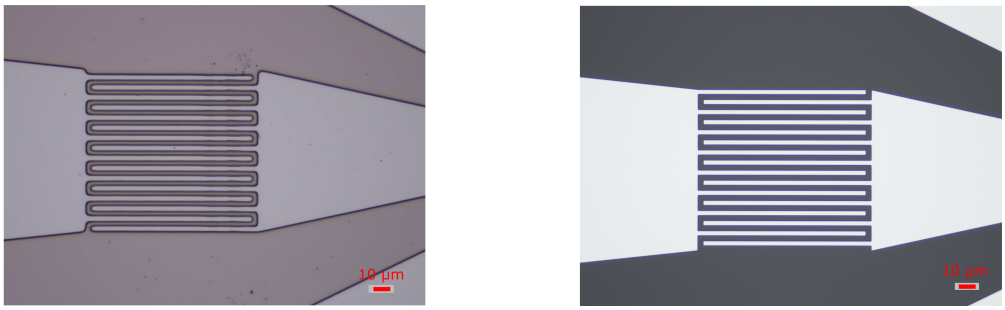

(a) **(b)**

Figure 4.15: Microscope photographs of the coupling capacitor. (a) shows a capacitor that was fabricated by means of optical lithography. The finger edges are rounded and the finger width varies slightly over the length of the fingers. In contrast, (b) shows a capacitor as a result of an electron-beam lithography fabrication with a precise shape. Both images courtesy of Joscha Domnick, FZ Jülich.

Eventually, figure 4.16 shows microscope photographs of the latest stage of chip fabrication at the time of writing this thesis. The shown chip parts already include the deposited gold layer and allows recognizing some parts that were described in the preceding structure. The coplanar waveguide bond pads are shown in figure 4.16(a) with clearly distinguishable materials, i.e. the evident gold layer next to the grayish niobium structures. The in principle transparent sapphire appears dark due to the surface where the chip is placed on. All of these three materials can be recognized in the close-up of a meandering waveguide part in figure 4.16(b). The interaction region is shown in figure 4.16(c), which illustrates the discussed lateral distance between the central bar of the Z wire structure, represented by the gray rectangular niobium line in the centre of the image, and the coplanar waveguide resonator approaching the bar from the bottom. In all three images figure 4.16(a) to figure 4.16(c), the 10 µm gold overlap region can be recognized, where the niobium step size has been reduced. It becomes evident as a prominent darker gold strip at the structures edges of the Z wire and the outer edges of the coplanar waveguide.

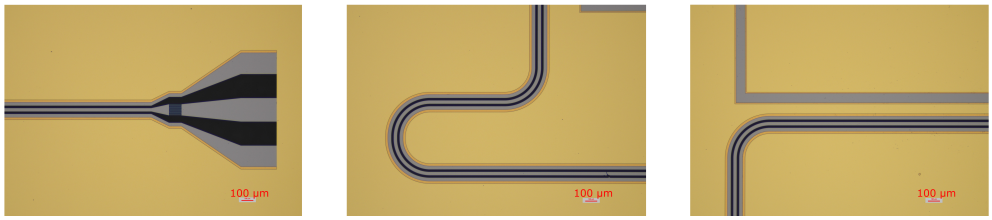

(a) **(b)** **(c)**

Figure 4.16: Microscope photographs of different on-chip parts with the final gold layer applied. Gray structures are made of niobium and the dark parts in between correspond to the sapphire substrate of the chip. In (a), coplanar waveguide bonding pads are shown. Also, part of the 1 mm clearance becomes apparent, where the gold layer continues on the right side. In (b), a detail of the meandering waveguide is shown. In (c), the interaction region is shown, where the waveguide reaches half of its length and is close to the Z wire. All images courtesy of Joscha Domnick, FZ Jülich.

Chapter 5

Electromechanical resonator

While the coplanar waveguide of chapter 3 serves as the microwave resonator, future atom chips aim at implementing an electromechanical oscillator as microwave resonator.

Electromechanical resonators are a common technique in the field of electronics and communications technologies, e.g. used as frequency filters [78]. These resonators are based on an electromechanical coupling mechanism, that owes to the use of piezoelectric materials. Piezoelectricity leads to a coupling and conversion between electrical and mechanical energy by the direct and indirect piezoelectric effect [78]. This effect can be exploited to create acoustic waves in a piezoelectric material by applying an oscillating electric field or vice versa [78]. One typical example for electromechanical resonators used in modern technology is a bulk-acoustic wave (BAW) resonator, which consists of a piezoelectric material with two thin electrodes attached to the top and bottom surfaces [78].

High quality factors of electromechanical resonators can be obtained by depositing small layers of piezoelectric material on top of a substrate with high acoustic quality, e.g. sapphire or silicon, which results in the resonator type of high-overtone bulk acoustic resonators (HBAR) [79]. If the piezoelectric layer is exposed to an electric field, it will not only generate an acoustic wave inside this layer, but in the whole resonator. This leads to a distribution of the acoustic energy between the piezoelectric layer and the high-quality acoustic substrate, which has two major consequences. On the one hand, this leads to the acoustic properties of the substrate being the main influencing factor for the quality factor [79] and on the other hand leads to a reduced electromechanical coupling because the acoustic energy in the piezoelectric layer is reduced [79].

For the intended use of the HBAR, the latter point is of great interest. In the planned experiment, the electric field generated by the piezoelectric layer due to the mechanical motion of the HBAR is supposed to couple to a microwave transition of Rydberg atoms close to the HBAR's surface. In principle, this setup requires both, namely a high quality factor for large resonator lifetimes and a large generated electric field for a sufficient coupling strength between the resonator and the atoms. However, the mentioned energy distribution in the HBAR makes clear that the design of such a resonator will be a compromise between both properties.

To determine, which electric fields need to be generated in order to achieve sufficient coupling strengths, and which design consequences have to be drawn form that result

corresponding device simulation need to be conducted. Due to the complexity of the physical models of these resonators, typically Finite element method (FEM) software are used to simulate the device behaviours [73, 78, 80]. This chapter will give an introduction of first calculations that were made towards that direction during this thesis.

The first section will introduce a FEM simulation for the coupling strength of a piezoelectric layer serving as a BAW resonator. The obtained coupling strengths are compared to the results of a simplified theoretical model for a proposed hybrid quantum system between such a resonator and ^{87}Rb Rydberg atoms of reference [20].

The final section of this chapter provides a brief and preliminary introduction to the simulation of HBAR's.

5.1 Coupling strength for an electromechanical resonator

The coupling strength between a mechanical oscillator and a Rydberg atom has been theoretically described by Gao *et al.* in Ref. [20]. In this case, the electromechanical oscillator consists of one piezoelectric layer, only. For their estimation, the authors calculate the electric field at a distance L above a circular oscillator with radius R, see figure 5.1 for the setup. This is done by calculating the expected surface charge for the piezoelectric material that is displaced with l_0, the zero-point fluctuation of the dilatational mode of the oscillator. Using this surface charge, the electric field created by two charged surfaces at a distance b, the resonator thickness, is readily obtained. Subsequently, the electric field can be used calculate the coupling strength using equation (4.1), they use the atomic transition $79P_{1/2} \rightarrow 80S_{1/2}$ of ^{87}Rb with transition frequency $\omega_a \approx 2\pi \times 8\,\mathrm{GHz}$. They plot the electric field as a function of L and R, which allows them to find the best distance L for any radius R, or vice versa. As a first step towards the design and evaluation of sophisticated electromechanical oscillator models, the following part is dedicated to the reproduction of such a plot using FEM software. Reproduction of such a plot is done to get a first impression of the capabilities of such a simulation by comparison with a simplified theoretical model.

The FEM software of choice is Comsol Multiphysics [72], using the Piezoelectric Effect module. That is a multiphysics module, which combines the Solid Mechanics and Electrostatics modules to account for the electric-mechanical coupling of piezoelectric material. The model is built like the theory model schematic and is shown in figure 5.2. A piezoelectric cylinder, made of Aluminium Nitride (AlN) with height $b = 0.5\,\mu\mathrm{m}$ and radius $R = 3.4\,\mu\mathrm{m}$ is sandwiched between two Aluminium electrodes. The height of the piezoelectric cylinder arises from the fact that the piezoelectric layer is supposed to have an eigenfrequency which matches the atomic transition frequency. With the mechanical eigenfrequency given by $\omega_m = 2\pi\nu/2b$ [20], where ν denotes the speed of sound in the material, $\omega_a \approx \omega_w$ is fulfilled by the chosen cylinder height [20]. The chosen cylinder radius ensures the largest possible electric field at the distance $L = 5\,\mu\mathrm{m}$, where the

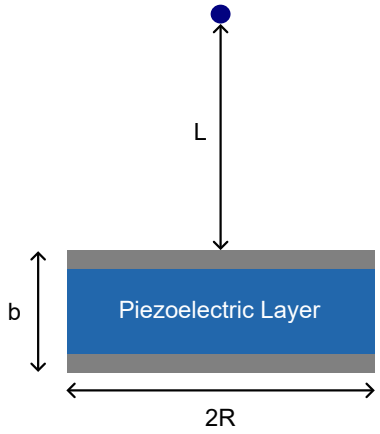

Figure 5.1: Piezoelectric layer sandwiched between two electrodes that serves as a resonator with radius R and thickness b. The electric field created by the resonator couples to the atom in a distance L above the resonator. Figure adapted from [20].

atoms are assumed to sit, and consequently the electric field will be evaluated. These three components form the resonator, that is surrounded by a sphere of perfect vacuum, partially removed in figure 5.2

To generate an electric field, the piezoelectric material has to be deformed. Gao *et al.* calculate the electric field generated by the zero-point fluctuation of the resonator $l_0 \approx 2.2 \cdot 10^{-16}\,\mathrm{m}$. In the simulation, this deformation achieved by putting a fixed constraint boundary condition on the bottom boundary of the piezoelectric cylinder (see blue coloured boundary in figure 5.2) and displacing the top boundary of the cylinder by a displacement given by l_0. The fixed constraint boundary condition ensures that this boundary is fixed in place and that the displacement actually leads to a deformation of the piezoelectric cylinder. Finally, the created static electric field is probed in the distance $L = 5\,\mu\mathrm{m}$ above the centre of the resonator.

The simulation result and the result based on the estimation presented above differ by about one order of magnitude. The estimation results in an electric field of $E_{z,\mathrm{est}} = 1.8\,\mathrm{V\,m^{-1}}$, corresponding to a coupling strength of $g \approx 50\,\mathrm{MHz}$ [20], while the simulation yields a result of $E_{z,\mathrm{sim}} = 0.14\,\mathrm{V\,m^{-1}}$, corresponding to $g \approx 4\,\mathrm{MHz}$. The difference of these results was investigated by further simulations and can likely be traced back to two different causes. The estimation result is yielded by the simulation, too, if

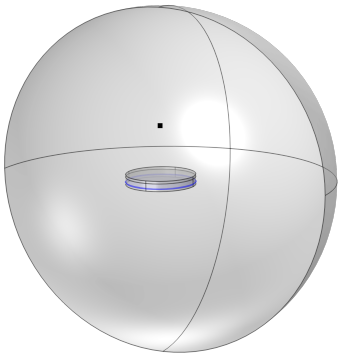

Figure 5.2: Setup to simulate the electric field generated by the electromechanical resonator. The resonator is shown in the centre, with a piezoelectric cylinder surrounded by two electrodes (see text), surrounded by a sphere of perfect vacuum (partially removed here). The black dot indicates the position, where the electric field will be probed, and the blue coloured area is the bottom boundary of the piezoelectric cylinder.

the displacement is taken to be twice the zero-point fluctuation l_0 of the piezoelectric cylinder, that was derived in reference [20], and if the dielectric constant of Aluminium Nitride is neglected. The latter is indeed only considered partially in the derivation of reference [20]. To calculate the electric field above the top electrode, they subtract the electric field created by a surface charge of the bottom electrode from the electric field created by the surface charge on the top electrode, thereby neglecting that the dielectric in between both electrodes alters the electric field of the bottom electrode. The l_0 confusion may be traced back to an inconsistency in the derivation.

The coupling strength resulting from the FEM simulations and calculated for the above-mentioned transition is shown in figure 5.3 for larger radii and atom distances than shown in reference [20]. The plot allows to find the best matching pairs of R and L like intended above and shows that coupling strengths in the order of 1 MHz are feasible in a distance of order 10 µm, even for the simulated zero-point fluctuation.

Summarizing, the simulation can be compared to the basic estimations for the coupling strength and demonstrates reasonable coupling strengths even for zero-point fluctuations. Furthermore, it paves the way for additional simulations that incorporate higher modes, which will be subject of the next section.

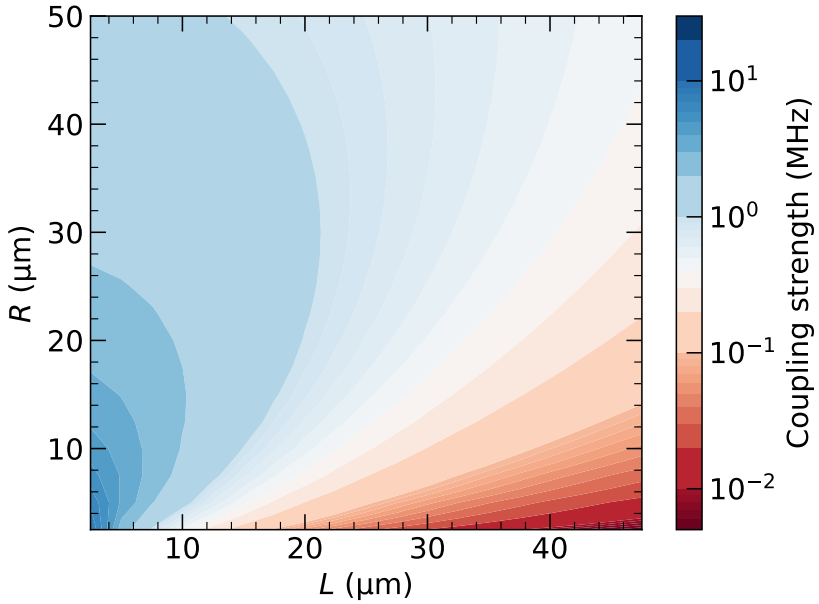

Figure 5.3: Coupling strength for interaction between an electromechanical resonator with zero-point fluctuation displacement and ^{87}Rb Rydberg atoms for a $79P_{1/2} \rightarrow 80S_{1/2}$ transition as a function of the resonator radius R and the distance L between resonator surface and atoms.

5.2 Towards the simulation of high-overtone bulk acoustic resonators

As mentioned in the introduction, it is intended to use a high-overtone bulk acoustic resonator (HBAR) for later electromechanical oscillators.

As described above, the high quality factor of these devices comes with a reduced generated electric field. In the previous section, the complete energy was assumed to be distributed equally in the piezoelectric layer. However, not only is this assumption simplified since the modes may lead to different deformation amplitudes over the piezoelectric volume [79], but due to the mentioned energy distribution the model is also not transferable to HBAR simulations.

In order to design such resonators, a simulation of the high-overtone modes of such a resonator will be needed prospectively for the estimation of the resonator's quality factor and the resonator - atom coupling strength. Other experiment with HBARs have made use of substrate heights of 400 µm [28]. Simulating such substrate thicknesses with a sufficient meshing to capture all relevant physical properties can lead to a computationally

challenging problem and need sophisticated meshing procedures [73]. For quantitative results such a meshing procedure would have to be implemented. In the scope of this thesis, this section describes first qualitative eigenfrequency simulations of high-overtone modes in a cylindrical substrate using the Comsol eigenfrequency analysis.

The simulations are simplified by exploiting a mirror symmetry of the cylindrical resonators, which allows to perform the simulation on a split model, see figure 5.5. Here, the bulk substrate is modelled as anisotropic, single-crystal silicon, while the piezoelectric layer is modelled as Aluminium Nitride. The substrate has a height of 30 µm and the piezoelectric layer is 5 µm thick. The complete cylinder is surrounded by a perfectly matched layer, which is supposed to prevent unphysical reflections and reduce the number of unphysical modes [78]. The outer border of the perfectly matched layer is used for the fixed boundary condition.

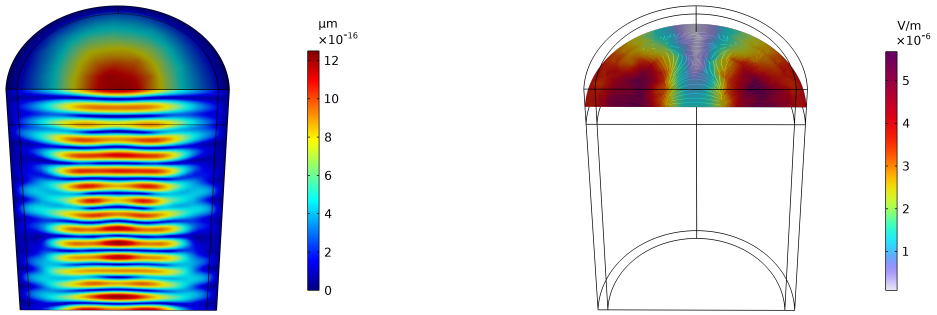

(a) **(b)**

Figure 5.4: Mode shape and corresponding electric field of a physical high-overtone mode of a bulk acoustic resonator as result of an eigenfrequency simulation. The mode shape is shown in (a), illustrated by the three-dimensional surface displacement in µm, as indicated by the colour legend. The corresponding electric field norm in units of V/m inside the piezoelectric layer is shown in (b). The electric field is the result of deformations of the piezoelectric layer due to the found eigenmode in the eigenfrequency simulation. Since the amplitude in this simulation is not normalized, but arbitrary, the resulting electric field amplitude is arbitrary, too.

In figure 5.4 a high-overtone eigenmode with its corresponding created electric field inside the piezoelectric layer is shown, resulting from an eigenfrequency simulation. The mode shape figure 5.4(a) is illustrated by its surface displacement. Although the plot contains a colour bar, which indicates the displacement in units of µm the amplitude resulting from the eigenfrequency simulation is arbitrary and would have to be normalized in order to give quantitative results. Hence, the same applies for the electric field in figure 5.4(b), where a quantitative result is of particular interest for the estimation of coupling strengths.

Even though it is of qualitative nature, the eigenfrequency simulation demonstrates that

it can find physical eigenmodes of the bulk acoustic resonator. Two further high-overtone modes are shown in figure 5.5.

Summarizing, the simulation of high-overtone modes is possible, but requires some parameter fine-tuning. For quantitative results, the displacement amplitude needs to be normalized to the phonon number in the corresponding oscillation mode in order to allow conclusions for the simulated electric field created above the resonator.

(a) **(b)**

Figure 5.5: Possible eigenmodes of a cylindrical bulk acoustic resonator consisting of a high-quality acoustic substrate with a piezoelectric layer on top, as a result of an eigenfrequency study in Comsol. (a) to (b) show the three-dimensional surface displacement of the resonator for different modes.

Chapter 6

Integration into the experimental setup

Once the atom chip has been fabricated, appropriate hardware is needed to integrate it into the experimental setup. The following part is dedicated to the description of the constructed hardware. Initially, the requirements are described briefly and after that all needed parts will be discussed to be finally put altogether.

The experimental environment places certain demands that must be taken into account. This concerns the cryogenic environment of 4.2 K temperature and ultra-high vacuum (UHV) conditions with a pressure of $p < 10^{-10}$ mbar.

For the cryogenic environment, one aspect to keep in mind is the different thermal contraction among the used materials. This plays a role, e.g. for connections in cryogenic environments like bolted connections, and possible breaking of materials with different contraction coefficients. Additionally, the thermal conductivity of the used components plays an important role. The atom chip will be attached to a sample holder, which is supposed to cool it down, but in order to do that efficiently the thermal conductivity of the involved parts has to be large enough. Otherwise, the heat input of remaining black body radiation and cables cannot be compensated for sufficiently [81]. A typical material used in cryogenic environments is copper, due to its advantageous thermal conductivity properties [75]. However, while the thermal conductivity at room temperature is equal to comparable for standard coppers, it differs significantly at cryogenic temperature for different purity-grade coppers [75]. The highest purity grade is so-called "five nines" copper with a purity of 99.999 %. At the cryogenic temperature of 4.2 K, it has a thermal conductivity of 11 300 $\mathrm{W\,m^{-1}\,K^{-1}}$. [75]. Followed by that are the normed copper grades C10100 and C10200 with thermal conductivities at 4.2 K of 850 $\mathrm{W\,m^{-1}\,K^{-1}}$ and 560 $\mathrm{W\,m^{-1}\,K^{-1}}$, respectively [75]. The common choice for sample holders and other cryogenic components is one of the two latter coppers, due to availability and cost aspects [75]. If not stated otherwise, all copper parts described in this chapter will be made of C10200 copper.

Besides that, the ultra-high vacuum environment demands a certain choice of material as well. All used components need to have a very low outgassing rate. Although the outgassing might as well be less relevant in a cryogenic environment due to freezing, UHV compatible material were considered during the design process. Furthermore, when engineering parts for an UHV environment, the creation of virtual leaks has to be prevented. These are trapped air pockets, that are kept from being pumped due to

building constraints, e.g. air pockets between the bottom of drill holes and the screw inside. This can be avoided by planning cross holes that vent the air pockets of bolted connections or by using vented screws if cross holes are no option.

6.1 Sample holder

The central part of the experimental integration is the sample holder, which is made of copper. It serves as a platform for the chip and integrates all chip-related components, e.g. the printed circuit boards for electrical contacting. It is attached to the cryostat sample holder and allows electrodes to be mounted above the chip.

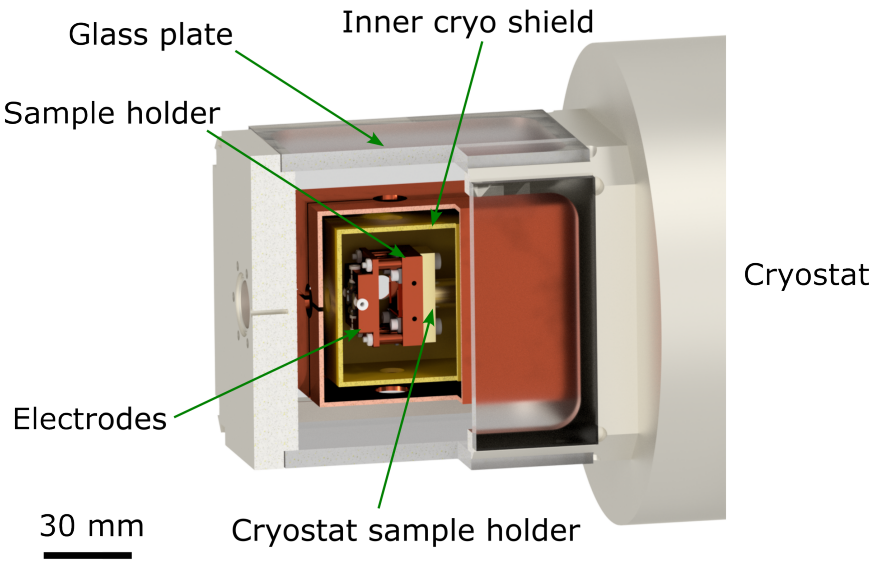

Figure 6.1: CAD drawing of the cryogenic region. The complete designed sample holder is shown in between the cryo shields. This includes the sample holder for the chip, which is bolted to the cryostat sample holder inside the inner cryo shield. The latter is further surrounded by an outer cryo shield. The labelled electrodes will be introduced later on. All components are surrounded by a vacuum chamber with glass plates that ensure optical access. The cryostat label indicates the position of the cryostat relative to the shown setup.

The design has to take spatial constraints placed by the surrounding inner cryo shield into account. The cryo shields are metal plates that are thermally anchored to a certain temperature stage of the cryostat and serve the purpose of shielding the experimental region from black body radiation. The complete cryogenic setup is shown in figure 6.1.

With dimensions of 20x30 mm^2, 10 mm remain between each short side of the sample holder and the inner cryo shield, and 5 mm between each long side of the sample holder and the inner cryo shield.

The final sample holder design is shown in figure 6.2. The CAD drawing in figure 6.2(a) shows schematically attached PCBs and figure 6.2(b) shows a photograph of the fabricated sample holder with a test chip. The most prominent structure of the sample holder is the central chip platform. The platform has a shallow deepening, where the 11x11 mm^2 chip is placed and attached to the platform (see section 6.1.1). The four outer holes serve as through-hole connections for the electrode mount, see section 6.3.1. The four holes close to the chip platform serve the connection of the flexible PCBs, see section 6.2. Finally, the sample holder will be connected to the cryostat sample holder with two M3 screws from the back.

(a) **(b)**

Figure 6.2: Images of the designed sample holder. (a) shows a CAD drawing of the sample holder, that is attached to the sample holder of the cryostat. On its top side, left and right of the centre chip platform, flexible printed circuit boards will be attached, which is schematically shown here. In (b), photograph of the built sample holder is shown. It also includes an early-stage fabrication test chip that is placed on the chip platform, where it will be attached to permanently later on.

6.1.1 Towards chip attachment

The atom chip will be attached permanently to the sample holder. The attachment method has to be compatible with both the ultra-high vacuum and the cryogenic environment, plus it has to provide high thermal conductivity. In addition, it needs to allow attaching sapphire to copper.

In other experiments, atom chips have been glued to sample holders using epoxy glue, but this did not lead to a sufficient cooling of the chip due to limited thermal conductivity of the used epoxy [81]. Nevertheless, glueing with epoxy was tested and the attachment itself works as expected. The used epoxy is Stycast 2850 FT, with a thermal conductivity in the order of 0.05 W m^{-1} K^{-1} [82], which is several orders of magnitude worse than the thermal conductivity of copper mentioned in the introduction to this chapter.

A well-suited material used for cryogenic soldering is pure Indium or Indium alloys, which is in particular stressed to be capable of joining different materials and surviving thermal cycling [83]. However, pure Indium (purity $> 99.999\,95\,\%$) has advantageous properties regarding its wetting behaviour even without flux [83]. Since wetting of sapphire is quite demanding, pure Indium should be preferred. Soldering with pure Indium was tested in a procedure of placing a 100 µm thick Indium foil in the deepening of the chip platform and placing a test chip with sapphire substrate on top of it. Subsequently, the copper mount was put in a vacuum environment with the possibility to preheat it above the melting temperature of Indium (157 °C [83]). The chip had some weight put on top of it to be slightly pressed onto the chip platform. However, this process has not yet been successful, because the indium was not able to wet the sapphire.

As a consequence, it will have to be tested whether a thin gold layer of 10 nm on the bottom of the sapphire substrate can lead to successful indium soldering, or if another attachment method has to be chosen.

6.2 Electrical connection for the atom chip

Section 4.1 already introduced the bond pads on the chip, that enable electrical connections to the trapping wire and the coplanar waveguide. The printed circuit boards (PCBs) that serve the power supply have been schematically shown in figure 6.2(a) in the previous section. The PCBs are designed to be flexible and long enough to be bent around the small side of the sample holder such that they can be connected to cryogenic-compatible cables on the bottom side of the sample holder (see figure 6.1 for the surrounding setup). Furthermore, they are attached slightly off-centre on the sample holder which provide the shortest connection possible between on-chip and PCB bond pads.

The PCB design is shown in figure 6.3. The dielectric substrate is a 100 µm thick UHV compatible polyimide layer. At the beginning and end of the PCB, the polyimide is reinforced to 1 mm thickness with an FR4 layer[1]. The reinforcement allows greater mechanical stability. This is necessary at the end where the PCB will be connected to the cables and on the other side, where it will be screwed to the sample holder (see screw holes next to 'PCB Bond Pads' in figure 6.3) via M2 screws. Furthermore, the reinforcement is chosen such that the PCB and the chip surface will be on the same level to simplify the wire bonding process.

The PCB has a thicker direct current line, which will be connected to a wire via a screw and cable shoe connection and an impedance controlled 50 Ω coplanar waveguide[2],

[1] Panasonic FR4 Epoxy Laminate, outgassing test result provided by manufacturer. 24 hours at 125 °C under pressure $< 1 \cdot 10^{-5}$ mbar with results: Total Mass Loss (+125 °C) = 0.27 %, Recovered Mass Loss 24 hours (+125 °C) = 0.14 % and Collected Volatile Condensable Material (+25 °C) = 0.00 %, values compliant with the European Cooperation for Space Standardization Q-ST-70-02.

[2] To avoid undesirable signal reflections.

Figure 6.3: Layout of one flexible PCB for powering the atom chip. It contains one direct current line (top structure) to feed the on-chip trapping wire and a coplanar waveguide (bottom structure) for the connection to the on-chip coplanar waveguide resonator. Both lines will be connected to cables in the connector region and to the chip via the PCB bond pads. In the connector region of the PCB, the SMP footprint for soldering the SMP connector to the PCB can be seen in the bottom.

which will be powered via a surface mounted SMP connector[3]. The footprints for the cable-PCB connections are depicted in figure 6.3.

The PCB design is individual per chip layout side as a consequence of the different arrangement of the on-chip bond pads of the coplanar waveguide and the Z wire bond pads. The PCB layout shown in figure 6.3 matches the left side of the chip layout in figure 4.2. Matching PCB and on-chip bond pads is achieved by using mirrored PCBs for the left and right side of the chip.

6.3 Rydberg ionization and ion detection

Some of the most important properties of Rydberg atoms were introduced in section 4.2.1 with strong sensitivity to electric fields among them. Any stray electric field gradients can lead to undesirable Stark shift mediated disturbances of the Rydberg transitions. Therefore, a set of electrodes for the compensation of stray electric fields along all coordinate axes is desirable, also referred to as electric field control.

In the experiment, transitions between neighbouring Rydberg states are driven by microwave fields. As outlined above, one transition of interest in this experiment will be the $85S_{1/2} \rightarrow 85P_{3/2}$ transition. The interaction with the microwave resonator will drive Rabi oscillations of the transition, which are to be detected. A direct readout of the coplanar waveguide resonator is not precise enough to distinguish single excitation changes. Additionally, the future electromechanical resonator will not be read out directly due to the reduction of its quality factor if it is coupled to a readout line.

That is why the readout will be done via the Rydberg atoms. For that, the property of Rydberg atoms to be ionized by easily achievable electric field strengths [32, 84] is

[3]SMP-MSSB-PCS-NM, SMP connector with all metal parts made of CuBe for UHV compatibility.

used in the experiment. The Rydberg atoms are ionized and subsequently accelerated towards an ion detection setup, see e.g. reference [85].

To distinguish between different Rydberg states, the different ionization energy of the different states can be exploited for a state selective field ionization, e.g. applied in reference [40]. Or else, an experimental sequence including a combination of laser pulses and field excitation can be implemented. This could include a selective deexcitation of the $85S_{1/2}$ state by shining in the probe and control laser again and subsequent field ionization. Accordingly, there would only be an ion if the Rydberg atoms were in the $85P_{3/2}$ state, hence showing Rabi oscillations in the ion signal.

This section aims at describing the designed ion detection setup and to show its ability to accelerate the ionized Rydberg atoms out of the experimental region, in order to detect them with the help of a microchannel plate detector (MCP[4]), which allows detecting ions with the working principle of an electron-multiplier.

6.3.1 Sample holder mounted electrodes

Figure 6.1 already gave an overview of the available space for integrating the chip and everything related into the experimental setup. With the design of the sample holder being set in section 6.1, this section is dedicated to the construction of electrodes that are compatible with the sample holder design, meet the requirements mentioned in the introduction and fits into the available space.

To facilitate the compensation of electric field gradients along all coordinate axes several individually controllable electrodes are needed, which sets the first design requirement. Furthermore, the electrodes should be centred above the region of the trapped atoms for ionization and subsequent acceleration, which will be discussed in the following sections.

The final design that was developed is shown in figure 6.4. The design incorporates four electrodes, which are centred above the chip with the help of an electrode holder plate construction. Mounting the electrode holder plate is done by four polls that serve as feet. Since the holder plate has the same size as the sample holder, the position of the polls can be moved to the most outer edges, which leaves enough space for the PCBs on the sample holder (cf. section 6.1).

The holder plate and the feet are made of copper. This has several advantages. On the one hand, the good thermal conductivity of copper should lead to sufficient cooling of the holder plate as well, thereby reducing a source of remaining black body radiation in the vicinity of the atoms. Furthermore, the holder plate and the polls will be electrically grounded, due to the contact with the grounded sample holder. The electrodes will be individually connected to high voltage cables, which will come from the direction of the sample holder. Having conducting and grounded polls leads to shielding of the Rydberg atoms from the high voltage cables by having the polls interrupt the line of

[4]Hamamatsu F4655-11 MCP

sight between cables and Rydberg atoms. Furthermore, this avoids having to construct polls that isolate the holder plate from the sample holder and the electrodes itself will be electrically isolated from the holder plate, as shown in figure 6.4(b). The isolation of the electrodes is achieved by the use of Macor isolation bushes. The semicircular hole is used to vent the hole.

The small resulting size of the electrodes leads to some effort in the engineering process. On the one hand, the electrodes are expected to be kept horizontally aligned without rotating with respect to the longitudinal axis, that is given by its connector screws. Ideally, rotation would be prevented by using two screws, but this is inhibited by the size of the electrodes. Thus, the bolted connections are achieved via one M1.6 screw per electrode only. These screws simultaneously ensure the electrical connection between high voltage wires and the electrodes. Venting is achieved by one cross-hole to the screw hole from the top of the electrode (can be seen in figure 6.4(b)).

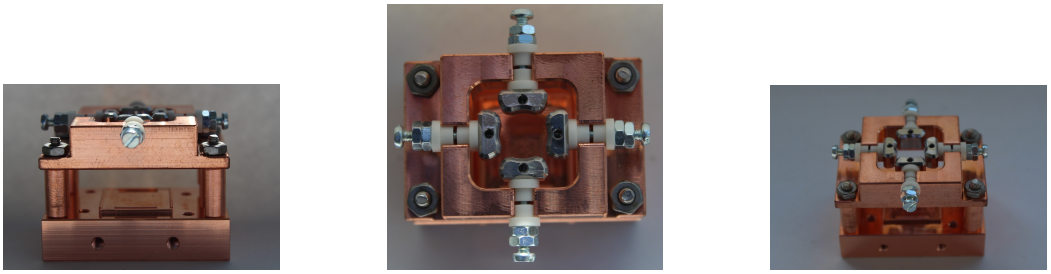

(a) **(b)** **(c)**

Figure 6.4: Photographs of the sample holder with mounted electrodes. In the side view picture of (a), the sample holder is easy to recognize, along with the platform for the atom chip, which is centred directly below the electrodes. The central electrode position above the chip centre can be seen in (b). It also allows all four electrodes and demonstrates their electrically isolated connection to the electrode holder and the venting holes for the electrode connections in the electrodes top sides. An impression of the complete construction can be gained from (c).

6.3.2 Electric field and ion trajectory simulations

The above section section 6.3.1 explained the mechanical part of the ionization and acceleration process and concludes with how such electrodes could be incorporated into the setup. With that being clear, the electrical part has to be discussed. In the following, the electric field in the region of the trapped atoms is analysed in order to determine which Rydberg states can be ionized with feasible applied voltages to the electrodes. Furthermore, the voltages needed to accelerate the ionized Rydberg atoms out of the experimental region and guide them onto the MCP are simulated.

Rydberg ionization

In order to be accelerated towards the MCP, the Rydberg atoms have to be ionized. The electric field that is needed to ionize a Rydberg state with principal quantum number n and quantum defect δ_{nlj} is given by [84]

$$E_{\text{ion}} = 3.2 \cdot 10^8 \frac{\text{V}}{\text{cm}} \cdot \frac{1}{(n - \delta_{nlj})^4} \tag{6.1}$$

for Rydberg s-states ($l = 0$).

With all voltages of the ionization and acceleration setup applied (see section 6.3.2) the electric field at the position of the atoms looks like shown in figure 6.5 for a voltage of $-100\,\text{V}$ applied to the acceleration electrodes presented in section 6.3.1. The plot shows the electric field in a plane 400 µm above and parallel to the chip surface, corresponding to the final trap position discussed above. In the centre region of that plane, which is where the atoms will be placed, the electric field reaches values of about $E_{\text{ion}} = 28\,\text{V/cm}$. With equation (6.1) and a quantum defect of $\delta_0 = 3.13$ for $nS_{1/2}$ states [64], equation (6.1) yields a lower bound principal quantum number

$$n_{\text{lower}} = 62, \tag{6.2}$$

that can be ionized in this setup. Since the minimum planned Rydberg state is $n = 68$, the simulated voltages are sufficient to ionize the target Rydberg states. Note, that there is no distinctive ionization step, but the electrodes designed in section 6.3.1 serve as ionization and acceleration electrodes simultaneously and the voltages considered here are voltages that also result in successful ion trajectory guidance. The latter will be subject of the next section.

Ion trajectory simulations

Charged particles with a charge q feel an electrical force $\vec{F}_{\text{el}} = q\vec{E}$ in an electric field $\vec{E}$, which leads to an acceleration of the particles. Ionized Rydberg atoms carry a charge of one time the elementary charge $+e$ and are therefore accelerated towards a negative potential and away from a positive potential.

The electrodes designed in section 6.3.1 are the first part of three major components of the acceleration setup, shown in figure 6.6. To reach the MCP, the ions must be accelerated towards the deflection electrode, which is at a positive potential. This deflects the electrodes towards the MCP, which is set to a negative voltage, and therefore attracts the ions. The last two steps are straightforward and will need some fine-tuning to find a working deflection voltage.

For the given setup, though, the first step is not so straightforward. As shown in figure 6.4 and figure 6.6, the first acceleration electrodes are located between the sample holder, i.e. the position of the ions, and the deflection electrodes. This leaves two options

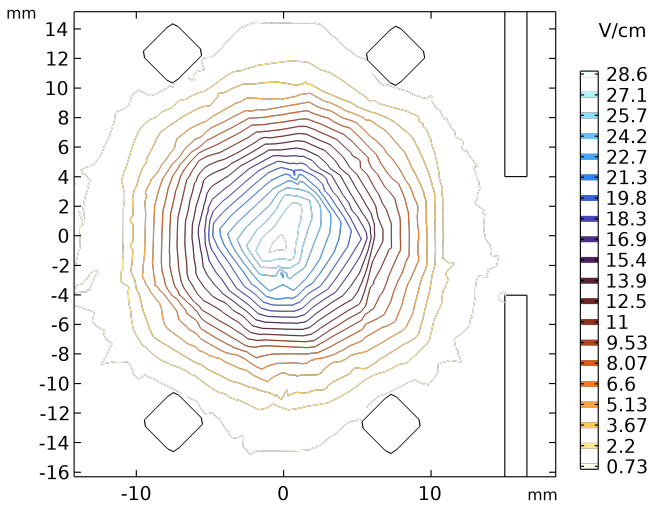

Figure 6.5: Contour plot of the electric field in a plane 400 µm above the chip surface, which is the height of the final atom positions. The shown created field is the result of all involved electrodes having their distinctive voltages applied (see text). The four black rectangles around the centre are the positions where the feet of the electrode mount sit and the two slim rectangles on the right are a cut through the inner cryo shield.

for accelerating them towards the deflection electrode, namely putting the sample holder at a positive potential and the electrodes on ground or putting the electrodes on a negative potential and the sample holder on ground.

The first option would be straightforward in a sense, because there would be in principle no need for any type of operation sequence, but static applied voltages would lead to an electric field that pushes the ions towards the deflection electrodes. This is a configuration also known as push-electrodes. However, this configuration is not suitable for the given setup because putting the sample holder to a positive potential would lead to large electric fields at the edges of the atom chip, which itself is at ground potential.

Accordingly, this leaves the second option, putting the electrodes to a negative potential and the complete sample holder to ground. That option does not come with any problems regarding the electric field at the chip, but it requires the acceleration electrodes to be switched during the acceleration phase of the ions. This can be made clear by imagining the potentials seen by the ions. For the static situation of a negative voltage applied to the acceleration electrodes, and a positive voltage to the deflection electrode, the electric field surrounding the ions is a superposition of the field created by both parts. The resulting potential landscape has a minimum at the position of the acceleration electrodes and rises again towards the deflection electrodes. Since the electric force for this static configuration is conservative, it is not possible for the ions to escape the

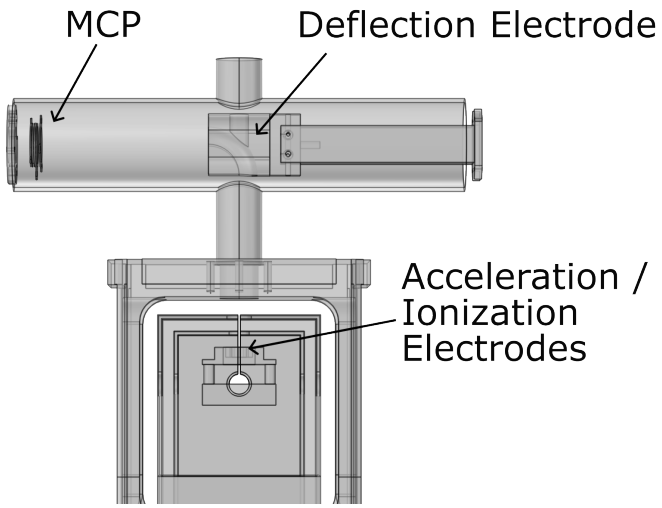

Figure 6.6: CAD drawing of the Science Chamber as used in the Comsol simulations. The MCP, deflection and acceleration electrodes are shown. The acceleration electrodes are simultaneously used for ionization, see text.

potential minimum and reach the deflection electrode, which is why they oscillate between two positions in front of and behind the acceleration electrodes. This behaviour is shown in figure 6.7(a). Instead, the acceleration electrodes have to be switched off during the acceleration phase, ideally at exactly the moment when they pass the potential minimum created by the acceleration electrodes. At that position, they reach their maximum kinetic energy which subsequently has to suffice in order to overcome the potential barrier towards the deflection electrode.

In the following, the needed voltages and the sensitivity to acceleration time is discussed by using a Comsol simulation [72]. The simulation computes ion trajectories with the Electrostatics and Charged Particle Tracing modules.

In principle, these simulations require only one initial electric field calculation for the complete setup and all set voltages, which is subsequently used for the trajectory simulations. However, since the voltage switch leads to a time-dependent electric field, which in term leads to calculating the electric field before each next particle trajectory step, the simulation time would increase significantly. For that reason, the simulation was simplified under the assumption of an infinitely fast switching time of the acceleration electrodes. This assumption allows to separate the simulation into two parts, namely the initial ion acceleration with the acceleration electrodes switched on, and a second part

with the acceleration electrodes on ground and the ions starting at the positions and corresponding velocities of the final step of the first simulation. With that, the electric field has to be calculated only twice and leads to fast runtimes again.

Finally, the simulation is run for an acceleration electrode voltage of $V_a = -100\,\mathrm{V}$ and a deflection electrode voltage of $V_{def} = 25\,\mathrm{V}$. The voltage of the MCP is set to $V_{MCP} = -2.5\,\mathrm{kV}$. With these parameters, the first simulation is run for 3 µs in time steps of 1 ns. Initially, there are 121 atoms evenly distributed over an area of 1x1 mm^2 around the chip centre, which sits directly below the acceleration electrodes.

If the acceleration electrodes are set to ground potential after an initial acceleration time of $t_a = 1.800\,\mu\mathrm{s}$, 120 out of 121 initial particles reach the MCP. Therefore, this is found to be an ideal acceleration time. The corresponding trajectories are shown in figure 6.7(b).

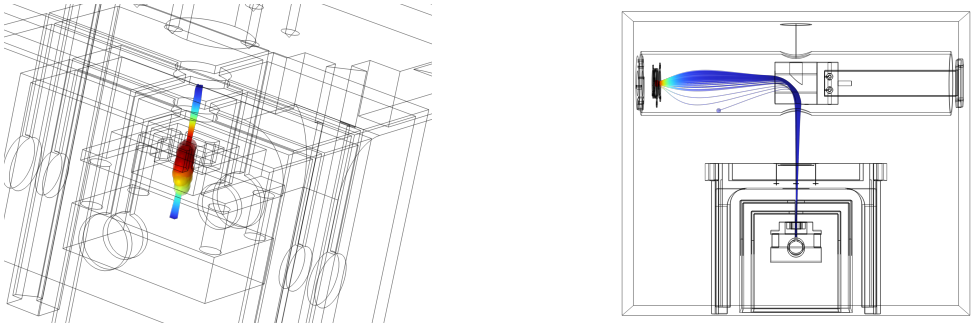

(a) **(b)**

Figure 6.7: Ion trajectories for an acceleration scheme (a) without and (b) with switching of the pull electrodes. If the electrodes are not switched off after an initial acceleration phase of the ions, they oscillate around the potential minimum created by the acceleration electrodes, shown in (a). However, it is possible to find an acceleration time (after 1.800 µs for the parameters simulated here, see text) after which most trajectories end on the MCP, shown in (b).

After having found a working configuration, the sensitivity to the switch off time is tested. For a symmetric interval of 50 ns around $t_a = 1.800\,\mu\mathrm{s}$ trajectories that end on the MCP are obtained, the corresponding trajectories are shown in figure 6.8. For the upper edge case of that interval at $t_a = 1.825\,\mu\mathrm{s}$ 20 out of 121 simulated trajectories end on the MCP and for the lower edge case of the interval for $t_a = 1.775\,\mu\mathrm{s}$ 92 out of 121 simulated trajectories end on the MCP. This result shows that the switch off time is more sensitive to later than to earlier switch off times. Next to an asymmetric potential, this could possibly be enhanced by the geometrical design of the deflection electrode.

For even longer and shorter acceleration times, trajectories are shown in figure 6.9. If the acceleration time is too short, the ions turn around before reaching the deflection electrode, shown in figure 6.9(a). If it is too long, the deflection voltage does not suffice

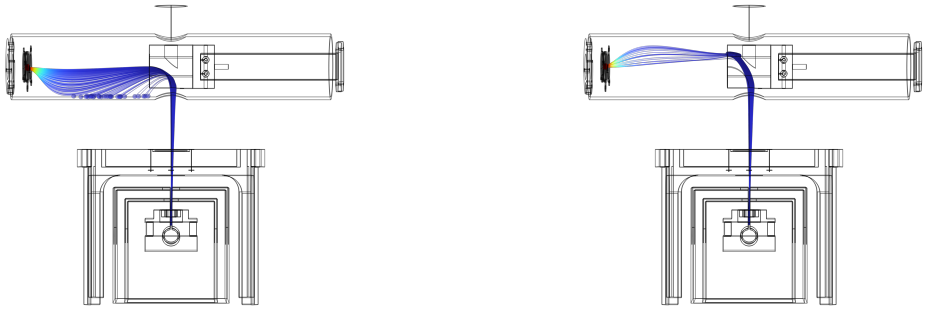

(a) $t_a = 1.775\,\mu s$ **(b)** $t_a = 1.825\,\mu s$

Figure 6.8: Ion trajectories for edge cases of a symmetric interval around the found ideal acceleration time of $t_a = 1.800\,\mu s$ for the given setup. The number of atoms reaching the MCP is more sensitive to switching off the electrodes (a) 25 ns previous to the optimal acceleration time than (b) 25 ns after it. This could be enhanced by the geometry of the deflection electrode.

to deflect the ions towards the MCP, shown in figure 6.9(b).

As a conclusion, the simulations show that it is possible to obtain ion trajectories that end at the MCP for experimentally feasible (order of several 10 ns) acceleration and electrode switching times. Further conclusions could be drawn from the simulation by investigating the velocity behaviour of the atoms when passing the acceleration setup.

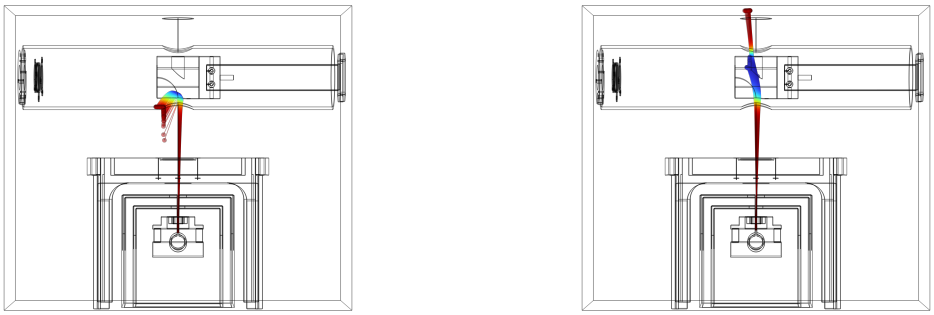

(a) $t_a = 1.7\,\mu s$ **(b)** $t_a = 1.9\,\mu s$

Figure 6.9: Ion trajectories after (a) too short and (b) too long initial acceleration times. For too short acceleration intervals, the ion trajectories turn before reaching the deflection electrodes and for too long initial accelerations the simulated deflection voltage does not suffice to deflect the ions.

Chapter 7

Conclusion and outlook

This thesis dealt with the design of a first-generation atom chip for interfacing trapped Rydberg atoms and a microwave resonator in form of a coplanar waveguide resonator for the HQO experiment. Furthermore, the fabrication of the atom chip and the integration into the existing experimental setup, including the necessary hardware like a sample holder, was planned.

The atom chip was designed under the premise of facilitating the hand-over of trapped cold atoms in a quadrupole trap as part of a magnetic transport setup into an on-chip magnetic trap, that is generated by a magnetic Z wire trap on the chip surface. It was demonstrated by simulation that such an atom transfer can be expected to provide sufficient efficiency ranging from $40\,\% - 100\,\%$, depending mainly on the initial cloud temperature. The simulations were run for all involved trap parameters for initial atom cloud temperatures and linear ramping sequences that are expected to be experimentally feasible.

The experimental procedure after the atom cloud transfer will include the exact relative positioning of atom cloud and coplanar waveguide, subsequent Rydberg excitation and Rydberg ionization as a final step after interaction with the resonator. It was shown that the positioning can be controlled with high precision by the Z wire trap parameters. This in turn allows precise control of the interaction strength. To achieve interaction between the Rydberg atoms and the coplanar waveguide resonator in the first place, the resonator was designed to match the transition frequency f_{85} of the $85S_{1/2} \rightarrow 85P_{3/2}$ electric dipole transition of ^{87}Rb atoms with its second harmonic resonator mode. This Rydberg transition was chosen for two reasons. First, the transition frequency of 5.8 GHz is in the regime that superconducting qubits work at [10] and secondly, there exists a lower lying Rydberg transition between $68S_{1/2} \rightarrow 68P_{3/2}$ with almost exactly twice the frequency difference. That allows for the flexibility to use the fourth harmonic of the resonator to address it.

The interaction strength was estimated based on these Rydberg transitions and the published quality factor of a comparably coupled superconducting coplanar waveguide resonator in reference [57]. It was shown that the designed coplanar waveguide resonator is expected to enable coupling strengths that are around 1 MHz even for input powers as low as $1 \cdot 10^{-6}$ mW.

Next to these estimations, the fabrication of the physical device was prepared. First,

the complete chip layout was designed under the premise of placing the on-chip structures in a way that enables coupling, which has lead to the coupling strength calculations mentioned above. Additionally, this includes integrating structures for an electrical connection of the chip, which was considered by the placement of bond pads. The bond pads will be contacted to printed circuit boards (PCBs) which provide the electric supply. The PCB design and its integration was discussed.

The chip is currently being fabricated by means of lithography processes as part of a collaboration with the Forschungszentrum Jülich. The lithography masks required for the distinctive lithography steps and the material choices for the chip fabrication were discussed.

To integrate the fabricated chip into the experimental setup a sample holder made of high-thermal conductivity copper was designed, which will be attached to the cryostat inherent sample holder. The attachment of the chip to the sample holder is planned to be of permanent nature. So, some insight was given into the first tests of attachment realizations, that are required to withstand the demanding experimental conditions in a cryogenic environment.

For conducting electric field Rydberg ionization and detection, a construction for sample-holder mounted electrodes was designed and built. Furthermore, it was simulated that the electrode setup allows ionizing Rydberg states down to sufficiently low principal quantum numbers. It was shown by simulations that the planned pull-electrode setup allows the guidance of appropriate ion trajectories for detection with experimentally feasible voltages and electrode switching times.

The next necessary step towards the experimental realization of the results presented in this thesis is to continue with the chip attachment steps. Care has to be taken with the thermal conductivity of the attachment method to avoid insufficient cooling of the chip which could not only lead to shifts in the resonator's frequency as demonstrated, but also to a complete breakdown of superconductivity during the experimental cycle.

With the chip being attached, and the PCBs mounted to the sample holder, the next step will be the realization of wire bonding for electrical contacting of the chip. As soon as this step is completed, the resonator can be characterized with regard to the achieved resonance frequency and linewidth with a vector network analyzer.

When it comes to the complete experimental setup, it will be required to integrate the sample holder along with the electrically connected chip and mounted electrodes into the experimental setup and test the transfer sequence for chip loading. Further simulations will be needed to investigate the possibilities of stray electric field compensation with the given setup. Finally, field ionization and acceleration protocols will have to be tested experimentally.

To get closer towards the declared goal of interfacing electromechanical oscillators and Rydberg atoms on an atom chip, the initiated electromechanical resonator simulations will have to be continued. Eventually, this will have to be used to plan and build an atom chip with an integrated high-overtone bulk acoustic resonator.

Appendix A

Appendix

A.1 Length deviation induced resonance frequency shift of coplanar waveguide resonators

The length of the coplanar waveguide resonator determines its resonance frequency. This section provides the derivation for estimations of expectable length-deviation induced resonance frequency shifts.

Use the resonance frequency function (equation (3.4))

$$f = \frac{nc}{2\sqrt{\epsilon_{\text{eff}}}} \frac{1}{l}$$

to make a Taylor approximation around $l = l_0$ to the first order, where l_0 is the length for the target resonance frequency. Cancelling the approximation after first order is justified under the assumption of the length deviation $\Delta l := l - l_0 \ll l_0$.

This yields, with the abbreviation $q = \frac{nc}{2\sqrt{\epsilon_{\text{eff}}}}$, which is assumed to not change with resonator length (ϵ_{eff} does not depend on l),

$$\begin{aligned} f(l; l_0) &\approx f(l_0) + \frac{\partial f}{\partial l}\bigg|_{l=l_0} (l - l_0) + \mathcal{O}\left((l - l_0)^2\right) \\ &= f_0 - q\frac{1}{l^2}\bigg|_{l=l_0} (l - l_0) + \mathcal{O}\left((l - l_0)^2\right) \\ &= f_0 - q\frac{\Delta l}{l_0^2} + \mathcal{O}\left(\Delta l^2\right). \end{aligned}$$

Subtracting the target resonance frequency f_0, defining $\Delta f := f(l; l_0) - f_0$ and plugging the definition for q back in results in

$$\Delta f(\Delta l) = -\frac{nc}{2l_0^2\sqrt{\epsilon_{\text{eff}}}} \Delta l. \tag{A.1}$$

Thus, equation (A.1) shows that to first order the resonance frequency changes linearly with a possible length deviation. Neglecting the second order under the given assumption is justified for possible fabrication induced length deviations in the range of µm, compared to the resonator length in the range of mm.

Bibliography

[1] J. P. Dowling and G. J. Milburn, *Quantum Technology: The Second Quantum Revolution*, Philosophical Transactions of the Royal Society of London. Series A: Mathematical, Physical and Engineering Sciences **361** (15, 2003), ed. by A. G. J. MacFarlane, 1655–1674.

[2] G. Kurizki et al., *Quantum Technologies with Hybrid Systems*, Proc. Natl. Acad. Sci. U.S.A. **112** (31, 2015), 3866–3873.

[3] S. Pirandola et al., *Advances in Quantum Cryptography*, Adv. Opt. Photon. **12** (31, 2020), 1012.

[4] N. Aslam et al., *Quantum Sensors for Biomedical Applications*, Nat Rev Phys **5** (3, 2023), 157–169.

[5] I. M. Georgescu, S. Ashhab and F. Nori, *Quantum Simulation*, Rev. Mod. Phys. **86** (10, 2014), 153–185.

[6] E. Chae, J. Choi and J. Kim, *An Elementary Review on Basic Principles and Developments of Qubits for Quantum Computing*, Nano Convergence **11** (18, 2024), 11.

[7] M. Wallquist et al., *Hybrid Quantum Devices and Quantum Engineering*, Phys. Scr. **T137** (2009), 014001.

[8] Z.-L. Xiang et al., *Hybrid Quantum Circuits: Superconducting Circuits Interacting with Other Quantum Systems*, Rev. Mod. Phys. **85** (9, 2013), 623–653.

[9] A. A. Clerk et al., *Hybrid Quantum Systems with Circuit Quantum Electrodynamics*, Nat. Phys. **16** (2020), 257–267.

[10] F. Arute et al., *Quantum Supremacy Using a Programmable Superconducting Processor*, Nature **574** (24, 2019), 505–510.

[11] Y. Kim et al., *Evidence for the Utility of Quantum Computing before Fault Tolerance*, Nature **618** (15, 2023), 500–505.

[12] E. R. MacQuarrie et al., *The Emerging Commercial Landscape of Quantum Computing*, Nat Rev Phys **2** (12, 2020), 596–598.

[13] P. W. Shor, *Polynomial-Time Algorithms for Prime Factorization and Discrete Logarithms on a Quantum Computer*, SIAM J. Comput. **26** (1997), 1484–1509.

[14] C. Monroe et al., *Large-Scale Modular Quantum-Computer Architecture with Atomic Memory and Photonic Interconnects*, Phys. Rev. A **89** (13, 2014), 022317.

[15] C. D. Bruzewicz et al., *Trapped-Ion Quantum Computing: Progress and Challenges*, Applied Physics Reviews **6** (1, 2019), 021314.

[16] C. S. Adams, J. D. Pritchard and J. P. Shaffer, *Rydberg Atom Quantum Technologies*, J. Phys. B: At. Mol. Opt. Phys. **53** (1, 2020), 012002.

[17] M. Kjaergaard et al., *Superconducting Qubits: Current State of Play*, Annu. Rev. Condens. Matter Phys. **11** (10, 2020), 369–395.

[18] D. P. DiVincenzo and IBM, *The Physical Implementation of Quantum Computation*, Fortschr. Phys. **48** (2000), 771–783.

[19] F. Pan, K. Chen and P. Zhang, *Solving the Sampling Problem of the Sycamore Quantum Circuits*, Phys. Rev. Lett. **129** (22, 2022), 090502.

[20] M. Gao, Y.-x. Liu and X.-B. Wang, *Coupling Rydberg Atoms to Superconducting Qubits via Nanomechanical Resonator*, Phys. Rev. A **83** (11, 2011), 022309.

[21] J. Clarke and F. K. Wilhelm, *Superconducting Quantum Bits*, Nature **453** (2008), 1031–1042.

[22] D. Petrosyan et al., *Microwave to Optical Conversion with Atoms on a Superconducting Chip*, New J. Phys. **21** (1, 2019), 073033.

[23] N. J. Lambert et al., *Coherent Conversion Between Microwave and Optical Photons—An Overview of Physical Implementations*, Adv Quantum Tech **3** (2020), 1900077.

[24] M. Mirhosseini et al., *Superconducting Qubit to Optical Photon Transduction*, Nature **588** (24, 2020), 599–603.

[25] M. J. Weaver et al., *An Integrated Microwave-to-Optics Interface for Scalable Quantum Computing*, Nat. Nanotechnol. **19** (2024), 166–172.

[26] P. Kharel et al., *Ultra-High- Q Phononic Resonators on-Chip at Cryogenic Temperatures*, APL Photonics **3** (2018), 066101.

[27] A. N. Cleland and M. R. Geller, *Superconducting Qubit Storage and Entanglement with Nanomechanical Resonators*, Phys. Rev. Lett. **93** (10, 2004), 070501.

[28] Y. Chu et al., *Quantum Acoustics with Superconducting Qubits*, Science **358** (13, 2017), 199–202.

[29] N. Lauk et al., *Perspectives on Quantum Transduction*, Quantum Sci. Technol. **5** (1, 2020), 020501.

[30] R. Stevenson et al., *Prospects of Charged-Oscillator Quantum-State Generation with Rydberg Atoms*, Phys. Rev. A **94** (12, 2016), 043813.

[31] A. D. O'Connell et al., *Quantum Ground State and Single-Phonon Control of a Mechanical Resonator*, Nature **464** (2010), 697–703.

[32] T. F. Gallagher, *Rydberg Atoms*, Cambridge University Press, 1994.

[33] J. A. Sedlacek et al., *Microwave Electrometry with Rydberg Atoms in a Vapour Cell Using Bright Atomic Resonances*, Nature Phys **8** (2012), 819–824.

[34] D. Davtyan et al., *Controlling Stray Electric Fields on an Atom Chip for Experiments on Rydberg Atoms*, Phys. Rev. A **97** (22, 2018), 023418.

[35] C. Hermann-Avigliano et al., *Long Coherence Times for Rydberg Qubits on a Superconducting Atom Chip*, Phys. Rev. A **90** (23, 2014), 040502.

[36] J. Schmiedmayer and R. Folman, *Miniaturizing Atom Optics: From Wires to Atom Chips*, Comptes Rendus de l'Académie des Sciences - Series IV - Physics **2** (2001), 551–563.

[37] A. Haase et al., *Trapping Neutral Atoms with a Wire*, Phys. Rev. A **64** (13, 2001), 043405.

[38] J. Popp, *Construction and Preparation of an Experimental Setup for Excitation and Detection of Rydberg Atoms in a Cryogenic Environment*, MA thesis, Universität Bonn, 2024.

[39] R. Barends, *Photon-Detecting Superconducting Resonators*, PhD thesis, TU Delft, 2009.

[40] M. Kaiser et al., *Cavity-Driven Rabi Oscillations between Rydberg States of Atoms Trapped on a Superconducting Atom Chip*, Phys. Rev. Research **4** (18, 2022), 013207.

[41] R. Grimm, M. Weidemüller and Y. B. Ovchinnikov, *Optical Dipole Traps for Neutral Atoms*, *Advances In Atomic, Molecular, and Optical Physics*, **42**, Elsevier, 2000, 95–170.

[42] J. Fortágh and C. Zimmermann, *Magnetic Microtraps for Ultracold Atoms*, Rev. Mod. Phys. **79** (1, 2007), 235–289.

[43] D. Meschede, ed., *Gerthsen Physik*, 24th ed., 2010.

[44] W. Ketterle, D. S. Durfee and D. M. Stamper-Kurn, *Making, Probing and Understanding Bose-Einstein Condensates*, Apr. 5, 1999, arXiv: cond-mat/9904034, URL: http://arxiv.org/abs/cond-mat/9904034 (visited on 05/17/2024), prepublished.

[45] D. A. Steck, *Rubidium 87 D Line Data*, Los Alamos National Laboratory, 2003.

[46] J. G. E. Harris et al., *Deep Superconducting Magnetic Traps for Neutral Atoms and Molecules*, Review of Scientific Instruments **75** (1, 2004), 17–23.

[47] S. Schneider, *Bose-Einstein Kondensation in Einer Magnetischen Z-Falle*, PhD thesis, Universität Heidelberg, 2003.

[48] D. E. Pritchard, *Cooling Neutral Atoms in a Magnetic Trap for Precision Spectroscopy*, Phys. Rev. Lett. **51** (10, 1983), 1336–1339.

[49] M. S. Yoon, *Experiments on Magnetic Transport, Magnetic Trapping, and Bose-Einstein Condensation*, PhD thesis, University of Oxford, 2009.

[50] E. Haller, *Mikrofallen Nahe Der Oberflaeche von Atomchips*, diploma, Heidelberg, 2004.

[51] Michael-Ortner et al., *magpylib*, version 5.0.3, June 25, 2023, URL: https://magpylib.readthedocs.io/en/latest/ (visited on 07/20/2024).

[52] R. Huebener et al., *Critical Current Density in Superconducting Niobium Films*, IEEE Trans. Magn. **11** (1975), 344–346.

[53] W. R. Hudson and R. J. Jirberg, *Superconducting Properties of Niobium Films*, Lewis Research Center, National Aeronautics and Space Administration, 1971.

[54] M. Tinkham, *Introduction to Superconducitvity*, 2nd ed., International Series in Pure and Applied Physics, McGraw-Hill, Inc., 1996.

[55] D. M. Pozar, *Microwave Engineering*, 4, John Wiley & Sons, Inc., 2012.

[56] B. C. Wadell, *Transmission Line Design Handbook*, Artech House, Inc., 1991.

[57] M. Göppl et al., *Coplanar Waveguide Resonators for Circuit Quantum Electrodynamics*, J. Appl. Phys. **104** (2008).

[58] D. Bothner et al., *Inductively Coupled Superconducting Half Wavelength Resonators as Persistent Current Traps for Ultracold Atoms*, New J. Phys. **15** (13, 2013), 093024.

[59] A. Blais et al., *Circuit Quantum Electrodynamics*, Rev. Mod. Phys. **93** (19, 2021), 025005.

[60] H. Hattermann et al., *Coupling Ultracold Atoms to a Superconducting Coplanar Waveguide Resonator*, Nat Commun **8** (21, 2017), 2254.

[61] M. S. O'Sullivan and B. P. Stoicheff, *Scalar Polarizabilities and Avoided Crossings of High Rydberg States in Rb*, Phys. Rev. A **31** (1, 1985), 2718–2720.

[62] MTI Corporation, *C plane sapphire wafer*, URL: https://www.mtixtl.com/AL-C-101001-S1.aspx#:~:text=Thermal%20Conductivity%3A%2046.06%20%40%200%20o,x10%2D5%20at%20C%20axis (visited on 07/20/2024).

[63] T. Boutell and D. McMahil, *Coplanar Waveguide Analysis/Synthesis Calculator*, July 20, 2024, URL: https://wcalc.sourceforge.net/cgi-bin/coplanar.cgi (visited on 07/10/2024).

[64] M. Mack et al., *Measurement of Absolute Transition Frequencies of Rb 87 to nS and nD Rydberg States by Means of Electromagnetically Induced Transparency*, Phys. Rev. A **83** (23, 2011), 052515.

[65] Y. Wang, *Fundamental Elements of Applied Superconductivity in Electrical Engineering*, John Wiley & Sons Singapore Pte. Ltd., 2013.

[66] J. Bardeen, L. N. Cooper and J. R. Schrieffer, *Theory of Superconductivity*, Phys. Rev. **108** (1, 1957), 1175–1204.

[67] R. Meservey and P. M. Tedrow, *Measurements of the Kinetic Inductance of Superconducting Linear Structures*, Journal of Applied Physics **40** (1, 1969), 2028–2034.

[68] A. Faltermeier, *Optimierung Supraleitender Schichten Aus Niob, Niobnitrid Und Niobtitannitrid Fur Den Einsatz in Mikrowellenresonatoren*, MA thesis, TU München, 2019.

[69] J. Rairden and C. Neugebauer, *Critical Temperature of Niobium and Tantalum Films*, Proc. IEEE **52** (1964), 1234–1238.

[70] J. R. Clem, *Inductances and Attenuation Constant for a Thin-Film Superconducting Coplanar Waveguide Resonator*, Journal of Applied Physics **113** (7, 2013), 013910.

[71] L. P. Chernenko et al., *Measurement of Magnetic Field Penetration Depth in Niobium Polycrystalline Films by the Polarized Neutron Reflection Method*, *Surface X-Ray and Neutron Scattering*, ed. by H. Zabel and I. K. Robinson, red. by H. K. V. Lotsch, **61**, Springer Berlin Heidelberg, 1992, 209–211.

[72] COMSOL AB, *COMSOL Multiphysics®*, version 6.1.

[73] H. Banderier, M. Drimmer and Y. Chu, *Unified Simulation Methods for Quantum Acoustic Devices*, Phys. Rev. Applied **20** (9, 2023), 024024.

[74] N. Šibalić et al., *ARC: An Open-Source Library for Calculating Properties of Alkali Rydberg Atoms*, Computer Physics Communications **220** (2017), 319–331.

[75] J. W. Ekin, *Experimental Techniques for Low-Temperature Measurements*, Oxford University Press, 2021.

[76] H. Zhang et al., *High-Tone Bulk Acoustic Resonators on Sapphire, Crystal Quartz, Fused Silica, and Silicon Substrates*, Journal of Applied Physics **99** (15, 2006), 124911.

[77] A. J. Annunziata et al., *Tunable Superconducting Nanoinductors*, Nanotechnology **21** (5, 2010), 445202.

[78] K.-y. Hashimoto, ed., *RF Bulk Acoustic Wave Filters For Communications*, Artech House, 2009.

[79] T. Baron et al., *High-Overtone Bulk Acoustic Resonator*, *Modeling and Measurement Methods for Acoustic Waves and for Acoustic Microdevices*, ed. by M. G. Beghi, InTech, 28, 2013.

[80] X. Xu, M. Newns and M. Oxborrow, *Simulating the Magnetic Fields Generated by Piezoelectric Devices Using FEM Software: Beyond the Quasistatic Approximation*, Journal of Applied Physics **132** (28, 2022), 205107.

[81] H. Hattermann, *Interfacing Cold Atoms and Superconductors*, PhD thesis, Universität Tübingen, 2013.

[82] F. Rondeaux, Ph. Bredy, J.M. Rey, *Thermal Conductivity Measurements of Epoxy Systems at Low Temperature*, 2001, Poster presented at Cryogenic Engineering Conference (CEC).

[83] G. Humpston and D. M. Jacobson, *Indium Solders*, Advanced Materials and Processes (2005).

[84] I. Beterov et al., *Ionization of Rb and Na Rydberg Atoms by Blackbody Radiation*, *2007 European Conference on Lasers and Electro-Optics and the International Quantum Electronics Conference*, 2007 European Conference on Lasers and Electro-Optics and the International Quantum Electronics Conference, IEEE, 2007, 1–1.

[85] N. Stiesdal et al., *Controlled Multi-Photon Subtraction with Cascaded Rydberg Superatoms as Single-Photon Absorbers*, Nat Commun **12** (15, 2021), 4328.

Acknowledgement

The past year of working on this master project has been a year full of interesting challenges, times of ease and fortunately rather rare times of stress. However, as it draws to a close, I can say that it has been most enriched by the people I have been surrounded by during this time. Therefore, I would like to take this opportunity to say thank you.

I would like to thank Professor Sebastian Hofferberth for giving me the opportunity to work on this project in his group and Professor Stefan Linden for taking on the second supervisor.

Additionally, I would like to thank the complete group for creating the most enjoyable work environment. You really are a bunch of great people and it has been a pleasure working, eating and drinking coffee with you. Of course, special thanks go to the team of the HQO experiment during this time, it would not have been the same or as much fun without you. Thank you to Cedric Wind for taking on the role as being my - and at the same time of two other master students - direct supervisor. That is a challenge that you have mastered exceptionally well in my opinion.

Although living my office life, most of the time far away from the sacred halls of the HQO lab, it has always been a very tempting opportunity to come over to you and have a chat - or coffee, or both. Also, thank you very much again to all of you that have helped me with proofreading this thesis!

With the writing of this thesis, not only the past year but rather the past years of studying come to an end. For me, this has been a time of larger changes including a change of the university. However, I am fortunate enough to say that quite a few people I have had the pleasure to get to know along the way have remained being a constant part of my life, which I am very grateful for. Thank you for that!

Almost last but certainly not least I would like to thank my girlfriend for the continuing support over the past few years. Thank you for your patience and understanding over all that time!

Finally, I would like to express my gratitude for having such a supportive family, I would for sure not be where I am today without you.